Polymer-Derived Ceramic Coatings for Corrosion Protection

Doctoral Thesis

by

Bura Rajesh

2017MSZ0001

DEPARTMENT OF METALLURGICAL AND MATERIALS ENGINEERING

INDIAN INSTITUTE OF TECHNOLOGY ROPAR

MAY 2025

Polymer-Derived Ceramic Coatings for Corrosion Protection

A Thesis Submitted

In Partial Fulfilment of the Requirements

for the Degree of

DOCTOR OF PHILOSOPHY

by

Bura Rajesh

2017MSZ0001

DEPARTMENT OF METALLURGICAL AND MATERIALS ENGINEERING

INDIAN INSTITUTE OF TECHNOLOGY ROPAR

MAY 2025

BURA RAJESH: Polymer-Derived Ceramic Coatings for Corrosion Protection

DEDICATED

TO

MY MOTHER AND FATHER

Declaration of Originality

I hereby declare that the work which is being presented in the thesis entitled **Polymer-Derived Ceramic Coatings for Corrosion Protection** has been solely authored by me. It presents the result of my own independent investigation/research conducted during the time period from August 2017 to September 2024 under the supervision of Dr. Ravi Mohan Prasad, IIT Ropar. To the best of my knowledge, it is an original work, both in terms of research content and narrative, and has not been submitted or accepted elsewhere, in part or in full, for the award of any degree, diploma, fellowship, associateship, or similar title of any university or institution. Further, due credit has been attributed to the relevant state-of-the-art and collaborations (if any) with appropriate citations and acknowledgements, in line with established ethical norms and practices. I also declare that any idea/data/fact/source stated in my thesis has not been fabricated/ falsified/ misrepresented. All the principles of academic honesty and integrity have been followed. I fully understand that if the thesis is found to be unoriginal, fabricated, or plagiarized, the Institute reserves the right to withdraw the thesis from its archive and revoke the associated Degree conferred. Additionally, the Institute also reserves the right to appraise all concerned sections of society of the matter for their information and necessary action (if any). If accepted, I hereby consent for my thesis to be available online in the Institute's Open Access repository, inter-library loan, and the title & abstract to be made available to outside organizations.

Signature

Name: BURA RAJESH
Entry Number: 2017MSZ0001
Program: Ph.D.
Department: Metallurgical and Materials Engineering
Indian Institute of Technology Ropar
Rupnagar, Punjab 140001

Date: 01-May-2025

Acknowledgements

I wish to thank my supervisor **Dr. Ravi Mohan Prasad** for his continuous support and encouragement throughout my journey as a PhD candidate. I am inspired by his knowledge and problem-solving skills. I wish to continue on his path to share my knowledge with others.

Dr. Pratik K. Ray, Chairman of my Doctoral Committee and Head of the Department of Metallurgical and Materials Engineering at IIT Ropar, has been very helpful and supportive during my time in research work. I would also like to thank my Doctoral Committee members, Prof. Harpreet Singh, Dr. Dhiraj K. Mahajan, and Dr. Tharamani C. N. from the Departments of Mechanical Engineering and Chemistry, respectively, for their unflagging attention to detail and constructive criticism during the course of the project.

Thanks to my respectful senior Dr. Binod Kumar for sharing his knowledge, and gratitude to my colleague Mr. Vishnu Girish for his continuous help, support and technical discussion. I am also grateful to my lab mates Mr. Ranjith Kumar and Mr. Jaganathan. Heartfelt thanks are also due to my friends Pankaj, Pranav, Jaswanth and Naresh for always being there for me.

My deepest gratitude goes to my family for their constant love and support throughout my life. Thanks to my father Mr. Bura Yedukondalu and my mother Mrs. Naga Laxmi (Late) for their immeasurable sacrifices and blessings. A very special thanks to my dear wife, Mrs. Bura Vinitha, for her endless affection and encouragement. All of them have always softened the life difficulties for me and I owe all my achievements, including this, to them. It is due to all these individuals who had put forth the effort and made this uphill task possible for me.

Lay Summary

Metals and alloys get damaged over a time period due to a natural process called corrosion. This occurs when a material reacts with its surrounding environment, such as water and air, causing it to weaken and damage the structure; corroded structures can compromise public safety. Stainless steel 304 (SS304) is mostly used in extreme/aggressive places like underwater pipelines, water treatment plants and storage containers for nuclear waste. SS304 contains a thin passive layer on the surface, which helps to prevent rusting. However, in seawater environments (chlorine-containing environments), this passive layer breaks down, and the underlying steel starts to corrode. Therefore, to enhance the corrosion resistance of metals in such environments, methods such as adding alloying elements to the base material and applying simple paint-like coatings are utilized.

In conventional routes, ceramic coatings are produced using Thermal Spray, Chemical Vapour Deposition, and Physical Vapour Deposition processes. However, these coatings have drawbacks; they consume more energy to coat ceramic and have higher equipment costs. Due to these drawbacks, Polymer-Derived Ceramic (PDCs) coatings have been studied to improve the corrosion resistance of SS304 in this work, due to lower synthesis temperatures and stability of PDCs under harsh chemical environments as well as high temperatures.

To coat the samples, a simple dip-coating method is used. After dipping SS304 in polymeric solution, the dipped samples are heat-treated to 800 °C under inert atmosphere to obtain silicon oxycarbide (SiOC) and silicon carbonitride (SiCN) ceramic coatings. Later, coated samples are studied using different structural characterization techniques and electrochemical testing. After two-fold coating, thickness of SiOC layer on SS304 is found to be ~1 μm, and after three-fold coating, thickness of SiCN layer is ~3 μm. Electrochemical testing was conducted on both coated and uncoated samples in a 0.6 M NaCl solution to determine the corrosion protection efficiency of the coatings. The results indicate that SiOC and SiCN coatings on SS304 significantly improved corrosion resistance. The corrosion mechanisms of both the uncoated and coated samples were analyzed using potentiodynamic polarization and electrochemical impedance spectroscopy (EIS). Among the two coatings, SiCN-coated SS304 exhibited superior corrosion resistance compared to SiOC-coated SS304 in 0.6 M NaCl solution.

Certificate

This is to certify that the thesis entitled **Polymer-Derived Ceramic Coatings for Corrosion Protection**, submitted by **BURA RAJESH (2017MSZ0001)** for the award of the degree of **Doctor of Philosophy** of the Indian Institute of Technology Ropar, is a record of bona fide research work carried out under my (our) guidance and supervision. To the best of my knowledge and belief, the work presented in this thesis is original and has not been submitted, either in part or in full, for the award of any other degree, diploma, fellowship, associateship or similar title of any university or institution.

In my (our) opinion, the thesis has reached the standard fulfilling the requirements of the regulations relating to the Degree.

Signature of the Supervisor

Dr. Ravi Mohan Prasad
Department of Metallurgical and Materials Engineering
Indian Institute of Technology Ropar
Rupnagar, Punjab 140001
Date: 01-May-2025

Abstract

Corrosion is common in industrial sectors where structures and machinery are made of metals and alloys. SS304 is a widely used stainless steel grade in the world and is generally used in applications that require strength and good corrosion resistance such as, in subsea pipelines, desalination plants, and in steel canisters, etc. SS304 mainly suffers from localized corrosion (pitting and crevice corrosion) in chloride-containing environments. The corrosion resistance of SS304 is facilitated by the presence of a thin passive film of chromium oxide on its surface. It is a well-known fact that pitting occurs when localized breakdown of the passive film occurs and it further leads to failure of components. All these causes massive economic loss in the form of replacing the structure or repairing the damaged section which leads to a decrease in production efficiency or plant shutdown for a few days.

The main objective of this thesis is enhancement of corrosion resistance of SS304 by depositing ceramic layers using polymer-derived route. Polymer-derived ceramics (PDCs) have gained good attention in the last two decades as they possess high thermochemical stability. In the present work, two types of ceramics (SiOC and SiCN) from polymer pyrolysis route were synthesized and coated on SS304. Corrosion protection performances of coated substrates were evaluated in 0.6 M NaCl solution.

Firstly, ceramic coating parameters were optimized for the deposition of SiOC and SiCN ceramic layers on SS304 using different precursor concentrations and by optimizing multi-fold coated layers followed by examining surface morphology. Subsequently, an amorphous SiOC layer with a thickness of about ~1 μm was deposited after two-fold coatings on SS304 by dip-coating with polysiloxane solution followed by pyrolysis at 800 °C under argon environment. Corrosion resistance of SiOC-coated SS304 was performed using open circuit potential (OCP), potentiodynamic polarization, and electrochemical impedance spectroscopy (EIS) methods. Electrochemical results confirmed improved corrosion protection behavior of SiOC-coated SS304 over uncoated SS304.

Afterwards, SiCN was synthesized by pyrolysis of a commercial polysilazane at 800 °C and a crack-free SiCN layer of ~3.2 μm on SS304 was coated using a multi-step dip-coating/pyrolysis process. Electrochemical characterization revealed that SiCN-coated SS304 had a significantly lower corrosion current density (and thus a lower corrosion rate) compared

to that of uncoated SS304 samples. Enhanced corrosion protection behavior of SiCN-coated SS304 was also confirmed by EIS measurements.

These findings signify the potential of SiOC and SiCN ceramic coatings for the protection of stainless steel in a seawater environment.

Keywords: Polymer-derived ceramics, Coating, Corrosion, Potentiodynamic polarization, Electrochemical impedance spectroscopy (EIS).

List of Publications

Journals

1. **R. Bura**, B. Kumar, R.M. Prasad, "Polymer-Derived SiOC Ceramic Coating for Corrosion Protection", *International Journal of Applied Ceramic Technology*, 21 (2024) 900-909.
2. **R. Bura**, V. Girish C, R.M. Prasad, "Enhanced Corrosion Protection Performance using Polysilazane-Derived Amorphous SiCN Ceramic Coating", *Surface and Coating Technology,* 494 (2024) 131402.
3. B. Kumar, **R. Bura**, R.M. Prasad, Amorphous microporous SiOC-coated SnO_2 sensor for selective hydrogen sensing application (*communicated*).
4. V. Girish C, **R. Bura**, H. Singh, R.M Prasad, "Development and Analysis of In-Situ Synthesized Polymer Derived Amorphous SiCN Reinforced AMC" **(***communicated***).**

Conference Presentations

1. **Bura Rajesh,** Binod Kumar, Ravi Mohan Prasad, Polymer-Derived Ceramic Coatings for Corrosion Protection, 48th International Conference and Exposition on Advanced Ceramics and Composites (ICACC 2024), Florida, USA, Jan 2024.
2. **Bura Rajesh**, Ravi Mohan Prasad, Corrosion Protection Behavior of Polymer-Derived Ceramic Coatings, CII National Corrosion Management Practices-Competition & Awards 2023, 18-19 Dec 2023, CII, Chandigarh.
3. **Bura Rajesh**, Ravi Mohan Prasad, Polymer-Derived Ceramic Coatings for Corrosion Resistance, iConFirm 2023, IIT Ropar, India, Dec 2023.
4. **Bura Rajesh**, Ravi Mohan Prasad, Study of Corrosion and Oxidation Resistance of Polymer-Derived Ceramic Coatings, 4th Edition of International Conference on "Industrial Coating & Surface Treatment (ICST 2023)" New Delhi, March 2023.
5. **Bura Rajesh**, Ravi Mohan Prasad, Corrosion and High-Temperature Oxidation Resistance Behavior of Polymer-Derived SiOC Ceramic coatings, National Symposium on Electrochemical Science and Technology (NSEST-2021), The Electrochemical Society of India, IISc Bangalore, India, June 2022.
6. **Bura Rajesh**, Ravi Mohan Prasad, Corrosion and Oxidation Behavior of Polymer-Derived SiOC Ceramic coatings, 58th National Metallurgists Day and 74th Annual Technical Meeting (NMD-ATM 2020), IIT Bombay, India, Feb 2021.
7. **Bura Rajesh**, Binod Kumar, Ravi M. Prasad, Polymer-Derived Ceramic Coatings for Corrosion and Oxidation Resistance, The Indian Institute of Metals NMD-ATM 2019, Trivandrum, Kerala, India, Nov 2019.

Table of Contents

List of Figures

List of Tables

Notations and Abbreviations

AC	Alternating current
ATR-FTIR	Attenuated total reflectance-Fourier transform infrared
ASS	Austenitic stainless steel
°C	Degree Celsius
CE	Counter Electrode
CPE_c	Capacitance due to coating
$\mathbf{CPE_{dl}}$	Double-layer capacitance
CVD	Chemical vapor deposition
DSS	Duplex stainless steel
E	Potential
EIS	Electrochemical Impedance Spectroscopy
EIC	Environmentally induced cracking
EMF	Electromotive force
$\mathbf{E_{corr}}$	Corrosion potential
$\mathbf{E_{pit}}$	Pitting potential
$\mathbf{E_{pa}}$	Passive potential
FESEM	Field emission scanning electron microscopy
HIC	Hydrogen induced cracking
i	Current
$\mathbf{i_{corr}}$	Corrosion current density
$\mathbf{i_p}$	Passive current density
M	Metal
NMR	Nuclear magnetic resonance
OCP	Open circuit potential
PVD	Physical vapor deposition
PDCs	Polymer-derived ceramics
P.E.	Protection efficiency
RE	Reference electrode
$\mathbf{R_c}$	Resistance due to coating
$\mathbf{R_{ct}}$	Charge transfer resistance
$\mathbf{R_p}$	Polarization resistance
$\mathbf{R_{sol}}$	Solution resistance

SHE	Standard hydrogen electrode
SCC	Stress corrosion cracking
SS	Stainless steel
SS304	Stainless steel 304
SiOC	Silicon-oxycarbide
SiCN	Silicon-carbonitride
TGA	Thermal gravimetric analysis
W	Warburg impedance
WE	Working electrode
XRD	X-ray Diffraction
Z	Impedance
Z′	Real part of the impedance
Z″	Imaginary part of impedance

Introduction and motivation

Metallic materials deteriorates over a time due to corrosion caused by electrochemical and chemical interactions with the exposed surroundings. Stainless steel (SS304) is widely used in applications under extreme environments such as in subsea pipelines, desalination plants, and canisters for spent nuclear fuels (SNFs), etc. Thin passive film of chromium oxide on the steel surface imparts corrosion resistance, however, it suffers from corrosion in chloride-containing environments. Formation of pits in SS304 occurs at a potential above ~0.22 V vs. Ag/AgCl. This causes significant economic losses worldwide. Global cost of corrosion is estimated to be US $2.5 trillion which amounts to ~4% of global GDP. Therefore, to enhance corrosion resistance of stainless steel, methods like adding alloying elements to the base material and applying coatings on the surfaces of base substrates are employed.

Coatings are an efficient method to prevent metals from the corrosion. In recent years different types of coatings ─ metals, polymers, composites, and ceramics ─ have been widely used for corrosion protection. Metallic coatings create adverse environmental effects and cause galvanic corrosion due to electrically coupling of dissimilar metals. Organic coatings such as epoxy coatings, poly-urethane coatings, phenolic resin coatings, etc., are proven to provide long-term protection for metals in marine environments. However, these coatings generally suffer from issues such as easy aging, and environmental pollution when exposed to high-temperature marine environments (such as heat exchangers and gas turbines, etc.). Ceramic coatings are known for their hardness and durability, they can show better erosion, and wear resistance than organic coatings in harsh environments. Conventional ceramic coatings are prepared by deposition methods like CVD, PVD, thermal spraying techniques. Major drawbacks of these processes are high sintering temperatures (1700-2000 °C) to sinter powders and high equipment costs.

Therefore, to overcome the aforementioned demerits, this work uses polymer-derived ceramics (PDCs) coatings due to their superior properties: (i) a relatively low synthesis temperature (~700-1000 °C) to obtain thermochemically stable ceramics, (ii) PDCs can be coated on complex structures, (iii) microstructure can be tuned by changing precursor composition, and (iv) simple deposition methods can be used for coatings. Synthesis of PDCs is done using silicon-based polymeric precursors, such as polysiloxanes, polysilazanes and polycarbosilanes; pyrolysis of these precursors in the inert environment leads to the formation of silicon oxycarbide (SiOC), silicon carbonitride (SiCN) and silicon-carbide (SiC),

respectively. This thesis investigates the corrosion protection performance of two different coatings (SiOC and SiCN) on SS304 in 0.6 M NaCl solution.

The research work of this thesis is focused on:

(i) Synthesis and characterization of ceramics using polymer-pyrolysis route,

(ii) Optimization of coating parameters,

(iii) Enhancing corrosion protection behavior of amorphous SiOC- and SiCN-coated SS304

The content of this thesis is as follows:

Chapter 1. Literature Review: This chapter presents an overview about corrosion, corrosion mechanism of stainless steel, methods to improve corrosion resistance, introduces different types of coatings, a comprehensive literature survey related to polymer-derived ceramics and objectives of this thesis work.

Chapter 2. Experimental methods: This chapter discusses experimental procedures used for the synthesis of polymer-derived ceramics, ceramic coating depositing method on steels, various structural characterizations and electrochemical techniques used in this work.

Chapter 3. Synthesis and characterization of polymer-derived ceramics and optimization of coating layers on SS304 substrates: This chapter investigates precursors used for the synthesis of SiOC and SiCN. Structural characterization of as synthesized ceramic powders are discussed.

Chapter 4. Corrosion protection performance of polymer-derived SiOC-coated SS304: A polymer-derived silicon oxycarbide (SiOC) coating was deposited on SS304 and electrochemical corrosion behavior of the ceramic coated samples were studied in 0.6 M NaCl solution and compared with uncoated SS304.

Chapter 5: Corrosion protection performance of polymer-derived SiCN-coated SS304: This chapter discusses about enhanced corrosion protection of silicon carbonitride (SiCN) coated SS304. SS304 is dip-coated with a polysilazane solution followed by pyrolysis under argon environment at 800 °C to develop SiCN ceramic layer. Electrochemical characterization revealed that SiCN-coated SS304 had a significantly lower corrosion current density compared to that of uncoated SS304 samples.

Chapter 6. Conclusions and outlook: This chapter summarizes the present thesis work and underlines its prospective future by evaluating the obtained results. A brief discussion about the prospective future extension is also presented.

Chapter 1. Literature review

At present, metals and alloys form the basis for nearly all kinds of construction and structures in the world. In particular, steel is predominantly used in all sectors. SS304 is a widely used stainless steel grade and is considered as backbone material for modern industry. It is generally used in applications that require strength and good corrosion resistance, such as in subsea pipelines, desalination plants, and steel canisters [1]. Irrespective of the function, all common metals tend to react with their environments at different rates and, therefore, deteriorate over time due to corrosion, which refers to the gradual degradation of materials through an electrochemical reaction with an exposed/functional environment. Degradation through corrosion is causing significant economic losses worldwide, with a global cost of US $2.5 trillion per annum [2]. This loss includes the repair and replacement of parts, shutdown of plants, and in some cases catastrophic failures.

SS304 mainly suffers from localized corrosion (pitting and crevice corrosion) in chloride-containing environments. The corrosion resistance of SS304 is facilitated by the presence of a thin passive film of chromium oxide on its surface. Demand for improving the corrosion resistance of materials is increasing, and therefore, to enhance the corrosion resistance of stainless steel, methods like anodization, adding alloying elements to the base material and applying coatings on the surfaces of base substrates are employed. Among available methods, coating is a simple and economical process to prevent corrosion and improve the service life of the materials. Coatings can increase the corrosion resistance of substrate to provide specific functions to the system by modifying the surface properties.

1.1 Corrosion

Corrosion is defined as an irreversible interfacial reaction of material (metal, ceramic, polymer) with its environment which results in consumption of the material or dissolution into the material of a component of the environment. Basically, corrosion is the destructive result of a chemical reaction or electrochemical reaction of material and its environment [3]. In the periodic table, there are 85 metals and all common metals tend to react with their environments at different rates.

Corrosion has been classified in many different ways. One method divides corrosion into low and high-temperature corrosion, another method classify it as oxidation and electrochemical corrosion, sometimes also classified as wet corrosion and dry corrosion. Corrosion is mainly classified as chemical and electrochemical corrosion.

Chemical corrosion: Chemical corrosion occurs in the absence of a liquid phase. This type of corrosion is also known as dry corrosion, in which the constituents of the corrosion medium directly interact with the metal due to their chemical affinity of the metal.

Electrochemical corrosion: Difference in potential causes development of electric current due to the contact between dissimilar metals or difference in the concentrations of the electrolytes. Presence of water is the key factor for this corrosion to takes place.

1.1.1 Forms of corrosion

Various forms of corrosion are described in the following: schematic representation of corrosion types is shown in Figure 1.1. Later, each corrosion type is explained clearly.

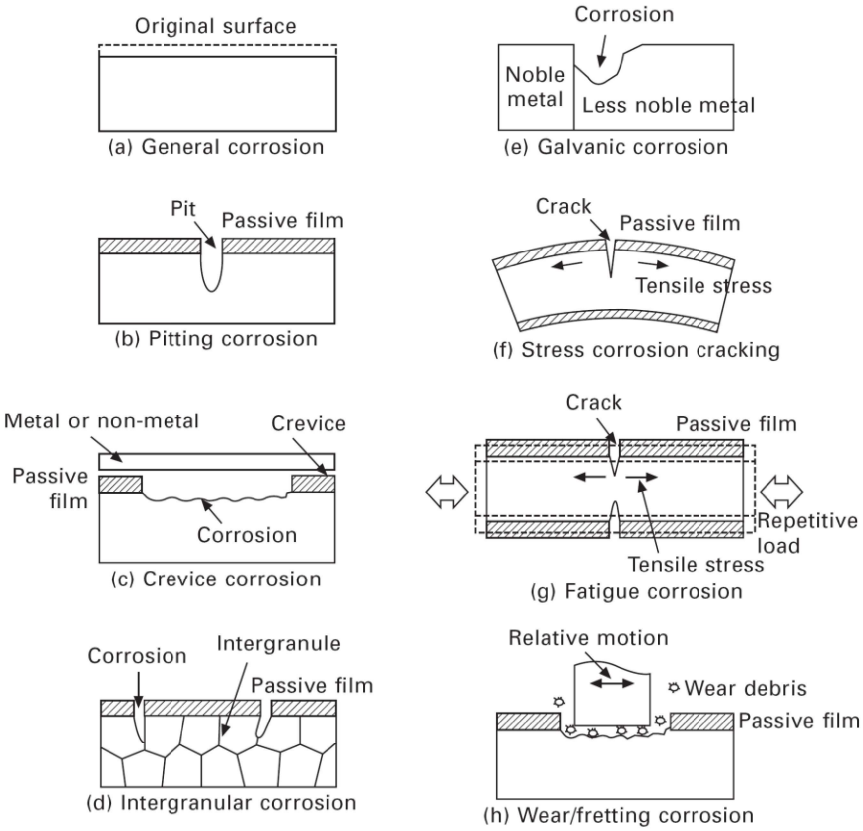

Figure 1.1 Schematic representation of different types of corrosion [4].

1) Uniform corrosion :

In this corrosion process, the entire metal is exposed to a corrosive environment, and it is converted to an oxide form. For example, aqueous corrosion of iron (Fe) in sulphuric acid and Zn in diluted Sulphuric acid. Both these metals dissolve at uniform rates according to anodic and cathodic reactions respectively,

Metal	Anodic reaction	Cathodic reaction	Overall reaction
Fe	$Fe \rightarrow Fe^{2+} + 2e^{-}$	$2H^{+} + 2e^{-} \rightarrow H_2 \uparrow$	$Fe + 2H^{+} \rightarrow Fe^{+2} + H_2 \uparrow$
Zn	$Zn \rightarrow Zn^{2+} + 2e^{-}$	$2H^{+} + 2e^{-} \rightarrow H_2 \uparrow$	$Zn + 2H^{+} \rightarrow Zn^{2+} + H_2 \uparrow$

here, $H_2 \uparrow$ is in gaseous form.

Figure 1.2 Uniform corrosion of a gate valve [5].

Figure 1.2 shows the uniform corrosion of gate valve used in the chemical transfer pipeline. In this scenario, aqueous solution causes extensive corrosion.

2) Galvanic corrosion:

Galvanic corrosion is either chemical or electrochemical corrosion. Later, one is due to the potential difference between the two different metals connected through a circuit, and current flow occurs between the more active (negative potential) metal and the more noble metal (more positive potential). In galvanic coupling, anode is more corrosive than the cathode.

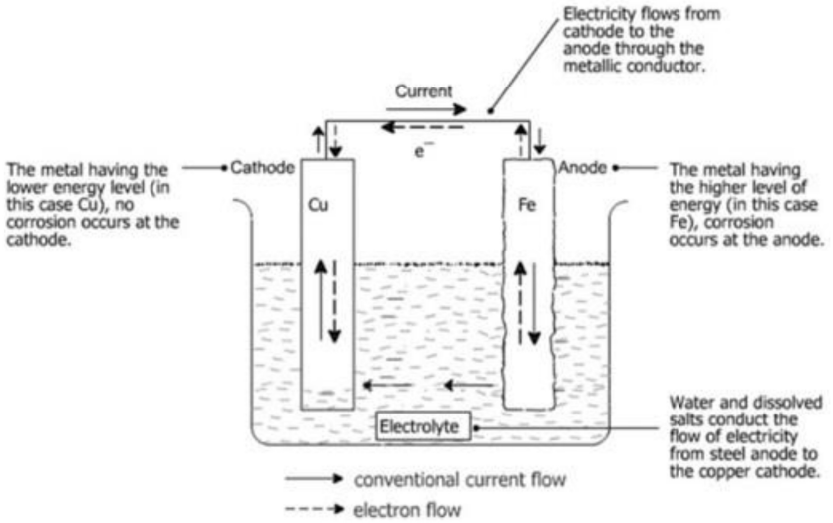

Figure 1.3 Schematic of galvanic cell [6].

Galvanic cell may have anode or cathode of dissimilar metals in electrolyte. For example, Figure 1.3 shows steel and copper electrodes immersed in an electrolyte. Noble metal copper acts a cathode and the iron acts as an anode, current flow occurs from iron to copper in the electrolyte. Slowly iron will get corroded.

Galvanic corrosion can be predicted using electromotive force (EMF). Metal reduction potential is measured against the standard hydrogen electrode (SHE), which is a reference potential whose potential is arbitrarily considered standard potential as a zero. To suppress the galvanic corrosion, both metals' potentials should be similar or close to each other in the galvanic series as shown in Table 1.1.

Table 1.1 Galvanic series of various metal and alloys in flowing seawater [7].

Alloy		*Voltage Range of Alloy vs. Reference Electrode**
Magnesium	**Anodic or Active End**	-1.60 to -1.63
Zinc		-0.98 to -1.03
Aluminum Alloys		-0.70 to -0.90
Cadmium		-0.70 to -0.76
Cast Irons		-0.60 to -0.72
Steel		-0.60 to -0.70
Aluminum Bronze		-0.30 to -0.40
Red Brass, Yellow Brass, Naval Brass		-0.30 to -0.40
Copper		-0.28 to -0.36
Lead-Tin Solder (50/50)		-0.26 to -0.35
Admiralty Brass		-0.25 to -0.34
Manganese Bronze		-0.25 to -0.33
Silicon Bronze		-0.24 to -0.27
400 Series Stainless Steels**		-0.20 to -0.35
90-10 Copper-Nickel		-0.21 to -0.28
Lead		-0.19 to -0.25
70-30 Copper-Nickel		-0.13 to -0.22
17-4 PH Stainless Steel †		-0.10 to -0.20
Silver		-0.09 to -0.14
Monel		-0.04 to -0.14
300 Series Stainless Steels ** †		-0.00 to -0.15
Titanium and Titanium Alloys †		+0.06 to -0.05
Inconel 625 †		+0.10 to -0.04
Hastelloy C-276 †		+0.10 to -0.04
Platinum †	**Cathodic or Noble End**	+0.25 to +0.18
Graphite		+0.30 to +0.20

* These numbers refer to a Saturated Calomel Electrode.
** In low-velocity or poorly aerated water, or inside crevices, these alloys may start to corrode and exhibit potentials near -0.5 V.
† When covered with slime films of marine bacteria, these alloys may exhibit potentials from +0.3 to +0.4 V.

3) Crevice corrosion :

Crevice is one of the common forms of corrosion. It generally occurs where a small amount of standing electrolyte solution is present, for example, between the flanges, bolts and nuts (Figure 1.4). The presence of chloride ions is highly conductive to crevice corrosion. The crevice must be wide to admit moisture and narrow to ensure a standing medium.

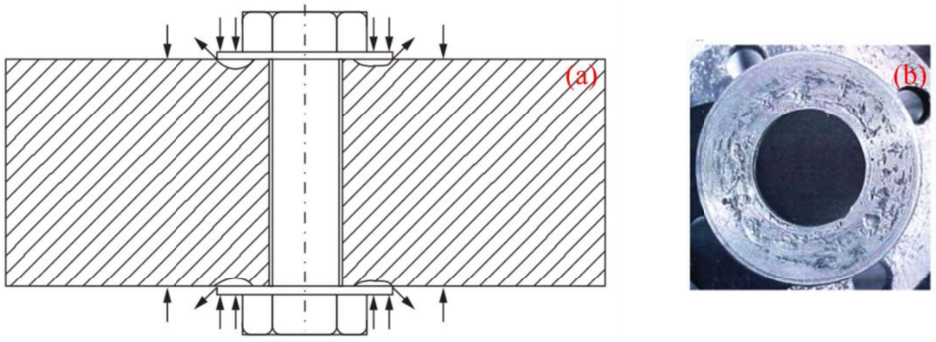

Figure 1.4 (a) Two metal plates are riveted, (b) corroded steel flange.

Crevice mechanism is described here. Consider two metal plates (M) which are riveted (as shown in Figure 1.4 (a)) together and located in the aerated seawater condition where pH = 7. The overall reaction consists of the dissolution of metal M and the reduction of oxygen to hydroxide ions:

$$\text{Oxidation: } M \rightarrow M^{+} + e^{-}$$

$$\text{Reduction: } O_2 + 2H_2O + 4e^{-} \rightarrow 4OH^{-}$$

All these reactions occur over the entire surface area and also inside the crevice, as shown in Figure 1.5 (a). After some time, oxygen inside the crevice will be consumed due to the absence of flow. Dissolution of Metal (M), continues inside the crevice (Figure 1.5 b). It results in a positively charged solution through which chloride ions migrate into the crevice. As a result, metal chloride concentration will increase inside the crevice. Further metal chlorides hydrolyse in water by forming an insoluble hydroxide and acid:

$$M^{+}Cl^{-} + H_2O \rightarrow MOH \downarrow + H^{+}Cl^{-}$$

Crevice is, therefore, an autocatalytic process.

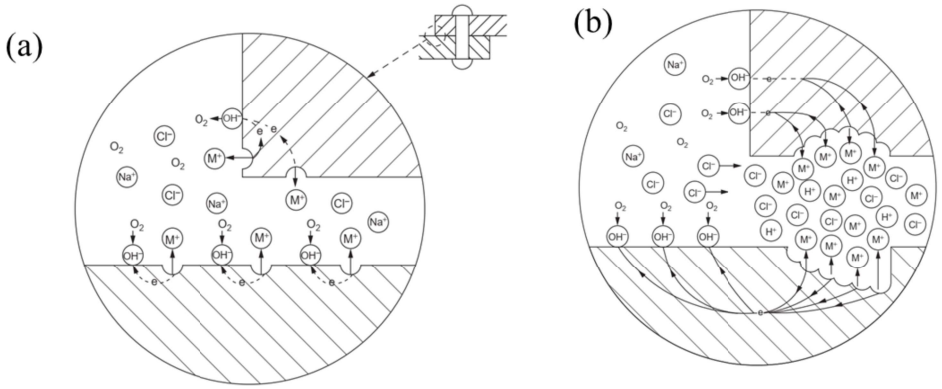

Figure 1.5 (a) initial stage of crevice corrosion, and (b) later stage of crevice corrosion [8].

4) Pitting corrosion :

Pitting corrosion affects the metal and alloys. Pitting corrosion is a cavity or hole that forms in a small area of the surface. During the corrosion, metal dissolution occurs, and the localized surface acts as an anode, and the surrounding material (passive layer) acts as a cathode; due to this, the localized anode dissolves by generating cavities known as pits.

Figure 1.6 shows the pitting of Fe in alkaline chloride solutions, abundant amount of positively charged Fe^{2+} ions attract negative anions, e.g., Cl^- to the pit initiation site. Positively charged Fe^{2+} ion attracts the negatively charged Cl^- ions to initiate the hydrolysis by

$$Fe^{2+} + 2H_2O + 2Cl^- \rightarrow Fe(OH)_2 + 2HCl$$

which produces local pH reduction by increasing the acidity level at the pit initiation site. Later, it results in the self-propagating of the pit growth mechanism, as shown in Figure 1.6. Anodic dissolution is further increased by acid chloride concentration in the pit, which in turn increases the chloride content in the pit. Formed metal hydroxide is unstable, and it further reacts with water to form a corrosion product.

$$2Fe(OH)_2 + 1/2O_2 + H_2O \rightarrow 2Fe(OH)_3$$

When Fe^{2+} diffuses out of the pit, insoluble $Fe(OH)_3$ corrosion product presents at the pit mouth oxidized to Fe^{3+}. Porous $Fe(OH)_3$ impedes the escape of Fe^{2+} but it allows the migration of Cl^- into the pit, thereby increasing the acid chloride concentration in the pit.

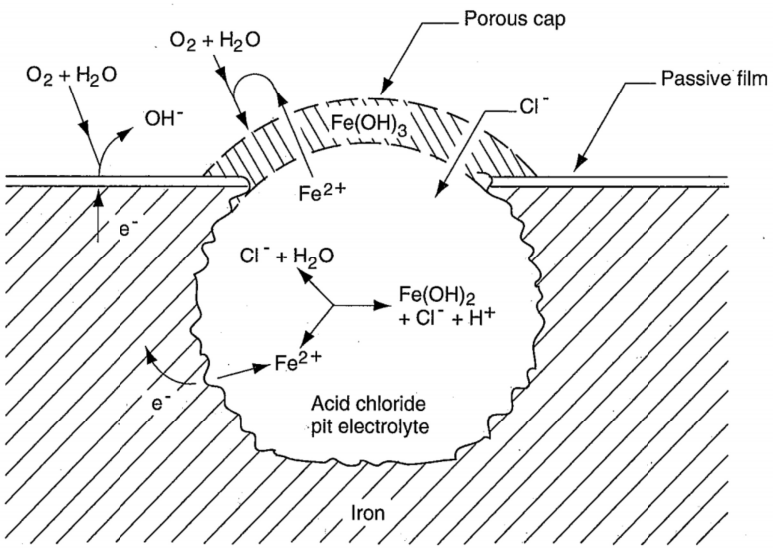

Figure 1.6 Schematic process occurring at an actively growing pit [8].

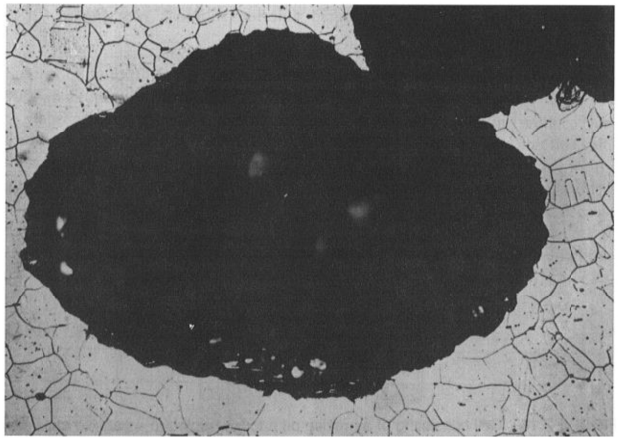

Figure 1.7 Pitting in type 304 stainless steel [8].

SS is susceptible to localized corrosion (pitting and crevice) in chlorine-containing environments due to the breakdown of the passive oxide layer on the surface. The pitting micrograph of 304 stainless steel is shown in Figure 1.7.

5) Intergranular corrosion:

When a stainless steel is heat treated at high temperatures, chromium (Cr) depletes near the grain boundaries by metallurgical reaction. At a temperature range of 425 to 815 °C, $Cr_{23}C_6$ (mainly) precipitates at the grain boundaries. Passivating element Cr may be depleted near the grain boundaries due to which regions near the depletion region being less corrosion resistant, and preferential corrosion happens at grain boundaries as shown in Figure 1.8.

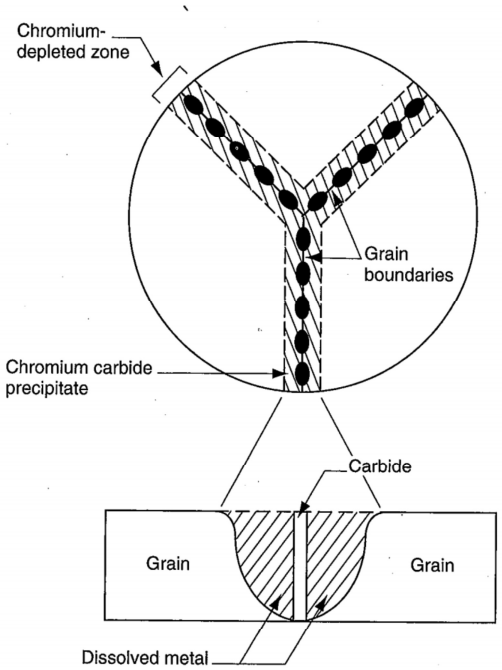

Figure 1.8 Schematic representation of carbide precipitation at grain boundaries [8].

6) Selective leaching:

An alloying element whose potential is negative is considered as the active material to the major solvent element and is likely to be corroded preferentially by selective leaching (or dealloying). Dealloying of brass (Figure 1.9), considered as dezincification, is a common and frequently used example. Zn is strongly active to copper and fastly leaches out of brass, and porous copper will be left out; Dark regions are material-lost regions.

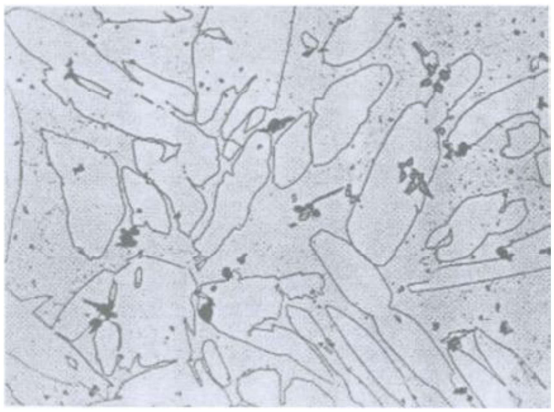

Figure 1.9 Dezincification of α-brass [9].

7) Erosion-corrosion:

Erosion occurs regularly in liquids-bearing systems. Even a small amount of corrosiveness of the system leads to damage strongly in a short interval due to synergy between corrosion and

often local-high fluid velocity. Low-strength alloys are more susceptible to erosion. The attack generally follows the direction of localized flow and turbulence around the irregularities in the surface. Presence of sediment particles in the centrifugal pumps significantly increase the erosion rate of the pump, which in turn reduces the efficiency and decreases the operational life of pump [10].

Figure 1.10 Erosion-corrosion of pump impellers [5].

1.1.2 Effect of environmental variables

i. *Effect of temperature:* Temperature change strongly influences the phenomena involved in corrosion, including product film formation (morphology, properties, and nature) and chemical and electrochemical reactions at the interface or bulk of the metal within the solution. An increase in temperature leads to an increase in chemical reactions and with a high mass transfer rate [11]. In pitting corrosion, temperature is the critical factor; below a certain temperature, many materials will not pit [12]. Pitting potential decreases with an increase in temperature and also a change in chlorine concentration [13].

ii. *Effect of pH and concentration:* In acidic solutions, decrease in pH leads to an increase in corrosion rate due to severe corrosive reactions because of an increase in acidity level. The corrosion rate is proportional to the concentration of solution.

iii. Effect of surface condition: Samples prepared with rough surfaces corrode faster than the polished sample. The effect of surface condition on corrosion is significant and care must be taken while collecting the experimental data. In the pitting corrosion, roughness plays a role. If surface is smoother then it reduces the occurrence of meta-stable pitting by decreasing the reactive sites on the surface [14].

1.2 Methods and parameters to evaluate the corrosion

Electrochemical techniques require a potentiostat and a three-electrode electrochemical cell set-up to perform a test. In general, to determine the electrochemical properties open-circuit potential (OCP) measurement, potentiodynamic polarization, and electrochemical impedance spectroscopy (EIS) measurements are preferred.

1.2.1 Three electrode system

American Society for Testing and Materials (ASTM) approved standard electrochemical polarization cell is shown in Figure 1.11 (a), which is currently available in slight variations also [15]. Working electrode (WE) is located in the middle of the cell with an auxiliary electrode (AE) for better current distribution. Reference electrode (RE) is placed outside the cell, and the potential of WE is measured through Luggin probe and solution bridge with respect to reference electrode.

In a conventional three-electrode set-up, potential (E) is controlled between WE and reference electrode (RE) and current (*i*) passes between counter electrode (CE) and WE. This set-up schematic can be seen in Figure 1.11 (b). The output of these measurements typically plots i on the X-axis and E (vs. RE) on the y-axis.

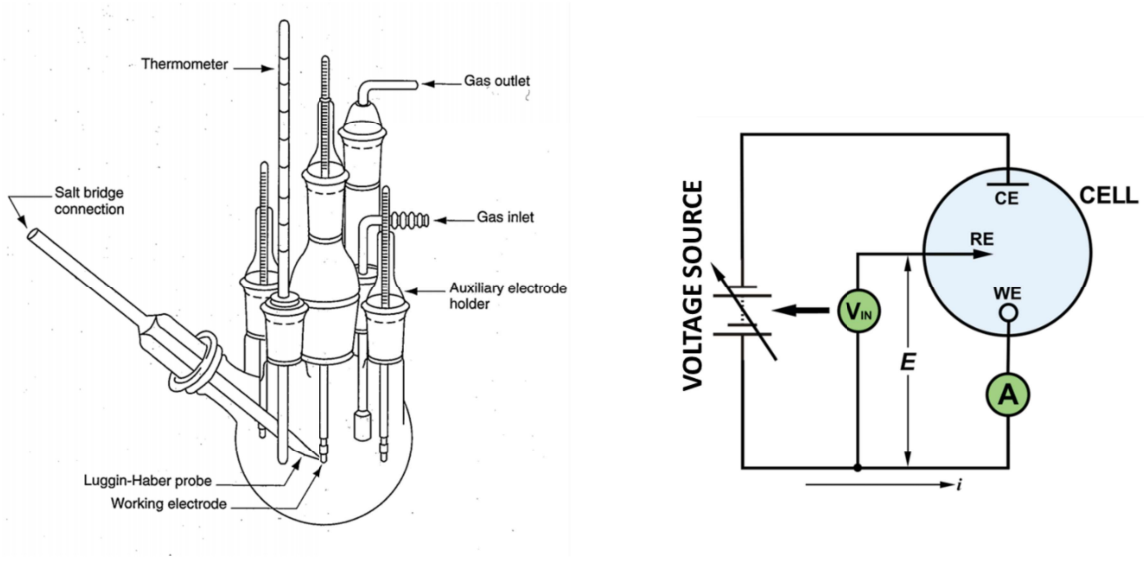

Figure 1.11 (a) Electrochemical polarization cell[8], (b) Schematic of typical three-electrode electrochemical set-up [16].

Functions of cell components and their functions are described here as follows:

Working electrode (WE): The sample to be tested is considered a working electrode; 1 cm^2 area of WE is desirable**.**

Platinum (Pt) Auxiliary Electrode (AE): It passes current to the working electrode (testing specimen) to be studied.

Reference Electrode (RE): It has a stable well-defined electrochemical potential which does not change during testing. It helps to measure the corrosion potential of the working electrode. Common reference electrodes are saturated calomel electrode (SCE) and silver/ silver chloride (Ag/AgCl).

Potentiostat: It is an instrument used for measuring the potential (E) and current density (i) and developing the E vs log (i) graphs (as shown in Figure 1.12) to evaluate the electrochemical parameters.

1.2.2 Electrochemical methods

Open circuit potential (OCP): When an electrode is immersed in an electrolyte without applying an external power supply, the measured potential difference between the electrode and reference electrode is called open circuit potential (OCP) or corrosion potential (E_{corr}). Both anodic and cathodic reactions are in equilibrium. At this stage, the net current passing through the electrode is zero. At the equilibrium state (potential is constant with the time) rate of oxidation and reduction reactions are equal. In general, the OCP value is not able to give much information about corrosion because it does not give information about corrosion kinetics. Some corrosion properties of electrodes can be evaluated using the OCP value. After immersion over a period of several minutes or hours, potential becomes constant due to attaining the equilibrium with the electrolyte environment. An increase in potential towards the noble direction indicates the metal is less corroded due to the barrier formation; if the OCP value falls to the negative direction then it corrodes faster [17,18].

Potentiodynamic polarization: In the potentiodynamic polarization method, potential of the working electrode is scanned in the defined potential range from several hundreds of mV below the OCP (cathodic direction) and above the OCP value. This testing requires three electrodes – Working Electrode (WE), Reference Electrode (RE), and Counter Electrode (CE). The obtained results of the test are plotted as potential versus current density. The results extracted from a potentiodynamic polarization measurement gives information about the passivity behaviour of the electrode, passivation current density, corrosion rate, corrosion current density

(i_{corr}), and corrosion potential (E_{corr}). One more important parameter is passive film break-down potential (pitting potential). The polarization test is a destructive technique because the applied potential range is sufficient to damage the electrode surface [17,18].

A typical polarization curve is shown in Figure 1.12. Different parameters obtained after potentiodynamic polarization measurement are explained below:

Corrosion potential **(E_{corr}):** Corrosion potential indicates a state where the rate of oxidation and reduction reactions are balanced, resulting in no current flow between the metal and electrolyte. E_{corr} value represents the material's susceptibility to corrosion. Generally, metals with more negative corrosion potential are more prone to corrosion than metals with more positive corrosion potential in the electrolyte system.

Corrosion current density **(i_{corr})***:* Corrosion current density is defined as the amount of current that passes through a unit area of a metal surface when it is exposed to the environment. It is generally measured in μA/cm^2. βa and βc are anodic and cathodic slopes.

Other parameters indicated in Figure 1.12 are

i_p = passive current density

i_{corr} = corrosion current density

i_s = secondary current density

i_{crit} = critical current density

i_{max} = maximum current density

E_{pa} = passive potential

E_{corr} = corrosion potential

E_{o2} = Oxygen evolution potential

E_{pp} = primary passive potential

E_p = pitting potential

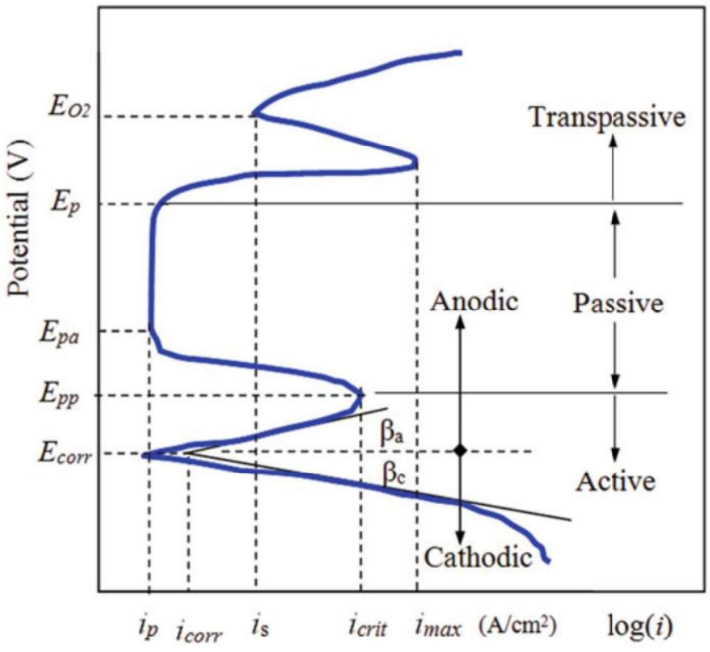

Figure 1.12 Schematic representation of a polarization curve [19].

Electrochemical impedance spectroscopy (EIS): During corrosion of an electrode, several complex chemical reactions occur at the surface, which cannot be predicted/understood by simple electrochemical testing. The EIS method is a widely used and powerful tool to investigate the electrochemical reactions and corrosion of the electrode surface, coatings, inhibitors, etc. This method also gives information about the transportation characteristics of electroactive species near the metal surface, film or coating properties. A small amplitude of AC sinusoidal potential (5-10 mV) and a frequency (10^3-10^6 Hz) is applied to the system and the output current signal is measured. Output results are the impedance of the interface between metal and the solution and data is fitted to an electrical equivalent circuit, which contain electrical elements like resistors, capacitors, inductors, etc. Figure 1.13 shows equivalent circuit model to fit a coated sample measured data. In this R_{sol} represents the solution resistance between the WE and RE. CPE_{dl} represents the double-layer capacitance formed between the metal surface and solution. There are so many factors that influence the impedance of the electrodes, such as roughness, concentration of the electrolyte, temperature, etc. R_{ct} represents the charge transfer resistance which is related to the corrosion rate; a higher value of R_{ct} means less the corrosion rate. CPE_{film} and R_{film} are the capacitance and resistance related to an oxide film on the steel surface, respectively [17,18,20].

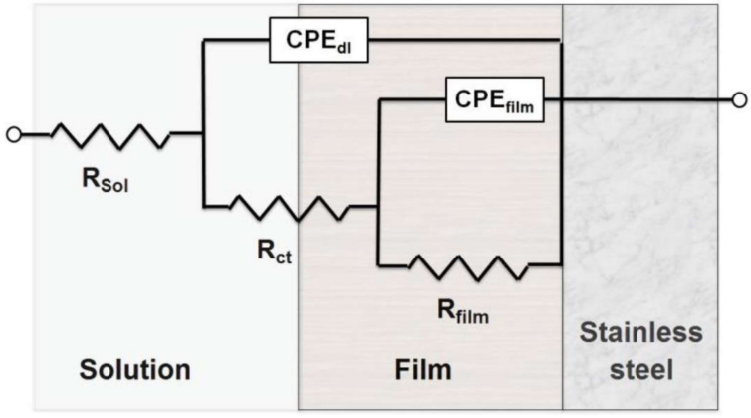

Figure 1.13 Schematic of an equivalent circuit to analyse the data [20].

1.3 Stainless steel

Applications of stainless steel (SS) are wide due to its high corrosion resistance in severe environments. Properties of SS vary depending upon its functionality in the environment. Corrosion resistance is affected by alloying levels, surface conditions, and steel microstructure.

Stainless steel is an iron-based alloy that contains at least 10.5 wt% chromium, and a maximum amount of carbon is 1.2 wt%. Chromium is the crucial alloying element in stainless steels. It forms a thin passive oxide layer on the surface (passive film), and it protects from corrosive environments. However, it is prone to localized corrosion, such as pitting corrosion in the presence of chloride ions [21,22]. Corrosion resistance is influenced by many factors, like alloying composition, electrolyte composition, operating temperature, pH, and electrode potential [23–27]. Other alloying elements like Molybdenum (Mo), Nickel (Ni), Manganese (Mn), Copper (Cu), Silicon (Si), and Carbon (C) are added to improve corrosion resistance and microstructure stability [28]. Cu enhances the corrosion resistance in acid environments. Small amount of Mo increases the pitting resistance of stainless steel in chloride environments. Si is added to improve the oxidation resistance and C is a strong austenizer which helps to improve the strength of the steel.

1.3.1 Classification of stainless steel

The Stainless-steel family is classified based on its microstructure: austenitic, ferritic, duplex, and martensitic, which contains both austenite and ferrite microstructure; the effect of alloying element contents varies in some aspects between the different types of SS. Currently, austenitic stainless steel (ASS) is considered for this work.

1.3.1.1 Austenitic stainless steel

ASS has a face-centred cubic crystal structure and is generally alloyed with nickel to promote the austenitic structure. SS contains 12-30 wt% Cr, and 1-25 wt% Ni and other minor alloying elements such as Mn and N. The advantage of adding Cr to steel is to create a thin passive (micron/nm) oxide layer and protect it from corrosion. Adding 2-3 wt% of Mo content gives the better corrosion resistance. However, it is susceptible to localized corrosion attacks (pitting corrosion) in the presence of chloride ions in the solution [29–31]. ASSs are available in different grades based on their alloy composition, namely SS304, SS316, SS310, and SS321, etc.

1.3.1.2 Ferritic stainless steel

Ferritic stainless steel is non-magnetic. It contains Cr (11-30 wt%) with less Ni (< 0.5%) in it. They are generally used in automotive parts and industrial machinery parts. These steels are highly resistant to stress corrosion cracking and also have good mechanical properties. The cost of ferritic steel is lower than austenitic grades [32].

1.3.1.3 Duplex stainless steel

Duplex SS contains equal amounts of austenite and ferrite, in general, the aim is to produce a 50/50 mixture of phases, but commercial alloys are also produced with 40/60 ratio. Cr content varies in 20-28%, Ni is 9%, C is < 0.03%, and Mo is about 5%. Other minor alloying elements are N, W, and Cu [33]. DSS has several applications due to its tensile strength, yield strength, corrosion resistance, low weight, and impact resistance. These steels are used in automotive, marine, petrochemical, and thermal powering industries.

Among various types of stainless steel, austenitic stainless is widely used. In this thesis work, SS304 is chosen as the base substrate to improve the corrosion resistance in a seawater environment.

1.4 Corrosion of SS304 in chloride-containing environments

Stainless steel 304 (SS304) is widely used in various areas (chemical industries, marine environments, naval applications, etc.) due to its good corrosion resistance in many environments and weldability. Marine environment applications of SS304 are in desalination plants [1], subsea pipelines, structures built in marine urban environments, and storing of spent nuclear fuel tanks in coastal regions [29,30]. In all these places, the presence of chlorine ions (Cl^-), humidity, and temperature play a key role in the lifetime of a component. Due to the presence of chlorine ions, localized failure takes place.

SS304 suffers mainly from pitting and crevice corrosion in chloride-containing environments. The presence of thin passive oxide film on SS304 gives corrosion resistance. It is a well-known fact that pitting occurs when the localized breakdown of the passive film occurs and it further leads to the failure of the component; this is promoted by chlorine ions in the solution acting as a physical point of weakness in the material. When the part of the passive film is affected by ions, the other part of the passive film remains the same. Here, a galvanic couple is formed on the steel, and corrosion happens at an intensified rate and this is called pitting corrosion [31]. This breakdown leads to different forms of corrosion and corrosion mechanisms (pitting and crevice) in aqueous solutions. It is reported that the formation of pits (passive oxide layer breakdown and devolvement of pitting potential) in SS304 occurs at potentials above 0.22 V vs Ag/AgCl [34].

Dissolution of passive film makes film thinner at local sites. This dissolution continues until the metal is reached and the pit formation initiates. In the second stage, pit propagation phase, once pit initiation is started localized dissolution continues further. Here, the unprotected area becomes an anode, and the surrounding surface becomes a cathode where the potential

difference is generated between the pit and the surrounding area. Pits that are initiated and passivated are called metastable pits. If dissolution is continuously taking place then no repassivation takes place. Anode and cathode area differences will occur and high local corrosion happens at the pit. When the pit continues to grow, self-acidification leads to a decrease in pH in the pit, which later hinders the repassivation process [5-7]. Further it promotes Cl^- ions to migrate into the pit and decreases the pH of the electrolyte inside the pit, which leads to increase in the corrosion rate in the pit and as result pitting corrosion. A schematic representation of pit formation is shown in Figure 1.14.

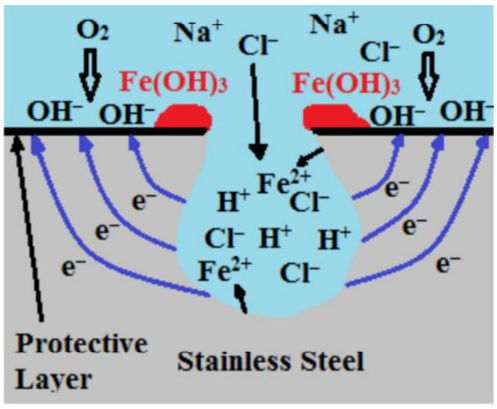

Figure 1.14 Mechanism of pitting corrosion in stainless steel [35].

During the pitting anodic and cathodic reactions take place which includes the dissolution of ferrous phase as follows:

$$\text{Anodic reaction: } Fe \rightarrow Fe^{2+} + 2e^-$$

In cathodic reaction, consumption of electrons produced in the anode reaction takes place (in neutral media)

$$^1/_2\, O_2 + H_2O + 2e^- \rightarrow 2OH^-$$

$$\text{Overall reaction: } Fe + {}^1/_2\, O_2 + H_2O \rightarrow Fe(OH)_2$$

Passive layer breaks due to chloride ions in the solution, and chloride ions reacts with iron to hydrolyze to hydrochloric acid and it worsens the corrosion attack.

$$FeCl_2 + 2H_2O \rightarrow 2HCl + Fe(OH)_2$$

In the presence of oxygen, $Fe(OH)_2$ oxidized to $Fe(OH)_3$ by

$$2Fe(OH)_2 + {}^1/_2\, O_2 + H_2O \rightarrow 2Fe(OH)_3$$

Using potentiodynamic polarization measurement (Figure 1.15), pitting potential can be identified. Pitting occurs at a critical potential (E_{pit}) or breakdown potential. Presence of

chloride in the solution increases the anodic current at all potential, but most singular feature is dramatic increase in the current density at the E_{pit} as shown in Figure 1.15. The more noble is the E_{pit}, the more corrosion resistant is the material. Figure shows two curves, one in the presence of Cl^- and other without Cl^-, it can be seen that with Cl^- breakdown potential or E_{pit} occurs at lower potentials.

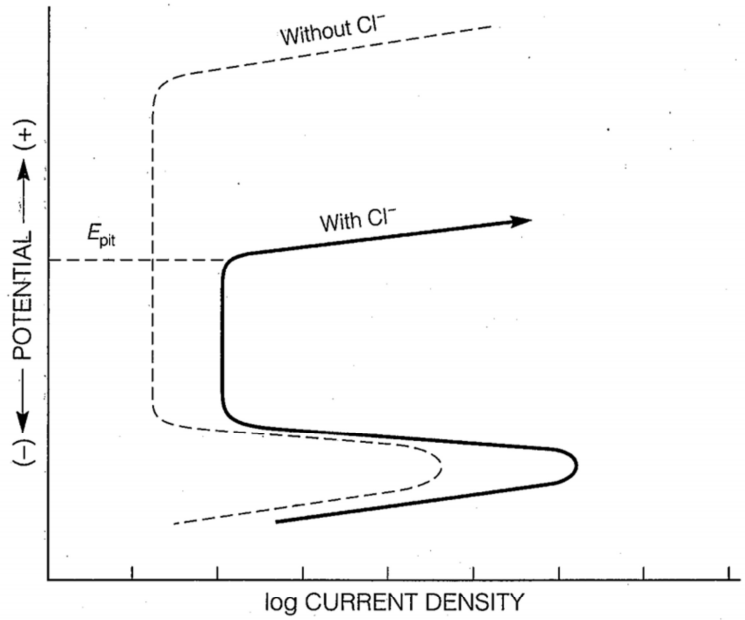

Figure 1.15 Schematic determination of critical pitting potential (E_{pit}) from anodic polarization [8].

1.5 Methods of corrosion prevention

There are several methods available to control rate of corrosion, such as anodic protection, cathodic protection, alloying, inhibitors and coatings. The current section discusses corrosion prevention methods. However, it is important to think about the usage of these prevention methods depending upon the situation, where the metal or alloy is going to be used.

1.5.1 Anodic protection

Anodic protection is used to reduce the corrosion of metal by polarizing it into its passive region and holding it there. The impressed current anodic protection for a steel storage vessel containing sulfuric acid is shown in Figure 1.16. Design parameters and operating conditions for anodic protection are determined by experimental measurements and polarization tests. Power supply protects the tank by applying constant potential between the tank and the $Hg/HgSO_4$ reference electrode.

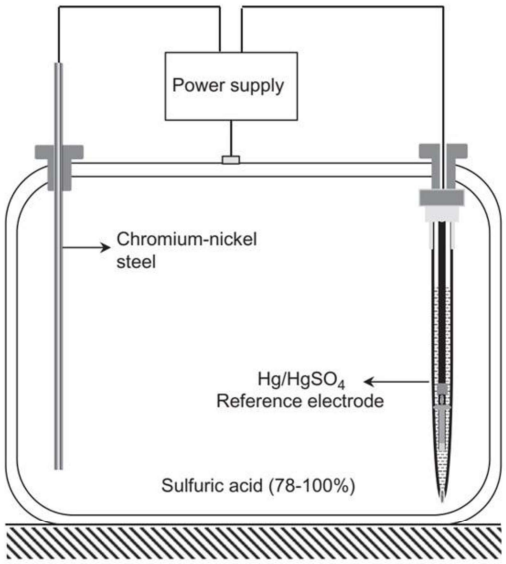

Figure 1.16 Schematic of anodic protection system for sulphuric acid storage tank [36].

1.5.2 Cathodic protection

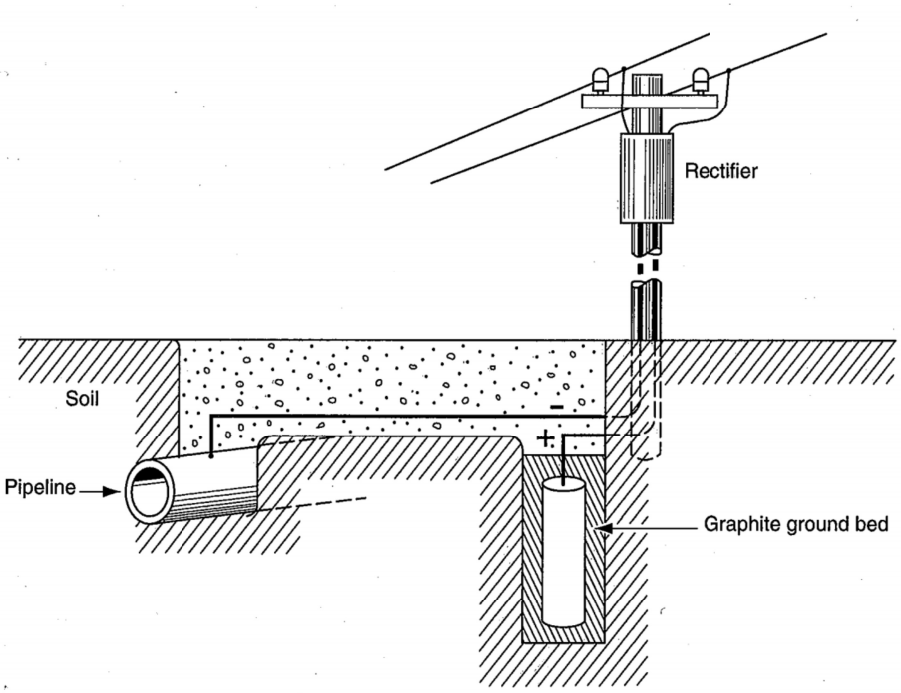

Figure 1.17 Cathodic protection by the impressed current [8].

It is one of the widely used methods to prevent corrosion of metal or alloy exposed to an aqueous electrolyte. Cathodic protection reduces corrosion by cathodically polarizing the

corroding metal surface. Consider iron in the dilute aerated neutral electrolyte solution. Anodic and cathodic reactions are

$$Fe \rightarrow Fe^{2+} + 2e^{-}$$

$$O_2 + 2H_2O + 2e^{-} \rightarrow 4OH^{-}$$

Cathodic polarization reduces the rate of iron dissolution with an excess of electron supply which also increases the rate of oxygen reduction and OH^- production by cathodic reaction. Impressed current is supplied by a rectifier for cathodic polarization by converting the alternating current (AC) from the power lines to the direct current (DC), as shown in Figure 1.17.

A metal structure is cathodically protected by connecting to the second metal (sacrificial anode), which has a more active corrosion potential. The more noble structure in this galvanic coupling is cathodically polarized, while the other one is anodically dissolved. An example is shown in Figure 1.18 for protecting the buried pipeline by using magnesium (sacrificial anode).

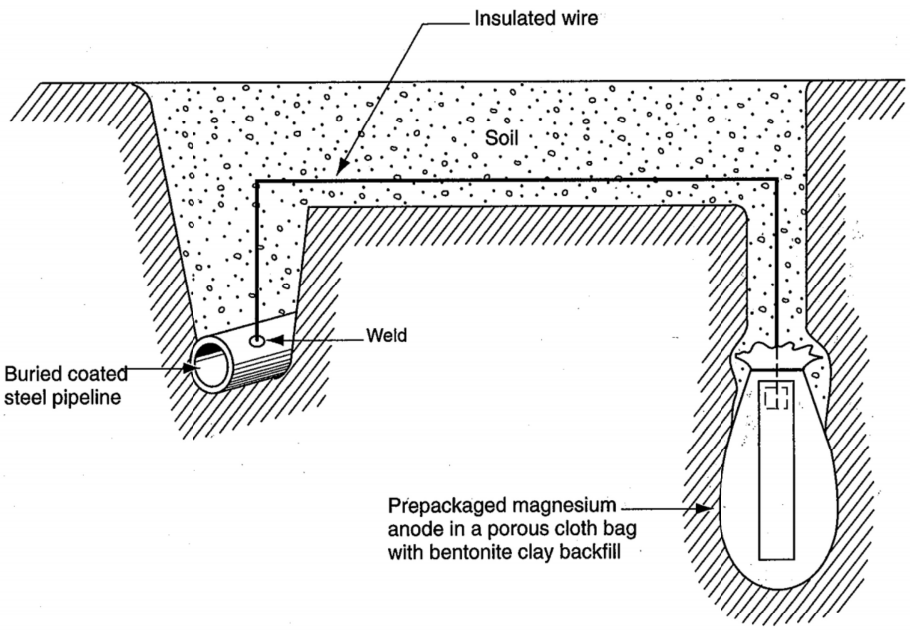

Figure 1.18 Cathodic protection with a sacrificial anode (Mg) [8].

1.5.3 Alloying elements

The alloy composition of stainless steel (SS) has a strong effect on the susceptibility to corrosion. Cr is the essential alloying element in SS because it gives a passivity to SS. An insufficient amount of Cr cannot prevent the corrosion of SS. The high amount of Cr increases

the pitting potential and increases the passive film stability. Addition of alloying elements improves the corrosion resistance.

1.5.4 Inhibitors

An inhibitor is a substance that decreases the corrosion rate in a specific environment when added in small concentrations to the electrolytic environment. It means it functions as a retarding catalyst. Corrosion mechanism by inhibition is shown in Figure 1.19. It shows a proposed model for carbon steel corrosion inhibition in freshwater using biocides (BC) and corrosion inhibitors combination of Zinc chloride ($ZnCl_2$), phosphoric acid (H_3PO_4), sodium molybdate (Na_2MoO_4) and ionic liquid.

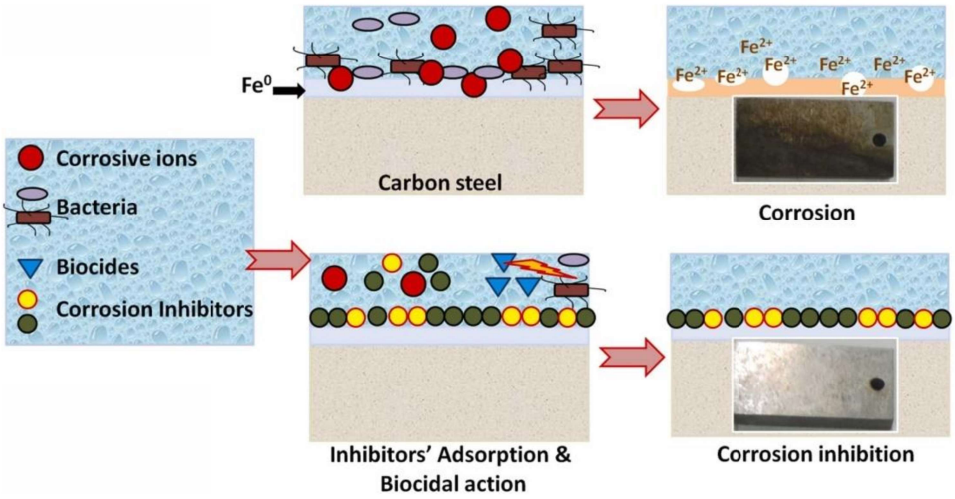

Figure 1.19 Proposed model of carbon steel corrosion inhibition in freshwater with corrosion inhibitor and Biocides (top row) and corrosion inhibition formed molecular monolayer on carbon steel and Biocides (bottom row) [37].

1.5.5 Coatings

Corrosion protection by coatings is the most efficient, cost-effective, flexible, and straightforward method to enhance corrosion resistance. Coatings act as a barrier between the exposed environment and the substrate and it leads to the improvement of corrosion resistance. Different coatings are available to increase the corrosion resistance of components in different environments, which are polymeric coatings, metallic coatings, composite coatings, and ceramic coatings.

1.5.5.1 Polymeric coatings (or organic coatings)

Organic coatings are employed to increase the corrosion resistance of metals for a long time. The major purpose of the organic coating is to function as a physical barrier against aggressive

species. However, all polymeric coatings are not impenetrable to electrolyte species; few defects in the coatings will work as a pathway for the corrosive species to attack the metallic substrate and lead to localized corrosion. To increase the diffusion path length for oxygen and water molecules pigments with different shapes, such as micaceous iron oxide and aluminum flake, are introduced. In literature, a number of electrochemical studies have been used as tools to evaluate the organic coatings performance, including electroactive (e.g., polyaniline) or non-electroactive (e., polyesters) polymers. The advantages of polymer are low processing cost and can be deposited using simple deposition methods, however, the final polymer coating usually suffers from low hardness and reduced chemical and thermal stability. In Table 1.2, a few earlier studies on polymer coatings to enhance the corrosion resistance of mild steel, steel and other materials are listed.

Table 1.2 Polymer coatings on metal and alloys.

Coating material	Corrosion monitoring technique	Metal/Alloy used	Medium used	Protection efficiency	Reference
Polyaniline	Tafel, EIS	Mild steel	HCl	Not measured	[38]
Polypyrole	Potentiodynamic polarization	Pt, Au, Cu, Ti, SS, Fe	20 non-aqueous and aqueous electrolytes	90%	[39]
Polyaniline	Chronoamperometry	Steel	Oxalic acid	Not measured	[40]
Polyaniline	Potentiodynamic polarization	Mild steel	H_3PO_4	Not measured	[41]
Polyaniline	Galvanostation polarization	AA3004	Oxalic acid	97.6%	[42]
CrN and diamond-like carbon	Physical vapour deposition	Mild steel	Sodium tatrate	75%	[43]
Polyaniline	CV or galvanostatic	Mild steel	H_2SO_4	Not measured	[44]

1.5.5.2 Metallic coatings

Processing metallic coatings is usually more costly and complicated than polymeric coatings, and although metallic coatings have good electrical and thermal conductivity, they possess limited corrosion and oxidation resistance. Metallic coatings can be classified into two - those

which are more active than the base substrate and those more noble than the base substrate. For example, to protect steel, the first groups that can be used are zinc and aluminium. These coatings act as sacrificial anodes. In another case, more noble coatings include chromium, nickel, and copper. These coatings are used to provide luster, hardness and electrical conductivity [45]. In Table 1.3, selected reported studies on metallic coatings and corresponding corrosion current density are mentioned.

Table 1.3 Zn and Zn-alloy composite coatings.

Zn/Zn-X	Second phase	Substrate	System	Mode of deposition	E_{corr}, V (SCE)	i_{corr}, µA/cm^{-2}	References
Zn	CeO_2	Mild steel	Chloride	Direct current and pulse current	-1.127 & -1.147	3.56 & 0.69	[46]
Zn	$TiO_{2.5}$	Steel	Sulfate	Direct current and pulse current	-1.052 & -1.118	2.7 & 15.1	[47]
Zn-Ni	TiO_2	Steel	Citrate	Galvanostatic	-0.90	176	[48]
Zn-Fe	Graphene	Mild steel	Sulfate	Direct current	-1.087	19.20	[49]
Zn-Co	CNTs	Mild steel	Sulfate	Direct current	-0.901	0.156	[50]

1.5.5.3 Ceramic coatings

Conventional ceramic coatings can be prepared using CVD, PVD and thermal spray processing. The end product will have high thermal resistance, better hardness, wear resistance, and better oxidation and corrosion stability. The main disadvantages of conventional ceramic coatings are the high processing cost, high sintering temperatures (~1700-2200 °C) to get ceramics and high energy consumption [51,52].

Table 1.4 List of various ceramic coatings on steel.

Coating material	Corrosion monitoring technique	Base substrate	Electrolyte	E_{corr} (mV) & i_{corr} (µA/cm^2)	Reference
ZrN/ZrO_2	Potentiodynamic polarization	304 SS	3.5 wt%NaCl, 10 wt% HCl and 20 wt% HCl	-382 (vs SCE) and 0.0161.	[53]

				-335 (vs SCE) and 0.082	
TiO_2	Potentiodynamic polarization & EIS	304 SS	0.1 M HCl	143 (vs SCE) and 6.6	[54]
TaON	Potentiodynamic polarization and EIS	304 SS	2.5 M HCl	-337 (vs Ag/AgCl) & 20.80	[55]

1.6 Polymer-derived ceramics

In the last few decades, polymeric-derived ceramics (PDCs) have gained good attention due to their advantages over conventional ceramic processing routes. In contrast to the above-mentioned coatings, polymer-derived ceramic (PDC) coatings have high thermal resistance, better hardness, wear resistance, and better oxidation and corrosion stability. In PDCs, complex structures can be coated due to liquid precursors, and ceramic can be obtained at relatively low synthesis temperatures (~800-1000 °C). Ceramic coatings can be applied using simple spin and dip-coating methods.

The foundation for developing PDCs is started by Ainger and Chanttrell in the 1960s by pyrolyzing the polymer precursors [56]. Verbeek and colleagues successfully developed the Si_3N_4/SiC ceramic fibers from precursors in the early 1970s [57]. Then, in the mid-1970s, Fritz and Yajima produced the SiC ceramics by pyrolyzing the polycarbosilane, this process greatly promoted the development of PDCs. The most commonly available commercial precursors are silicon-based polymers, which include polycarbosilane, polysiloxane, polysilazane, and polycarbosilazane. Silicon-based preceramic polymer is classified as shown in Figure 1.20.

Formation of PDCs consists of mainly three main steps : (i) synthesis of preceramic polymer; (ii) cross-linking of the polymer at moderated temperature to get organic/inorganic network; (iii) ceramization process of the cross-linked polymer – polymers are converted to inorganic amorphous/crystalline materials depending of the pyrolysis temperature between 800 °C to 1800 °C. One of the main advantages of using PDCs route is — control over the final composition of ceramic using different preceramic polymeric precursors, cross-linking and pyrolysis conditions.

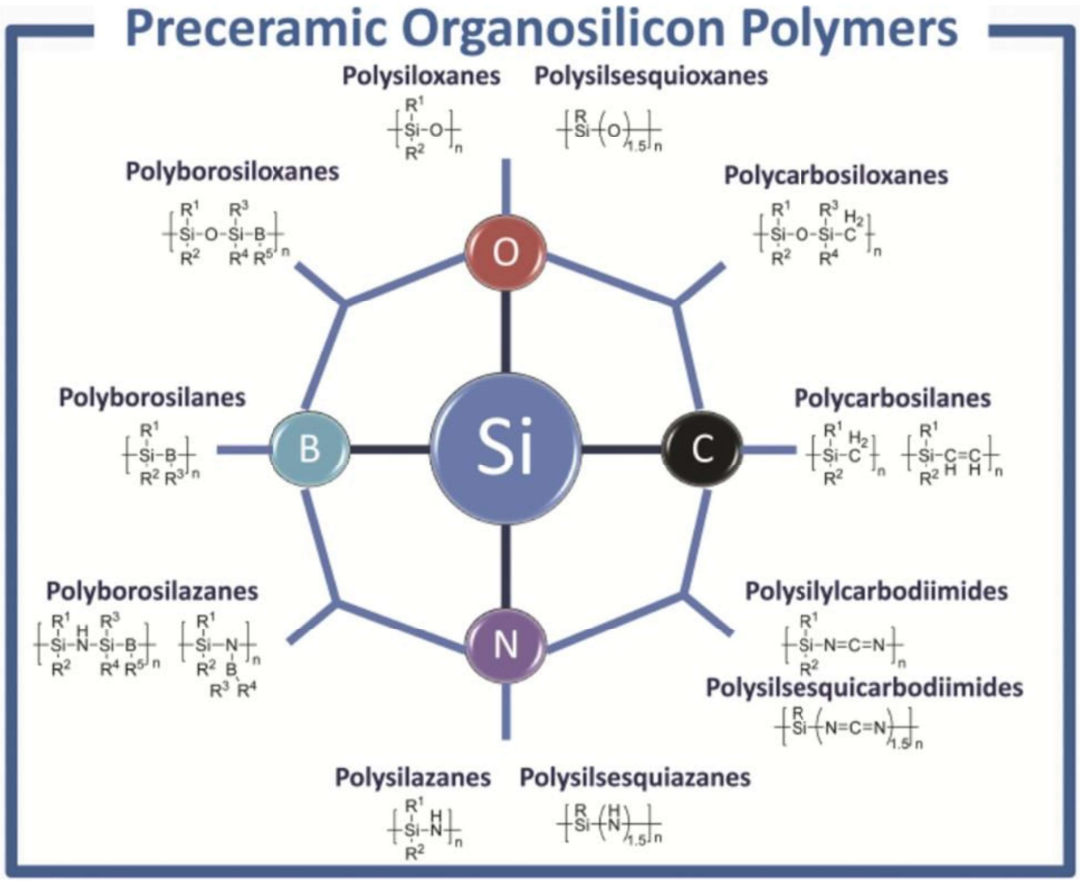

Figure 1.20 Main classes of Si-based precursor for ceramics: polysilazanes, polyborosilazanes, polyborosilanes, polyborosiloxanes, polysiloxanes, polycarbosiloxanes, polysilylcarbodiimides, etc [51].

Chlorosilanes R_xSiCl_{4-x} (x=0, 1, 2, 3) are the most commonly used starting material used for the synthesis of above shown different preceramic organosilicon polymers (Figure 1.21). The monomer used in the synthesis of organosilicon polymers contains active sites such as Si-H, Si-Cl, Si-C=C, which allows polymerization by means of elimination, substitution or addition reactions. These polymers are generally produced in large scale by the Müller-Rochow process — involving the reaction of gaseous methyl chloride with silicon, containing copper as catalyst in a fluidized-bed reactor at 250-300 °C. Different synthesis routes of organochlorosilicon polymers are shown in Figure 1.21.

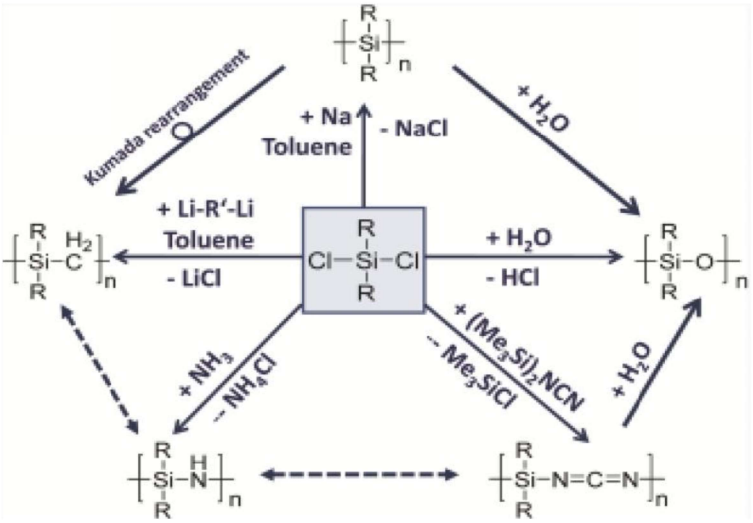

Figure 1.21 Synthesis routes of most representative classes of Si-based preceramic polymers from organochlorosilanes [58].

The second step in the processing of PDCs is a cross-linking process [58]. During this step, polymeric precursors are converted into organic/inorganic materials at low temperatures (150–300 °C). This transformation prevents the loss of low molecular weights of components (monomers) of the precursors, and thus increases the ceramic yield. Various reactions occurring during cross-linking of polysilazane is illustrated in Figure 1.22. Crosslinking reactions occurred in the organosilicon polymers are shown in Figure 1.22.

Cross-linking of polysilazanes occurs via four major reactions: transamination, dehydrocoupling, vinyl polymerization and hydrosilylation. *Hydrosilylation* reaction occurs for the precursors, which contain Si-H and vinyl groups, which leads to formation of Si-C-Si and Si-C-C-Si bonds. This is a fast reaction which can even occur starting from 100-120 °C. Higher ceramic yield as well as higher carbon can be achieved in the final ceramic due to hydrosilylation reaction [59]. *Dehydrocoupling* of Si-H/N-H or Si-H/Si-H lead to Si-N and Si-Si bond formation and hydrogen evolution. This reaction generally starts at 300 °C. Vinyl polymerization occurs at higher temperatures with no mass loss. Transamination reactions (200–400 °C) are associated with the evolution of amines, ammonia etc., and hence mass loss occurs. This reaction leads to a decrease in nitrogen content.

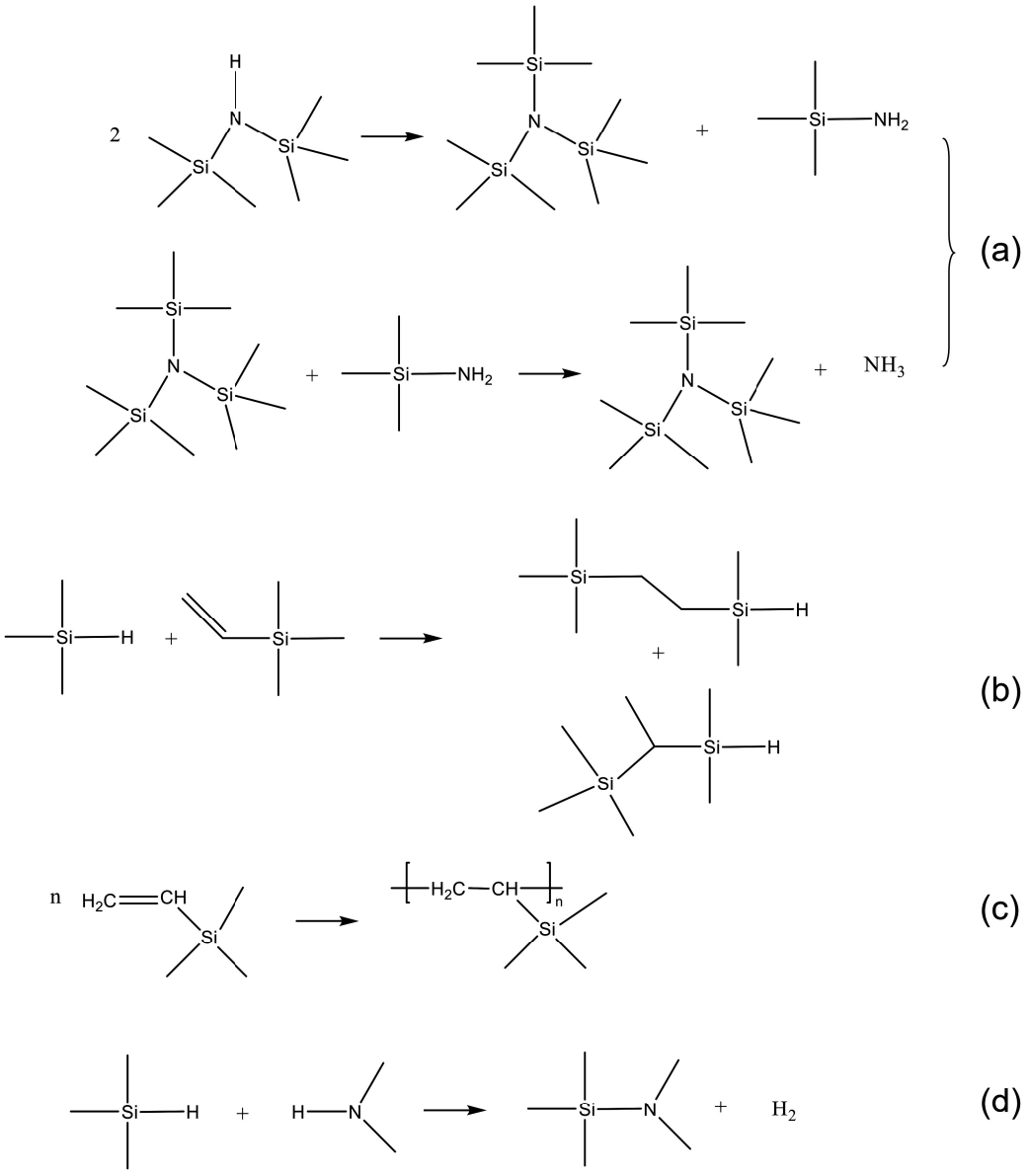

Figure 1.22 Cross-linking reactions of polysilazanes: (a) transamination, (b) hydrosilylation, (c) vinyl polymerization, (d) dehydrocoupling (adapted from reference [58]).

During the last step, polymer-to-ceramic conversion, thermal decomposition of basic organosilicon polymer occurs [58]. The ceramization process of cross-linked precursors involves thermolysis and volatilization of their organic groups in the temperature range of 600–1000 °C, which finally transforms into amorphous ceramics. Investigation of volatile species and fragments of the decomposition products during organic/inorganic transformation is monitored by simultaneous thermal analysis coupled by mass (TGA) and FTIR/MS spectrometery. During ceramic formation evolution of gases, such as, CH_4, H_2, etc. Polymers undergo densification during the ceramic transformation. During the conversion process, along with an increase in density, mass loss occurs, which implies the volume of materials decreases.

Change in mass and volume is affected by two main effects mainly shrinkage and porosity. During the early stages of ceramization, gases release leads to the development of open pores; few of them may disappear during the thermal treatment, it is due to shrinkage of the parts. This type of porosity is called as transient porosity; however, some residual porosity may retain in the final product.

Consider organosilicon as example, and the process for obtaining polymer to ceramic occurs in several stages as shown in Figure 1.23.

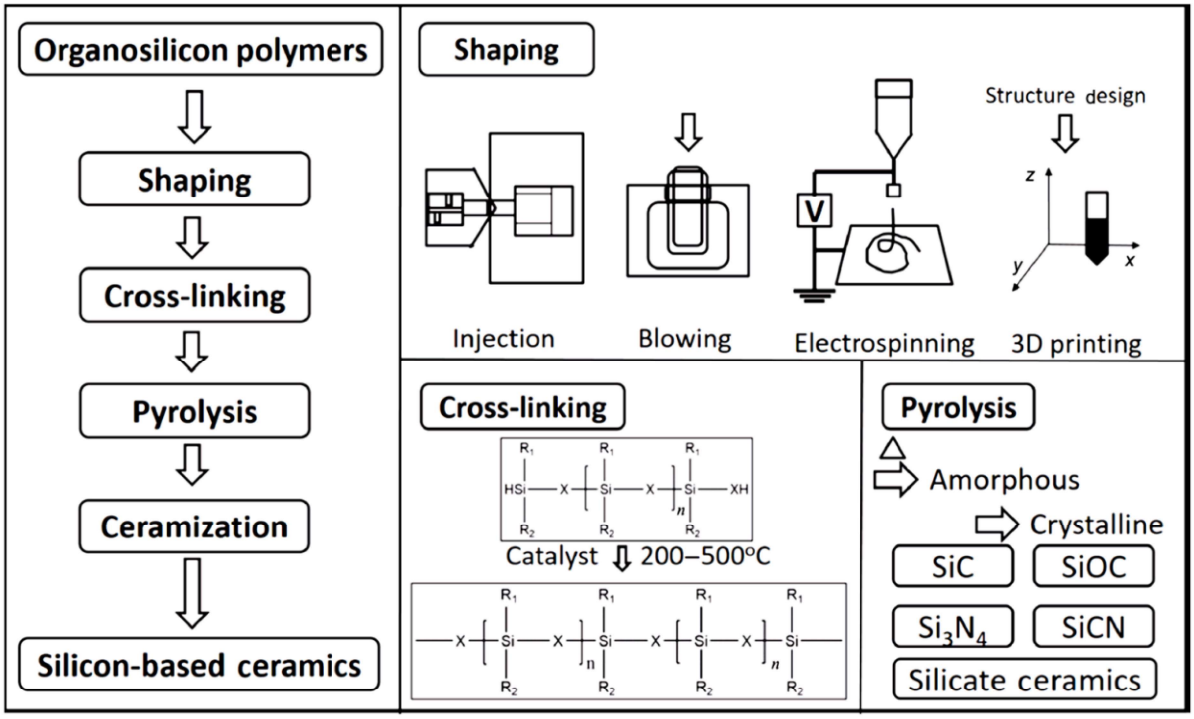

Figure 1.23. Preparation of ceramic products by PDCs technology [60].

Thermal decomposition behavior of different organosilicon polymers is illustrated in Figure 1.24. After thermal treatment above 700 °C, preceramic polymers like polycarbosilane, polysiloxane and polysilazanes/polysilylcarbodiimides are transformed to amorphous SiC, $Si_xC_yO_z$ and $Si_xC_yN_z$ ceramics, respectively.

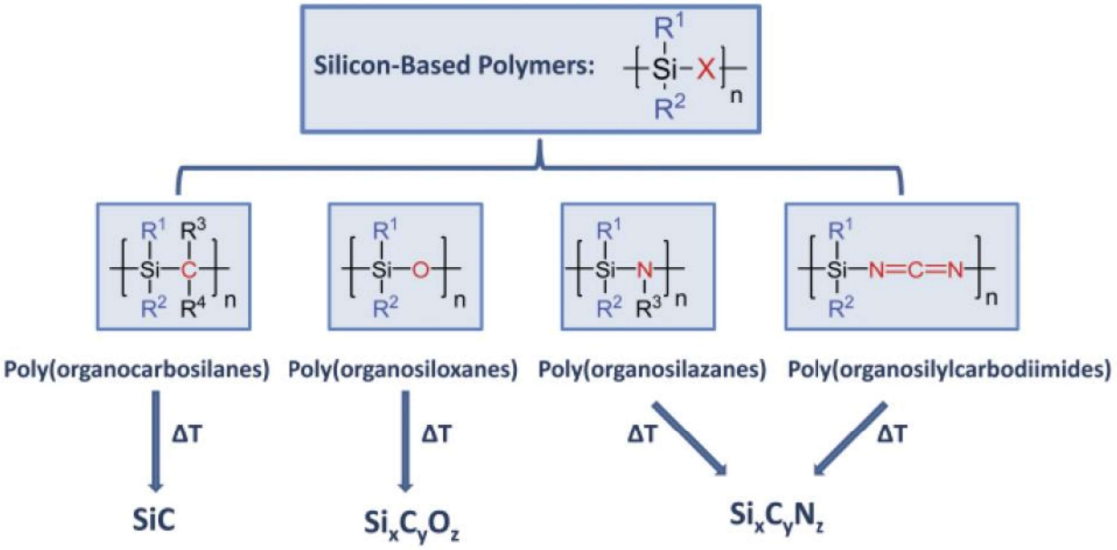

Figure 1.24 Thermal decomposition of silicon-based polymers [51]. Polymer-derived silicon carbide (SiC), silicon oxycarbide ($Si_xC_yO_z$) and silicon carbonitride ($Si_xC_yN_z$) ceramics are obtained after the thermal treatment of polycarbosilane, polysiloxane and polysilazanes/polysilylcarbodiimides, respectively, at T ≥ 700 °C under inert atmosphere (Ar or N_2).

Coatings based on Si-based polymers have higher thermal stability and high chemical resistance when compared to most organic coatings. Some important criteria must met to enable the preparation of silicon polymer coating [61]. Initial precursors must be available in liquids or have appropriate solvents to enable the coating deposition in a liquid state. Another aspect of getting ceramic coating is latent reactivity, which induces the crosslinking upon pyrolysis. Latent reactivity is related to unsaturated organic groups such as Si-H or N-H. To prevent the volatilization of compounds, sufficiently high molecular weight is required.

1.6.1 Structure and Properties of PDCs

PDCs exhibit an amorphous structure at low temperatures with many other properties, such as high thermal stability [51] [63], better semiconducting [64], oxidation and corrosion resistance [51], light transmission and luminescence [65]. At higher temperatures, PDCs gradually crystallize. Considering the advantage of the structural evolution of PDCs at high temperatures, mechanical properties can be improved by controlling the structure and distribution of ceramic nanoparticles [66]. Owing to the presence of the free C phase in the structure, PDCs are typically black; few reports on the optical properties of PDCs reported white silicon oxycarbide formulation, free of segregated sp^2-carbon [62].

High-Thermal Stability (HTS): Thermal stability is the ability of a material to resist thermal decomposition [67]. Traditional silicon-carbide materials possess HTS and good strength at high temperatures; however, Si_3N_4 decomposes into Si and N_2 above 1400°C, which limits the application of this material at high temperatures [68]. Si_3N_4 prepared via the PDCs route can remain stable up to 1800 °C temperature range, which also has better HTS [68].

Oxidation Resistance: In the literature, several in-depth studies on the oxidation behaviour of SiC, SiOC, SiCN, and SiBCN were reported**.** Wang et al.[69] studied the oxidation and hot-corrosion behaviour of SiC and reported that SiC shows a parabolic oxidation trend in the temperature range of 800 to 1400°C, activation energy remains at ~120 $kJ.mol^{-1}$, and the oxidation rate is slightly higher than that of pure silicon carbide or silicon nitride ceramics. Riedel et al. [70] studied the relationship between the silica layer on the surface of SiCN and the solid-state reaction of the matrix and observed that the latter is inhibited by a very low diffusion coefficient of nitrogen in the SiO_2. An et al. [71] and Wang et al. [72] studied SiCN-based SiAlCN ceramics in which Al is doped to block the structure in an oxidised SiO_2 lattice, which later reduces the oxygen diffusion coefficient in the SiO_2 layer and enhances the oxidation resistance.

Mechanical Properties: Over the last five decades, PDCs have been widely used in various applications. To use the materials for a long time, understanding the deformation behaviour at elevated temperatures is essential to designing the material. Due to the unique precursor structure strongly governed by precursor chemistry, measuring the quantitative estimation of mechanical properties is challenging.

Fibers: Historically, the pursuit of the polymer pyrolysis route to advanced ceramics (PDC route) was motivated by the quest to develop ceramic fibers with exceptional thermo-mechanical properties [57,73]. Yajima et al. [73] showed that SiC fibers, resulting in tensile strength and Young's modulus of 6.2 and 440 GPa, respectively, could be produced. Nicalon fibers are produced from polycarbosilane by Nippon Carbon utilizing the Yajima technique. The first generation of Nicalon fibres is cured in the air at approximately 200 °C, thereby introducing 12 wt% oxygen into the system. Obtained fibers are described as Si(O)C fibres [74,75]. In search for enhancing the thermal stability of Nicalon-derived SiC fibres, modification of polycarbosilane with Ti is proposed and lead to the development of Si-Ti-C-O fibres with high-temperature resistance above 1200 °C, at room temperature tensile and elastic

modulus is 3 and 220 GPa [76]. By using the same concept later, Al- and Zr-modified SiC fibres developed, and produced SiAlCO fibers showing the 3 GPa tensile and 300 GPa elastic modulus and its mechanical properties can be retained up to 1900 °C [77]. Fibers of BN and SiBCN systems have also been synthesized from a boron-modified polysilazane, and it remains thermally stable up to 1500 °C [78].

Elasticity and Density: Elastic modulus (E) of prepared SiCN and SiOC falls in the range of ~80-150 GPa (SiCNs) [80,81] and ~57-113 GPa (SiOCs) [79,82,83]. These reported values are well below the elastic modulus of crystalline SiC and Si_3N_4. The amorphous structure of SiCN and SiOC systems density values are low in the range of 1.85-2.35 g/cm^3 [84,85]. As a general trend, as increasing the pyrolysis temperature, the elastic modulus and young modulus increase due to an increase in the network connectivity. An increase in density and elastic modulus is observed by incorporating C into the silica network via Si-C bonds in the sol-gel-derived SiOC glasses [86].

Poisson's Ratio: In literature, Poisson's ratio (υ) of PDCs has been reported in limited numbers, and the values are quite low. For SiCN systems, it ranges from 0.21 to 0.24 [80], whereas for SiOC glasses reported value is 0.11, this low value of Poisson's ratio of glasses and polycrystalline material is explained by low atomic packing density and high crosslinking degree of silicon oxycarbide glasses [83].

Hardness: Vickers hardness (HV) of SiOC is reported in the range of ~5 to 9 GPa [79,82,83]. Hardness increases by increasing (i) pyrolysis temperature, and (ii) amount of C inserted in the amorphous silica network [79,87]. A similar kind of behaviour is reported for the SiCN [88] and Si(O)C systems [89].

Fracture Toughness: Fracture toughness (K_{IC}) is measured for SiCN and SiOC; both processed by the liquid and by the powder route, and irrespective of the PDC system, reported values lay between ~0.56 and ~3 $MPa.m^{1/2}$ [82,89,91–94]. Higher K_{IC} values in the range of ~2-3$MPa.m^{1/2}$ are reported for SiCN and SiOC systems, which are obtained through the powder processing route [93]. PDCs obtained through the liquid route have much lower K_{IC} values, in the range of 0.56 and 1.3 $MPa.m^{1/2}$ [86].

Viscosity, Viscoelasticity and Creep: Si-based PDCs show remarkable creep resistance. For the SiOC system, creep is limited up to 1300 °C, and for Si-B-C-N PDC, it is 1500 °C. In amorphous PDCs, viscosity is the main property which makes them remarkably different from other known ceramics so far, typically, it is two to three orders of magnitude greater than

vitreous silica and stands as the highest recorded value for any glass at elevated temperatures. Data available on SiOC glasses were obtained through bending creep [95] and internal friction experiments [96] , while Si-C-N [97–99], Si-Al-O-C [100] and Si-B-C-N [98,99] were gathered through compressive creep experiments. SiOC glasses, viscoelastic behaviour was initially indicated by internal friction measurements [96] and subsequently confirmed by compressive stress measurements conducted between 1000-1200 °C [101].

1.6.2 Applications of PDCs

Due to PDCs' physical-chemical and functional properties as well as their ability to shape easily using casting, fibre drawing, coating, injection moulding, pressing and impregnation, PDCs have extensive attention for their wide applications. PDCs widely used in the application areas of monoliths, coatings, porous materials, membranes, micro components, ceramic fibers CMCs and complex shape materials. Only selected applications are described here.

Sensors: Sensors used in advanced systems which require detection and control. PDC sensors were developed because of semiconducting behaviour, especially the high-temperature-dependent conductivity feature of PDCs. Silicon or SiC-based sensors have been used at temperatures below 500 °C. A high-temperature pressure sensor is developed based on the piezoresistivity of SiAlOC, which requires strength to withstand high-temperature harsh environments with deteriorating properties [104]. An effective way to enhance the selectivity of gas sensors is by applying a thermally stable porous filter layer on the sensing material. Microporous PDCs (SiC, SiOC, SiCN, etc.) are suitable candidates as filter materials due to their chemical and thermal stability, and tunable porosity [105–107]. Kumar et al. reported a microporous amorphous SiOC filter layer coating the GaN Sensor layer and studied the gas sensing selectivity of H_2 with respect to CO [108].

Thermal Barrier Coatings/Environmental Barrier Coatings: In order to improve the material's stability in aggressive environments, thermal and environmental barrier coatings (TBCs/EBCs) have been developed using PDCs. Non-oxide and oxide ceramic coatings are well suited to improve the resistance to corrosion and oxidation of metals in chemically harsh environments. The main drawback of PDC is the shrinkage during the polymer pyrolysis; sometimes, it can be higher than 50% by volume. Due to volume shrinkage residual stress develops in the material and leads to the formation of defects, cracks or delamination of the coating. Volume shrinkage from polymer to ceramic transformation can be significantly reduced by using passive fillers like SiC, BN, ZrO_2 or active fillers like Nb, Ti, $TiSi_2$ [51,61].

PDC route has been applied to many studies to prevent the corrosion and oxidation of metallic and ceramic substrates at high temperatures [66,109–115]. PHPS (20 wt%) with passive glass fillers BN, Si_3N_4, ZrO_2 is coated on mild steel to enhance the oxidation resistance at 700 °C confirmed by conducting cyclic oxidation tests [109]. Novel-PDC coating is developed on medium carbon steel using polysiloxane and active/passive + glass frit at 800 °C, and it is identified that the coating is not delaminated, and no cracks were observed on the surface, this coating method can widely used to protect the carbon steels in boilers in waste-to energy plants [52].

PDC-based coatings: Corrosion prevention works based on PDC-based coatings in aqueous environments are described here. Bordia et al. [116] deposited $TiSi_2$-filled SiOC ceramic composite coating on 316 stainless steels by dip-coating of polyhydromethylsiloxane (PHMS) precursor, and the coated sample was pyrolyzed to 800 °C. Long-term corrosion-resistant testing was performed in H_2SO_4 by immersing the samples for 30 days; later, weight loss of the material is recorded, and they found that coated samples mass loss per unit area was reduced by 72% when compared to the base substrate. Fuping et al. [117] fabricated polycarbosilane-derived SiCN by dip-coating on iron (Fe) to check the effect of the curing process and pyrolysis effect on the microstructure. They found that at higher temperature at 600 °C, coating gives larger shrinkage compared to 400 °C due to the large molecule loss during pyrolysis. At 400 °C, the pyrolyzed sample showed improved corrosion resistance with lower amount of micro-cracks. Electrochemical testing of coated sample shows the improved corrosion resistance in 3.5 wt% NaCl solution. Perhydropolysilazane (PHPS)-derived SiO_2 coating on AISI 304 shows improved pitting and corrosion resistance in 0.6 M NaCl [118]. In this study, PHPS coatings was deposited at room temperature and at 600 °C, corrosion resistance of the samples were evaluated by OCP and potentiodynamic polarization methods. Coated samples pyrolyzed at 600 °C showed improved corrosion resistance compared to samples coated at room temperature. Perhydropolysilazane (PHPS) derived silica coating on Al 5086 substrate showed an improvement of about three orders of magnitude in corrosion resistance as studied by Renzo et al. [119]. Choi et al. [120] prepared a polysilazane-derived SiON coating on stainless steel and studied for weld metal corrosion protection using salt spray tests. Corrosion resistance of SiON coating was highly influenced by the coating thickness; coatings obtained at low withdrawal speeds of 1 mm/s and 3 mm/s showed a significant reduction in corrosion compared to uncoated substrates. Based on the literature survey, it is evident that very few studies on

electrochemical corrosion testing of PDC-based coatings in aqueous environments are reported and thus a detailed investigation is necessary.

1.7 Objectives of thesis work

The major objective of the thesis is enhancement of corrosion resistance of SS304 by depositing ceramic layers using polymer-derived route. The research work of this thesis is focused on:

(i) Synthesis and characterization of ceramics using polymer-pyrolysis route,

(ii) Optimization of coating parameters,

(iii) Enhancing corrosion protection behavior of amorphous SiOC- and SiCN-coated SS304.

Chapter 2. Experimental methods

The current chapter discusses the experimental methods and equipment used for the synthesis and characterization of polymer-derived ceramics (PDCs) used in this work. Pyrolysis parameters to synthesize PDCs from polymeric precursors and the deposition method to coat polymer-derived ceramic layers on the substrates are described. At the end, various equipment and parameters applied to characterize the structure of synthesized powdered ceramics and ceramic coated substrates as well as electrochemical characterization techniques to evaluate the corrosion protection performance of ceramic coated substrates are discussed briefly.

2.1 Pyrolysis process and parameters to obtain polymer-derived ceramics

In this work, pyrolysis process (a heat treatment process under inert environment to cross-link and decompose the precursors at high temperatures) of two polymeric precursors was done to obtain ceramics for structural characterization. Pyrolysis temperature was determined from the thermal analysis data of precursors described in sections 3.1.3 and 3.2.3. Parameters used to pyrolyze the precursors are mentioned below:

Silicon-oxycarbide (SiOC) ceramic derived from polysiloxane: In order to prepare SiOC ceramic powder, commercially available viny-functionalized polysiloxane precursor (XP RV200, Evonik, Hanse GmbH) was taken and pyrolyzed at 800 °C under flowing argon atmosphere. Handling and transferring of samples were performed under the glove box. The precursor was kept in a quartz boat and transferred to a high-temperature furnace. Precursor is pyrolyzed from room temperature to 250 °C at a heating rate of 100 °C/h, hold for 1 h at 250 °C to promote crosslinking followed by heating to 800 °C, hold for 1 h at 800 °C and then furnace cooled to room temperature.

Silicon-carbonitride (SiCN) ceramic derived from polysilazane: To prepare SiCN ceramic powder, commercially available polysilazane (Durazane 1800, Merck) precursor was taken and pyrolyzed at 800°C under flowing argon atmosphere. Polymeric precursor was kept in a quartz boat and transferred to a furnace followed by thermolysis from room temperature to 250°C at a heating rate of 100 °C/h, hold for 1 h at this temperature to promote crosslinking and further heating to 800°C, hold for 1 h at 800 °C and furnace cooled to room temperature.

2.2 Base substrate

In this work, stainless steel 304 (SS304) was selected as the base substrate, and its chemical composition is listed in Table 2.1. SS304 samples with dimensions (5 cm × 2.5 cm × 0.3 cm)

were polished up to 1000 grit emery paper followed by ultrasonication cleaning and dried in an oven at 150 °C to remove any external contamination and moisture.

Table 2.1 Chemical Composition of SS304 measured using the SPECTROLAB instrument, Model-12.

Element	C	Si	Mn	P	S	Cr	Ni	Fe
wt%	0.039	0.387	0.994	0.032	0.004	17.93	7.93	72.652

2.3 Deposition of ceramic layers on SS304

Dip-coating method was used for the deposition of polymeric precursors on substrates and polymer coated substrates were pyrolyzed to obtain ceramic coated SS304.

To coat the substrate, polymeric precursor was diluted with anhydrous toluene (50 % by volume) and was stirred using a magnetic stirrer inside a glove box to get homogenized solution. The prepared preceramic solution was dip-coated on SS304 by immersing the substrate in the solution for 3-4 min and withdrawn at a speed of 40 mm/min followed by pyrolysis under an argon environment by initially heating at 250 °C for 1 h to promote crosslinking of coated precursor and subsequently pyrolyzed at 800 °C for 1 h. Before performing the dip-coating on SS304, the other side of the substrate was masked using scotch-tape. For multiple coatings of ceramic layers, pyrolysis of polymer coated substrate was done before depositing the successive layers. Schematic of dip-coating process and set-up used in this study are shown in Figure 2.1.

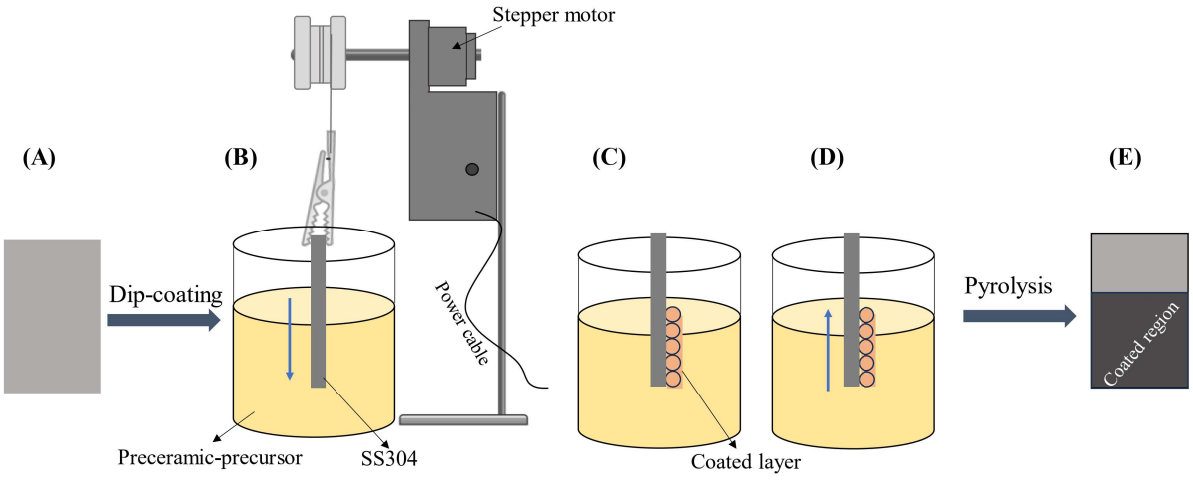

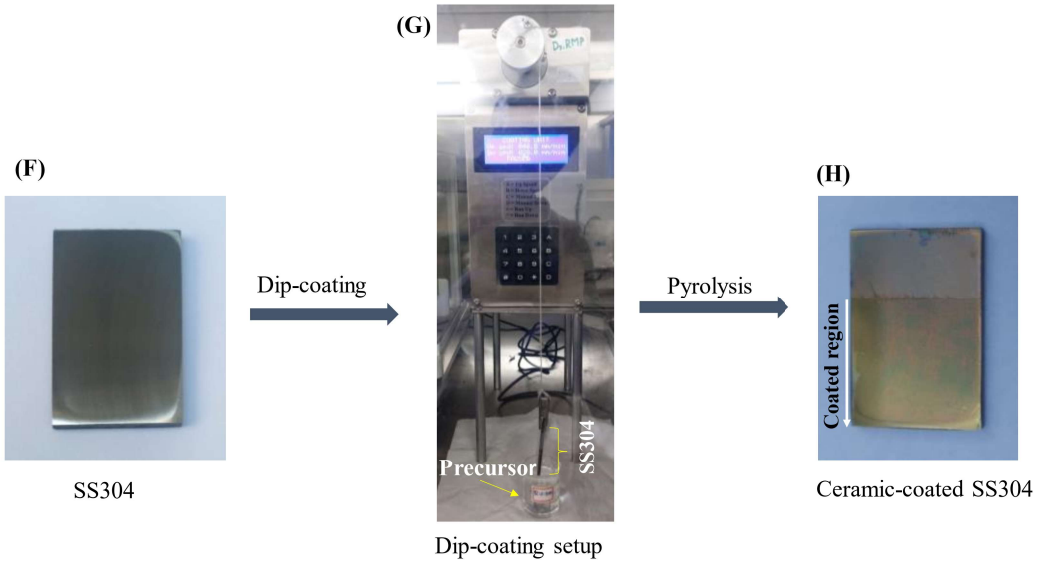

Figure 2.1 Schematic of Dip-coating process: (A) schematic of the substrate (SS304). Sequences of steps involved in dip-coating process: (B) substrate is dipped in the polymeric solution, (C) immersing the substrate in the solution for a few minutes, (D) withdrawing of immersed substrate, and (E) pyrolyzing the precursor coated sample. Digital images of: (F) uncoated SS304, (G) Dip-coating setup, and (H) ceramic-coated SS304.

2.4 Characterization techniques

2.4.1 Nuclear magnetic resonance (NMR) spectroscopy

^{1}H, ^{13}C and ^{29}Si liquid-state NMR spectra of as-received polymeric precursors were recorded on a JNM-ECS NMR spectrometer by operating at a frequency of 400 MHz using $CDCl_3$ (deuterated chloroform) as a solvent. Tetramethyl silane (TMS) was used as the internal reference material.

2.4.2 Attenuated total reflectance-Fourier transform infrared (ATR–FTIR) spectroscopy

ATR–FTIR spectroscopy of polymeric precursors (vinyl-functionalized polysiloxane and polysilazane) and synthesized ceramics (SiOC and SiCN) were measured in the range of 4000–600 cm^{-1} with a spectral resolution of 1 cm^{-1} using the Smart iTX single-reflection ATR assembly and Nicolet iS50 FTIR spectrometer (Thermo Scientific) under nitrogen environment.

2.4.3 X-ray Diffraction (XRD)

X-ray powder diffraction (XRD) measurements of the synthesized ceramic and ceramic coated substrates were recorded using PANalytical X′Pert Pro diffractometer with flat sample stage geometry using CuKα radiation in the reflection scanning mode in the 2θ range of 20–90° with

a scanning speed of 1° min^{-1}. Peak positions corresponding to structures were identified using X'pert High Score Plus software.

2.4.4 Thermal gravimetric analysis (TGA)

To find the ceramic yield of polymeric precursors and required pyrolysis temperature for coating of ceramics on substrates thermal gravimetric analysis measurements of precursors were done. TGA of polymeric precursors were performed using SDT 650 simultaneous Thermal Analyzer (TA Instruments). Samples were heated from room temperature to 900 °C at a heating rate of 5 °C/min under argon environment at a flow rate of 25 ml/min.

2.4.5 Optical Microscopy

The images of the surface of base substrate (SS304) and ceramic coated substrates were recorded using an optical microscope (DM4 Microscope, Leica).

2.4.6 Field emission scanning electron microscopy (FESEM)

The surface morphologies of the uncoated and ceramic coated were examined using JEOL JSM-7610FPlus with an acceleration voltage of 5-15 kV. The cross-sectional thickness of the coated ceramic layers on SS304 and energy dispersive spectroscopy (EDS) elemental mapping of the coated surfaces were measured. Before recording the image, samples were sputtered with gold layers to avoid the charging effect.

2.4.7 Raman spectroscopy

Raman spectra of powdered ceramics and ceramic coated substrates were recorded on a confocal micro-Raman spectrometer (LabRAM HR Evolution, Horiba France SAS) with excitation laser wavelength of 532 nm with 5% of maximum laser power at laser head (100 mW) from 300 to 3000 cm^{-1}. Data acquisition and analysis of Raman spectra were performed using labSpec 6 software.

2.5 Electrochemical characterization

To evaluate the corrosion resistance performance of base substrate and coatings, electrochemical methods like Open Circuit Potential (OCP), Potentiodynamic Polarization, and Electrochemical Impedance Spectroscopy (EIS) performed. All the electrochemical testing were conducted in 0.6 M NaCl (3.5 wt% NaCl) solution using a biological flat cell (shown in Figure 2.2 A) equipped with three electrodes – sample as working electrodes (WE), Ag/AgCl as a reference electrode (RE) and platinum mesh as a counter electrode (CE). Working electrodes with a 1 cm^2 area were used for corrosion testing. Schematic of the electrochemical setup connection is shown in Figure 2.2 B; a constant potential is applied between WE and CE,

and current is measured between the WE and CE. All electrochemical measurements were performed using potentiostat (Metrohm Autolab) as shown in Figure 2.2 C.

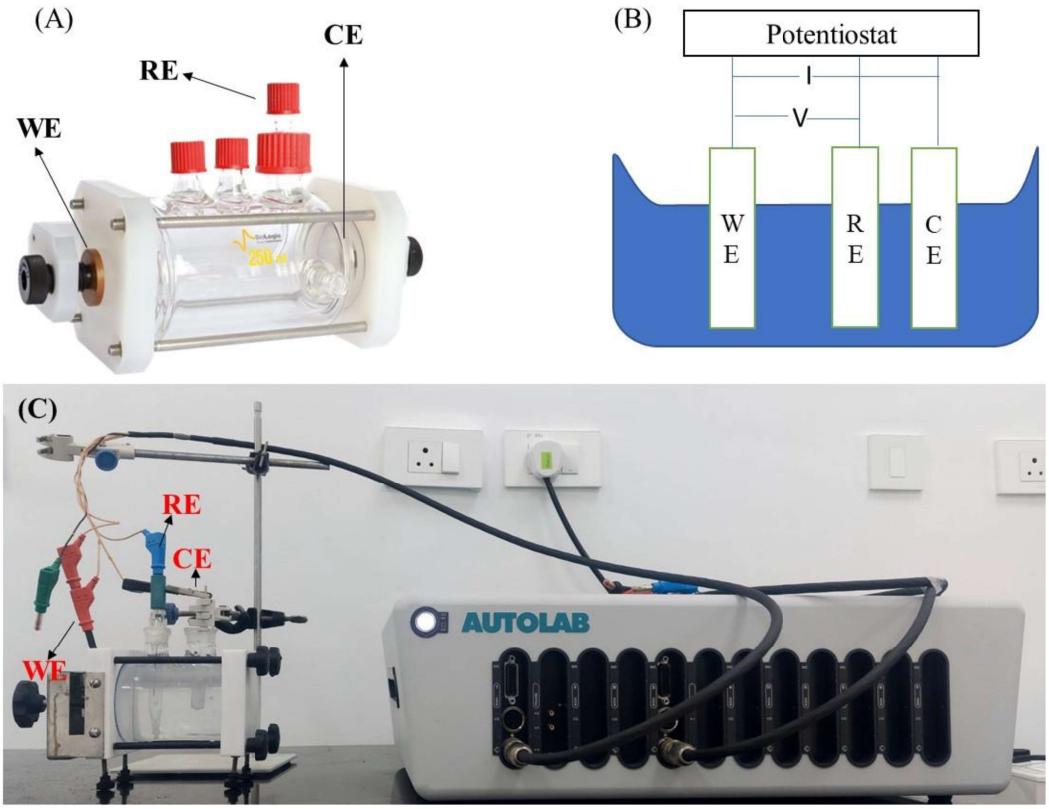

Figure 2.2 (A) Flat-cell, (B) schematic of electrochemical cell connections to potentiostat, and (C) Electrochemical workstation (Metrohm Auto lab).

2.5.1 Open Circuit Potential (OCP)

After immersing the sample in 0.6 M NaCl electrolyte, OCP was recorded for 1 h to attain the stable potential value.

2.5.2 Potentiodynamic Polarization

Potentiodynamic polarization measurements were performed using a potentiostat within the potential range of -500 mV (vs Ag/AgCl in the cathodic direction) and +500 mV (vs Ag/AgCl in the anodic direction) with respect to OCP value at a scan rate of 0.167 mV/sec according to ASTM G61-86 (2009) to measure the corresponding current change [18]. After attaining stable OCP values polarization measurements were performed.

2.5.3 Electrochemical Impedance Spectroscopy (EIS)

EIS measurements were carried out using the same potentiostat as that was used for potentiodynamic polarization measurements. EIS measurements were performed using ac perturbation signal of 10 mV over a frequency range of 0.1 Hz to 100000 Hz.

2.6 Immersion Test

The long-term corrosion behaviour of the samples (SS304 and ceramic coated SS304) were studied by immersing the samples in 0.6 M NaCl solution for different intervals and measuring the weight loss at each interval according to the ASTM G31-72 (2004) standard [121]. In this method, square type 1 cm^2 samples were hanged in a 100 mL, 0.6 M NaCl solution. The initial weight of the uncoated samples were measured using a precision balance and then samples were immersed in the solution for distinct time intervals (24 h, 72 h, 120 h and 168 h). After completion of immersion duration, samples were washed with DI water/dried and weight were measured. Data obtained were used to calculate the mean corrosion rate using the following formula:

$$\text{Mean corrosion rate} = \frac{(K \times W)}{(A \times T \times D)}$$

where K is unit constant 8.76×10^4 to measure the corrosion rate in mm/yr, as per ASTM G31-72 (2004), W is the mass loss in grams, A is the area in cm^2, T is immersion time in hours, D is the density in g/cm^3.

2.7 Adhesion Test (X-cut Tape Test)

Adhesive tape tests were done to verify the adherence of ceramic coating to the base substrate using ASTM D3359 method. A sharp razor blade was used to make an X-cut through the samples. Wide transparent tape was pasted on the surface of the X-cut, and after 90 seconds the tape was peeled from the coated surface and X-cut surface images on the tape were captured to assess the adherence.

Chapter 3. Synthesis and characterization of polymer-derived ceramics and optimization of ceramic coating parameters on SS304 substrate

This chapter describes synthesis and characterization of polymer-derived ceramics (PDCs) obtained from polymeric precursors and coating the ceramic layers on SS304 substrate to enhance corrosion protection. Silicon-oxycarbide (SiOC) and silicon carbonitride (SiCN) were synthesized by pyrolyzing commercially available vinyl-functionalized polysiloxane (XP RV 200) and polysilazane (Durazane 1800) under argon environment. Pyrolysis process and parameter to synthesize PDCs using various precursors used in this thesis work are already described in chapter 2 (section 2.1). Structure of the polymeric precursors were investigated using liquid state NMR and ATR-FTIR spectroscopy; Thermal analysis to determine polymer-to-ceramic transition temperature and structural characterizations (XRD, Raman, SEM) of the synthesized ceramics were performed. In the following sections, the synthesis and characterization of each synthesized ceramics are discussed.

3.1 Synthesis of silicon-oxycarbide (SiOC) derived from vinyl-functionalized polysiloxane

The molecular structure of as-received vinyl-functionalized polysiloxane is shown in Figure 3.1 (as provided by manufacturer, Evonik Industries AG, Germany; vinyl content in the polymer is ~2.3 mmol/g, density of 1.0 g/cm^3), and the structure was verified using liquid state NMR and ATR-FTIR spectroscopy, which are explained in sections 3.1.1 and 3.1.2.

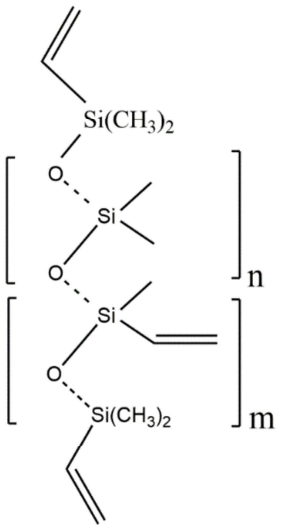

Figure 3.1 Molecular structure of vinyl-functionalized polysiloxane, XP RV 200.

3.1.1. Liquid-state NMR characterization

^{1}H NMR: The proton NMR spectrum of vinyl-functionalized polysiloxane is presented in Figure 3.2 A-B. Two resonance peaks are observed from -0.01 ppm to 0.24 ppm corresponding to methyl groups, Si-O-$(CH_3)_2$, in the polymer structure which is in agreement with the reference [122]. Peak shift ranging from 5.6 ppm to 6.1 ppm indicates vinyl-group bonding, $(CH_2{=}CH)$Si-O, in the polymeric structure.

^{13}C NMR: In the carbon ^{13}C NMR (Figure 3.2 C), resonance peaks are identified at 126 ppm,128 ppm and 133 ppm, which are in good agreement with the vinyl groups present in the polymer structure [122].

^{29}Si NMR: Figure 3.2 D shows the silicon (^{29}Si) NMR of vinyl-functionalized polysiloxane. It shows two resonance peaks; one in the range from -20 ppm to -21.5 ppm corresponds to methyl silicon bonding in the polymer O-Si$(CH_3)_2$-O and the other resonance peak at around -35 ppm is attributed to vinyl bonded to silicon group which is $(CH_3)(CH_2{=}CH)$-Si-O [122].

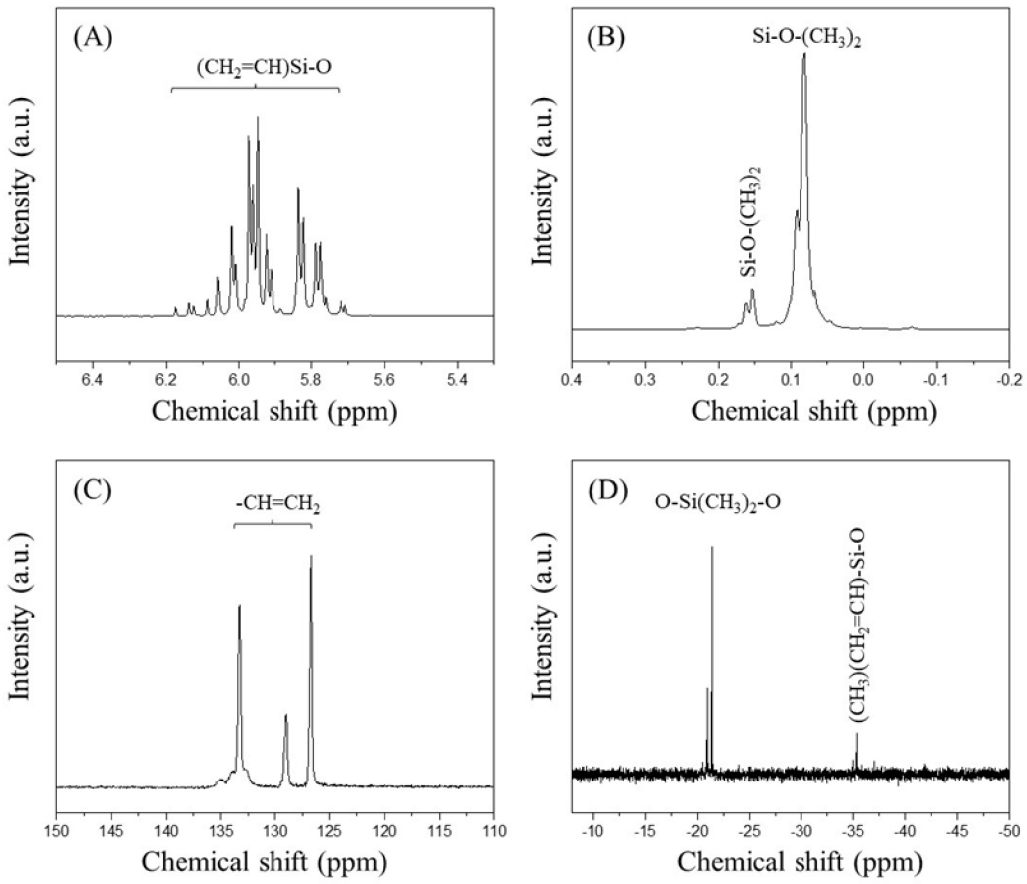

Figure 3.2 Liquid-state NMR spectrum of vinyl-functionalize polysiloxane using $CDCl_3$ as solvent: (A-B) ^{1}H, (C) ^{13}C, and (D) ^{29}Si.

3.1.2 ATR-FTIR characterization

ATR-FTIR spectra of polymeric precursor and SiOC ceramic powder synthesized at 800 °C are presented in Figure 3.3. The bands at 788, 1007, 1257, 1407, 1597, 2962 and 3054 cm^{-1} have been assigned to Si-CH_3, Si-O-Si, Si-CH_3, C-H, CH=CH_2, C-H and CH=CH_2, respectively [123,124]. Very low intensity bands at 1597 and 3054 cm^{-1} indicate the presence of very low amount of vinyl groups in the polymer, which is in agreement with the data provided by the supplier and the absence of these bands in the synthesized SiOC ceramic (obtained by pyrolyzing the precursor at 800 °C) confirms cross-linking reaction of vinyl groups followed by pyrolysis process leading to ceramic formation. Synthesized SiOC shows bands at 797 cm^{-1}, 1009 cm^{-1}, and 1262 cm^{-1} which corresponds to bands of Si-C, Si-O-Si, and Si-C, respectively [125]. ATR-FTIR analysis confirms the transformation of vinyl-functionalized polysiloxane precursor into SiOC ceramic after pyrolysis.

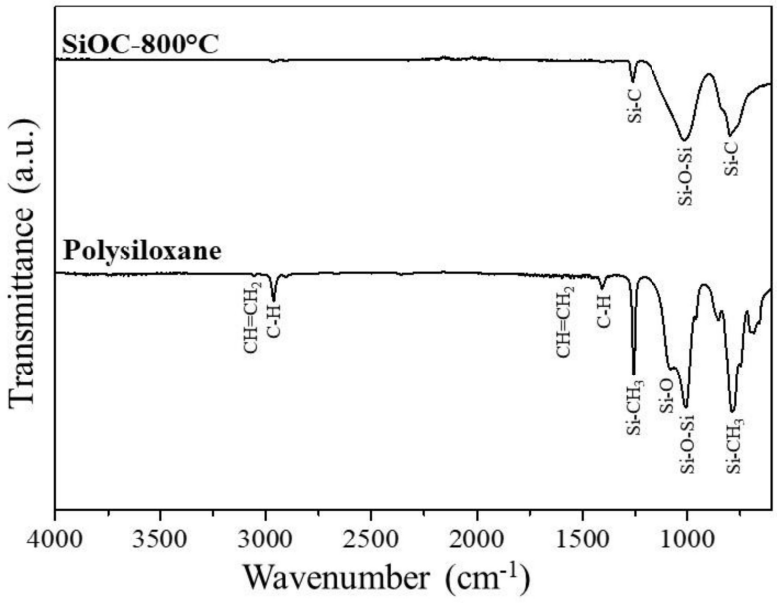

Figure 3.3 ATR-FTIR spectrum of vinyl-functionalized polysiloxane (XP RV 200) and SiOC ceramic obtained after pyrolysis at 800 °C.

3.1.3 TGA characterization: Polymer-to-ceramic transformation

Thermal Gravimetric Anlaysis (TGA) of polysiloxane was performed to determine polymer-to-ceramic transformation temperature and required pyrolysis temperature for coating of ceramic layers on stainless steel (S304) substrates. With the increase in temperature under argon, mass change of the polymer was recorded. Figure 3.4 A shows that above 750 °C mass change is constant with a ceramic yield of about ~33% by mass. TGA with mass spectrometry

was used to identify the gases released during polymer-to-ceramic transformation of vinyl-functionalized polysiloxane, Figure 3.4 B. Mass loss occurs in several steps by the release of oligomers (vinyl component, m/z = 28) in the temperature range of 150-400 °C and due to the release of methane (m/z = 16) and hydrogen (m/z = 2) components during the ceramization process in the range of 500-650 °C [108] . Negligible mass change is observed above 750 °C which indicates the completion of ceramization process.

Based on the TGA data (Figure 3.4), 800 °C was selected as the temperature for the synthesis of SiOC ceramic powder from polysiloxane as well as for depositing ceramic layers on SS304 and further structural characterizations were performed.

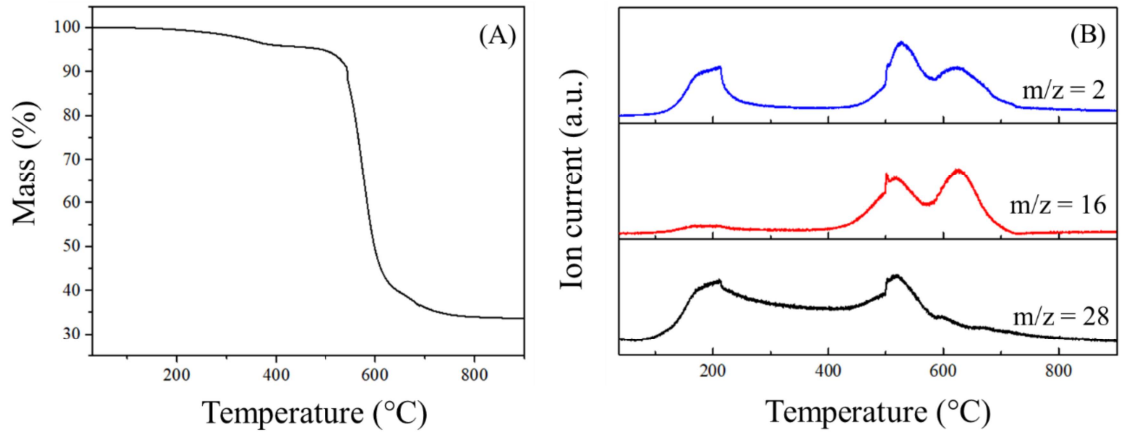

Figure 3.4 (A) Thermal Gravimetric Analysis (TGA), and (B) Mass spectra of vinyl-functionalized polysiloxane heated up to 900 °C (at heating rate of 5 °C min^{-1} under flowing argon).

3.1.4 XRD characterization

XRD pattern of the synthesized SiOC powder was found to be amorphous as confirmed by featureless broad x-ray diffraction pattern (Figure. 3.5), which is in agreement with other reported works on polymer-derived ceramics synthesized at lower pyrolysis temperatures (< 1000 °C).

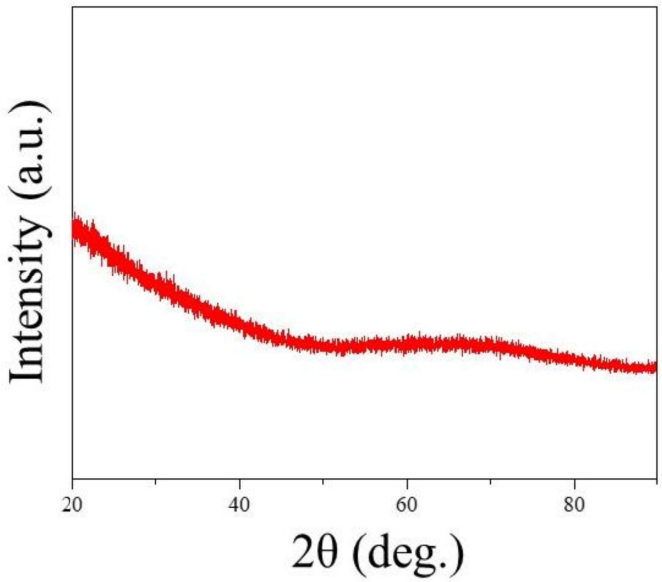

Figure 3.5 X-ray powder diffraction pattern of vinyl functionalized polysiloxane-derived SiOC ceramic obtained by pyrolyzing under argon at 800 °C.

3.2 Synthesis of silicon-carbonitride (SiCN) derived from polysilazane

SiCN ceramic was synthesized by pyrolysis of commercially available polysilanze (Durazane 1800). Molecular structure of as received precursor has been studied using liquid-state NMR spectroscopy and ATR-FTIR spectroscopy.

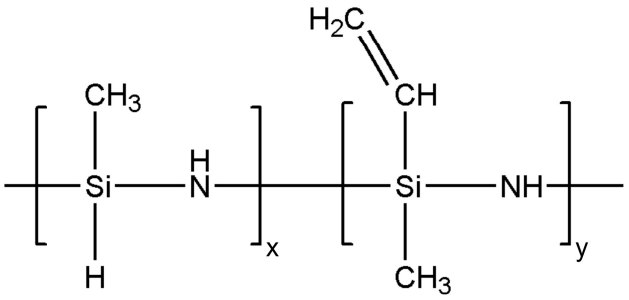

Figure 3.6 Molecular structure of polysilazane (Durazane 1800).

3.2.1 Liquid-state NMR characterization

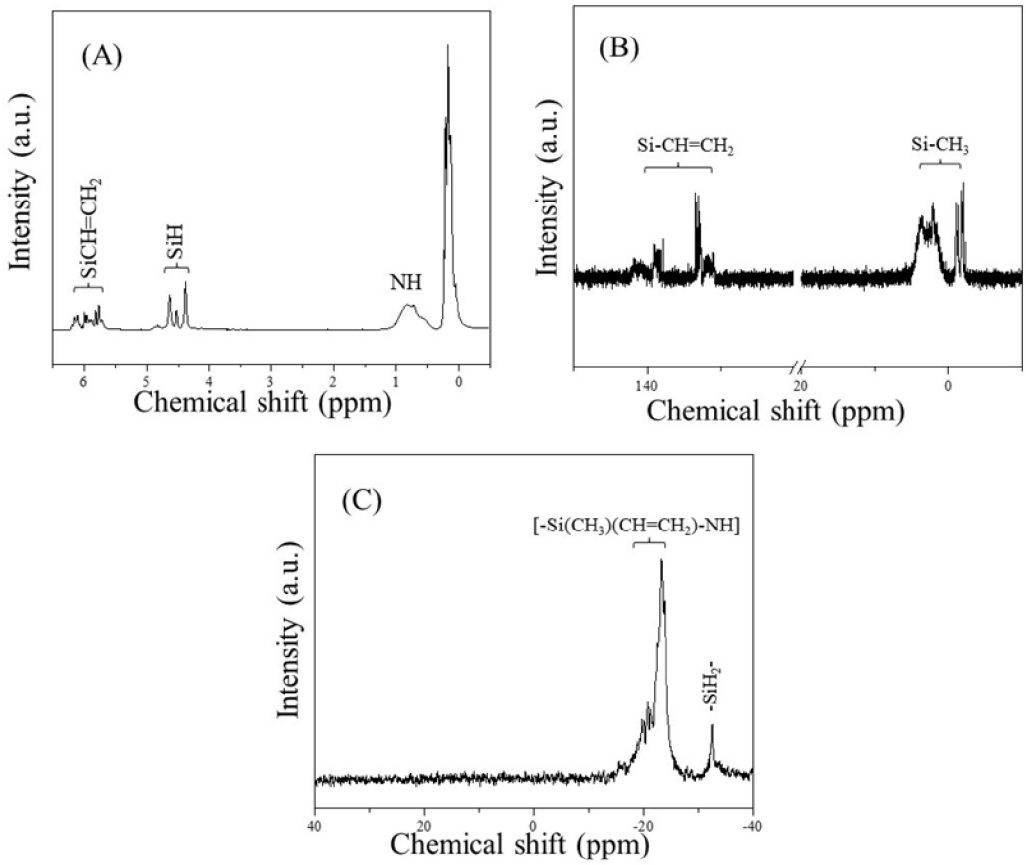

Figure 3.7 Liquid-state NMR spectrum of polysilazane using $CDCl_3$ as solvent: (A) ^{1}H spectrum, (B) ^{13}C spectrum, and (C) ^{29}Si spectrum.

^{1}H, ^{13}C, and ^{29}Si liquid-state NMR spectra of polysilazane (Durazane 1800) are shown in Figure 3.7 A-C.

^{1}H NMR: ^{1}H NMR spectrum of polysilazane is shown in Figure 3.7 A. SiH protons appear as multiplets between 4.1 and 4.9 ppm. Centered at 0 ppm, $SiCH_3$ protons were found as a broad resonance. Multiplets between 5.6 and 6.2 ppm are attributed to $SiCH=CH_2$, [126–128]. NH resonance can be seen as a broad signal at around 0.76 ppm [129].

^{13}C NMR: In ^{13}C NMR spectrum (Figure 3.7 B), signals related to methyl and vinyl groups attached to silicon are observed. Broad signal in the range from -2.4 to 5 ppm is assigned to $Si-CH_3$ and chemical shifts of 131-142 ppm corresponds to $Si-CH=CH_2$ [128].

^{29}Si NMR: In Figure 3.7 C, broad resonance peaks observed in the range from -16 to -27 ppm are assigned to [-Si(CH_3)($CH=CH_2$)-NH] [130], and minor signal at -32.5 ppm confirms the presence of trace amount of -SiH_2- functionality [131] .

3.2.2 ATR-FTIR characterization

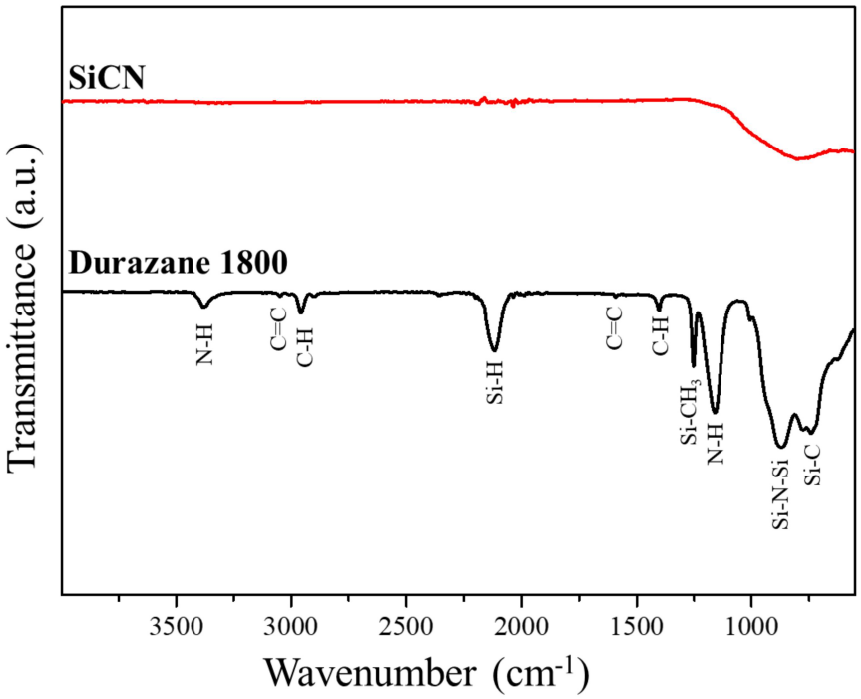

Figure 3.8 ATR-FTIR spectra of commercial polysilazane precursor (Durazane 1800) and SiCN ceramic powder synthesized by pyrolysis at 800 °C.

Figure 3.8 shows ATR-FTIR spectra of polymeric precursor polysilazane (Durazane 1800) and SiCN ceramic obtained by pyrolyzing the precursor at 800 °C. Absorption bands at 751 cm^{-1} (Si-C), 870 cm^{-1} (Si-N-Si), 1159 cm^{-1} (N-H), 1253 cm^{-1} (Si-CH3), 1590 cm^{-1} (C=C), 2118 cm^{-1} (Si-H), 2958 cm^{-1} (C-H), and 3382 cm^{-1} (N-H) are matched with the existing literature [128,131–134]. SiCN ceramic derived from polysilzane shows absence of absorption bands corresponding to Si-H and C-H; a broad band appeared in the range of 740-1100 cm^{-1} is assigned to Si-C and Si-N-Si [132,133].

3.2.3 TGA characterization: Polymer-to-ceramic transformation

TGA data of polysilazane shows mass loss occured in three stages, Figure 3.9 A. Simultaneous recorded mass spectra show gases evolved during heat treatment of the polymer as shown in Figure 3.9 B. During crosslinking reaction in the temperature range of 150 °C to 300 °C, mass loss occurred due to the release of hydrogen (m/z = 2), methane (m/z = 16), and vinyl fragments

(C_2, m/z = 28). In the next step up to 500 °C, ammonia (m/z = 17), methane (m/z = 16), and vinyl fragments (m/z = 28) were released. During the ceramization stage (500-750 °C), mass loss occurred mainly due to the release of ammonia and methane. Above 750 °C, there is almost no mass change, indicating the polymer-to-ceramic transformation with a ceramic yield of ~71% by mass.

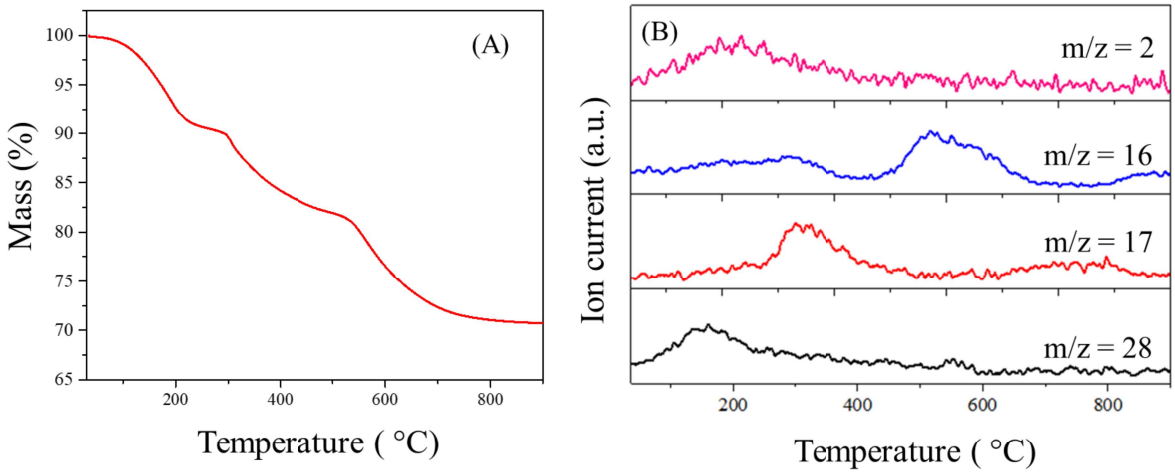

Figure 3.9 (A) Thermal Gravimetric Analysis (TGA) cruve, and (B) Mass spectra of polysilazane (Durazane 1800) heated up to 900 °C (at heating rate of 5 °C min^{-1} under flowing argon).

3.2.4 XRD characterization

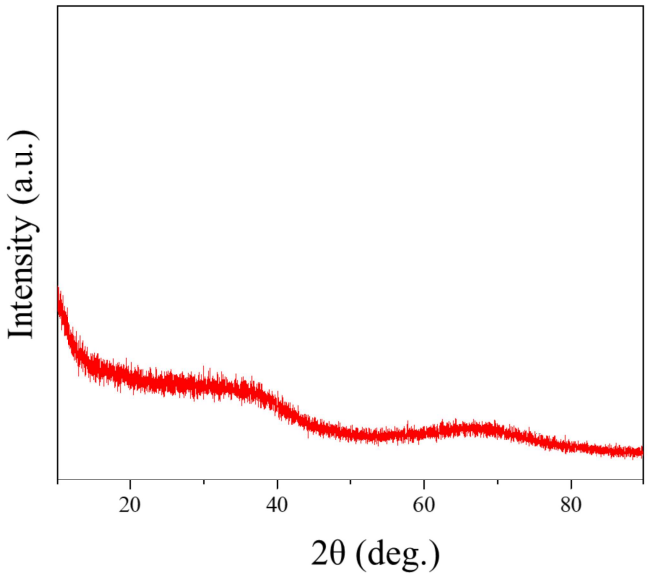

Figure 3.10 X-ray powder diffraction pattern of polysilazane-derived SiCN ceramics obtained by pyrolyzing under argon at 800 °C.

SiCN ceramic powder synthesized at 900 °C was found to be amorphous in nature with a featureless broad x-ray diffraction pattern, as shown in Figure 3.10; similar findings are observed for polymer-derived ceramics obtained after pyrolyzing at the temperatures (<1000 °C) [135–137].

3.3 Optimization of ceramic coating parameters on SS304 substrate

After synthesis and structural characterization of ceramics from polymeric precursors, optimization of process parameters for the coating of ceramic layers on SS304 substrate from respective precursors are described in the following sections.

3.3.1 SiOC ceramic coating on SS304

SS304 samples (were dip-coated with vinyl-functionalized polysiloxane solutions ─ diluted to 40 vol%, 50 vol%, and 60 vol% (in anhydrous toluene) ─ followed by pyrolysis at 800 °C using coating parameters and pyrolysis conditions as already described in section 2.3. Normally after one-fold coating process very thin and non-uniform ceramic layer is observed. Therefore, after deposition of one-fold SiOC ceramic layer on SS304, coating/pyrolysis process was repeated to get two-fold SiOC coated SS304 sample using all three diluted polysiloxane solutions. Surface of SiOC-coated SS304 samples were examined using optical microscopy and corresponding micrographs are shown in Figure 3.11.

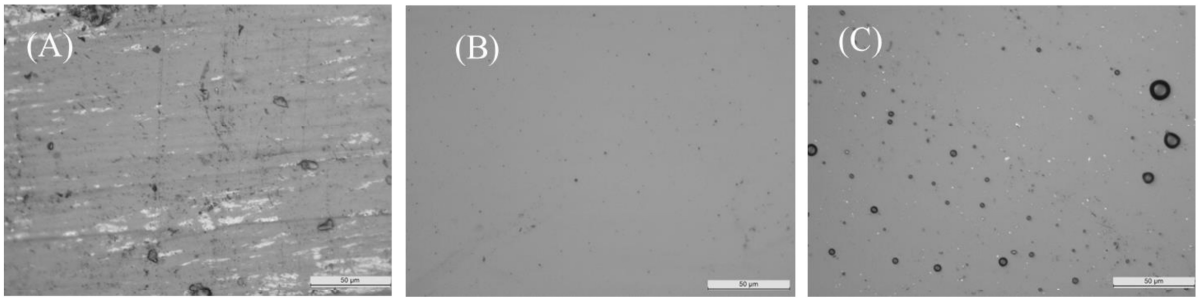

Figure 3.11 Optical micrographs of two-fold SiOC-coated SS304 deposited using (A) 40 vol% vinyl-functionalized polysiloxane, (B) 50 vol% vinyl-functionalized polysiloxane solution, (C) 60 vol% vinyl-functionalized polysiloxane solution.

After two-fold SiOC-coating on SS304 using 40 vol% polysiloxane solution it was found that coating was non-uniform as some regions of the substrate surface were not coated properly and some defects were also observed (Figure 3.11 A), whereas for two-fold SiOC-coated SS304 sample prepared using 50 vol% polysiloxane solution coating was found to be uniform and crack free. After depositing two-fold SiOC-coating on SS304 using 60 vol% polysiloxane solution, bubble-like defects were found on the surface as shown in Figure 3.11

C. During polymer-to-ceramic transformation while pyrolyzing a polymeric precursor, mass loss occurs due to the release of volatile species. When 60 vol% polymeric solution is coated on the SS304 surface, it leads to an increase in the thickness of the polymer coating; due to this, decomposed gases during pyrolysis will not escape easily and form bubbles within the coating. From the optical micrographs of the coated samples, it is identified that 50 vol% precursor solution is suitable for the deposition of SiOC coating on SS304. Further optimizations were carried out by comparing two-fold and three-fold SiOC coatings on SS304 using 50 vol% vinyl-functionalized polysiloxane.

Digital images and optical micrographs of two-fold and three-fold SiOC-coated SS304 samples are shown in Figure 3.12 and Figure 3.13. For two-fold SiOC-coated SS304 sample, coating was found to be uniform and crack free (Figure 3.13 A) whereas for three-fold SiOC-coated SS304 cracks were observed on the coated surface which could be due to formation of thick ceramic layer on the surface as shown in Figure 3.13 B.

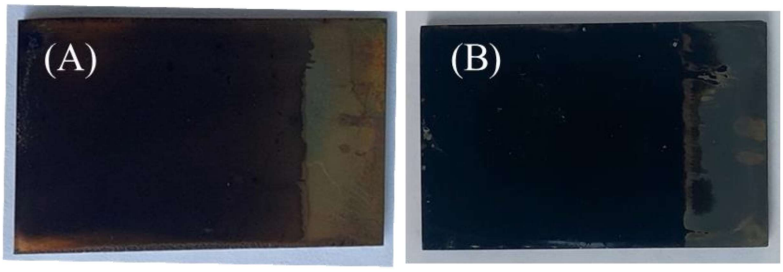

Figure 3.12 Digital images of SiOC ceramic coated samples prepared using 50 vol% polysiloxane solution: (A) two-fold SiOC-coated SS304, and (B) three-fold SiOC-coated SS304.

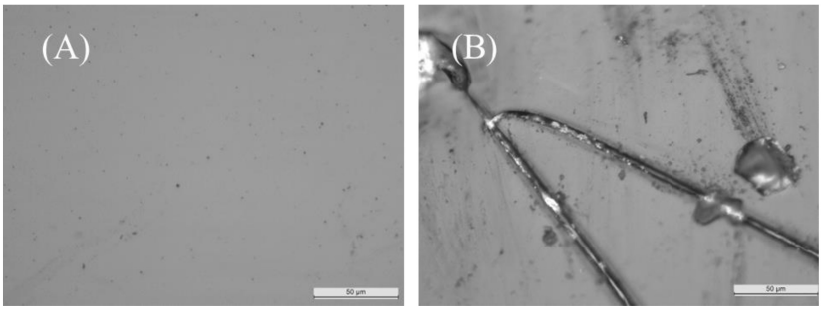

Figure 3.13 Optical micrographs of the surface of ceramic coated samples prepared using 50 vol% polysiloxane solution: (A) two-fold SiOC-coated SS304, and (B) three-fold SiOC-coated SS304.

While increasing the number of SiOC-coated layers from two-fold to three-fold, thermal mismatch between polymer-derived ceramic coated layer and SS304 substrate leads to crack

formation. Moreover, during the polymer-to-ceramic transformation, stresses develop in the PDC network due to gas evolution and considerable volume shrinkage (30-60 %), leading to cracking PDC coatings.

3.3.2 SiCN ceramic coating on SS304

For optimization of SiCN coating parameters on SS304 (with sample dimensions 5 cm × 2.5 cm × 0.3 cm), commercial polysilazane precursor (Durazane 1800) was diluted with anhydrous toluene (50 % by volume) and dip-coating process was carried out followed by pyrolysis at 800 °C to obtain one-fold, two-fold and three-fold SiCN coated SS304 as discussed in sections 2.3 and 3.2. Figure 3.14 and Figure 3.15 shows digital images and optical images, respectively, of SiCN-coated SS304 samples. One-fold coated sample was found be very thin (Figure 3.14 A and 3.15 A), whereas two-fold SiCN-coated SS304 showed non-uniform surface and some defects (bubble formation) in the coated layer, as shown in Figure 3.14 B and 3.15 B. For three-fold SiCN coated SS304 sample, coating was found to be uniform and crack-free, Figure 3.14 C and 3.15 C.

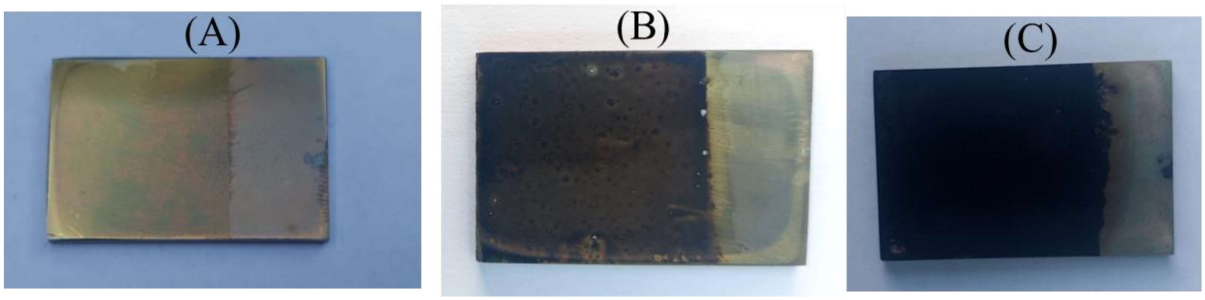

Figure 3.14 Digital images of SiCN-coated SS304 sample prepared using 50 vol% polysilazane solution: (A) one-fold SiCN-coated SS304, (B) two-fold SiCN-coated SS304, and (C) three-fold SiCN-coated SS304.

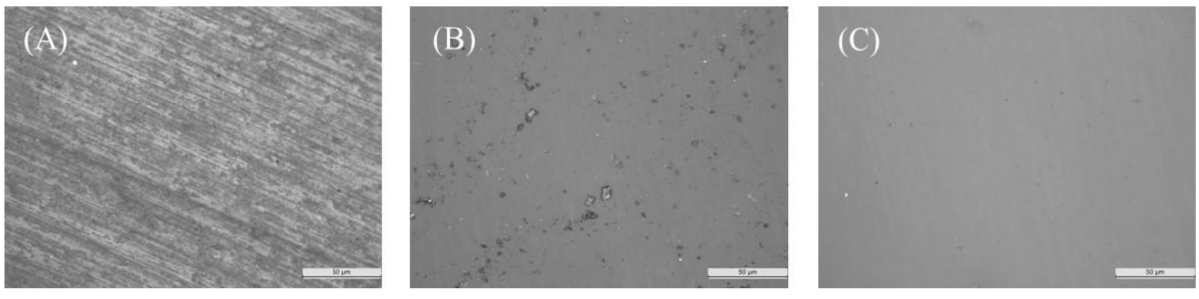

Figure 3.15 Optical micrographs of the surface of ceramic coated samples prepared using 50 vol% polysilazane solution: (A) one-fold SiCN-coated SS304, (B) two-fold SiCN-coated SS304, and (C) three-fold SiCN-coated SS304.

Based on the abovementioned optimization process carried out using different concentration of polymeric solutions and deposition of multi-fold ceramic coated layers following was concluded and considered for further corrosion protection performance evaluation which are described in chapter 4 and chapter 5:

(1) Two-fold SiOC-coated SS304 sample prepared using 50 vol% vinyl-functionalized polysiloxane solution,
(2) Three-fold SiCN-coated SS304 sample prepared using 50 vol% polysilazane solution.

Chapter 4. Corrosion protection performance of polymer-derived SiOC-coated SS304

In this chapter, structural characterization and electrochemical characterization of SiOC-coated SS304 is discussed. SS304 substrate was dip-coated with vinyl-functionalized polysiloxane (50% by volume) followed by pyrolysis at 800 °C to obtained SiOC-coated SS304. Structural characterization of base substrate SS304 and SiOC-coated SS304 was performed using SEM, XRD, and Raman spectroscopy. Electrochemical characterization of the samples were performed in 0.6 M NaCl solution.

4.1 Structural characterization of uncoated SS304 and SiOC-coated SS304

4.1.1 Scanning electron microscopy (SEM)

Polished SS304 was two-fold SiOC coated by dip-coating of polysiloxane solution followed by pyrolysis process 800 °C, as described in experimental procedures (chapter 2, sections 2.1 and 2.3) and surface morphology of the coated layer was checked using FESEM. SiOC ceramic coated layer was found to be is crack-free with a thickness of ~1 µm as shown in Figure 4.1 B and C. The elemental composition of the coating was found to be 40.2 wt% Si, 34.4 wt% O, and 25.4 wt% C.

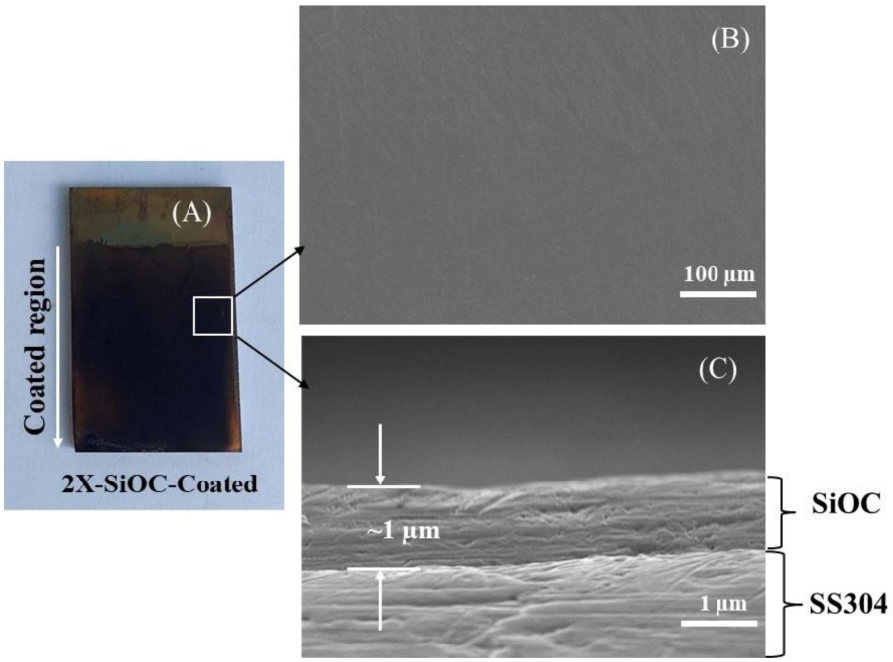

Figure 4.1 (A) Digital image of the two-fold SiOC-coated SS304. Field emission scanning electron microscopy (FESEM) images of: (B) uniform and crack-free surface of SiOC coated layer, and (C) cross-sectional view of SiOC-coated SS304.

4.1.2 X-ray diffraction (XRD)

X-ray diffraction measurements of base substrate (SS304), SiOC powder synthesized at 800 °C, and SiOC-coated SS304 were performed, and corresponding diffraction patterns are plotted in 4.2. XRD pattern of SiOC powder is found to be amorphous in nature as confirmed by featureless broad pattern shown in Figure 4.2 (i). Because of the amorphous nature of SiOC ceramic and very thin coated layer (~1 μm) on SS304, no significant difference is observed between the XRD patterns of base substrate SS304 and two-fold SiOC-coated SS304, Figure 4.2 (ii, iii). Peak positions at 43.38°, 50.52° and 74.24° in diffraction patterns of SS304 and SiOC-coated SS304 are well matched with the standard referenced patterns of gamma-iron (γ-Fe, ICSD PDF code: 01-071-4649) and peak positions at 44.35°, 64.52° and 81.65° are matched with the alpha-iron (α-Fe, ICSD PDF code: 01-089-7194). SS304 was received in the form of a sheet from a supplier. In general, during the sheet forming operation steel undergoes plastic deformation (cold working/work hardening process) which can lead to formation of ferrite due to phase transformation. Earlier reported literature [138] also showed the presence of austenite and ferrite in the base substrate SS304.

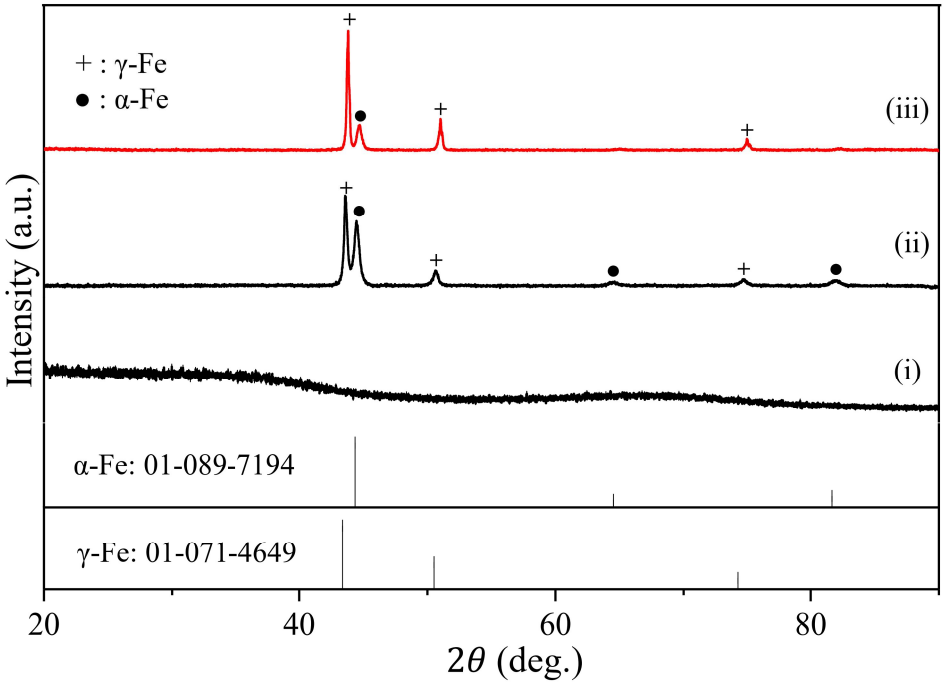

Figure 4.2 X-ray diffraction patterns of: (i) powdered SiOC obtained after pyrolysis of polysiloxane at 800°C, (ii) SS304 substrate, (iii) two-fold SiOC-coated SS304. Diffraction patterns of the reference α-Fe (ICSD PDF Code: 01-089-7194) and γ-Fe (ICSD PDF Code: 01-071-4649) are shown at the bottom.

4.1.3 Raman spectroscopy

As no significant difference in the XRD patterns of SS304 and SiOC-coated SS304 was observed, Raman spectroscopy was performed to verify the presence of SiOC coating on SS304. In Figure 4.3, base substrate SS304 does not show any Raman shifts due to the absence of Raman active vibrations, whereas SiOC-coated SS304 shows fluorescence – a typical behavior seen in PDCs obtained at lower pyrolysis temperatures (<1000°C) [135,136].

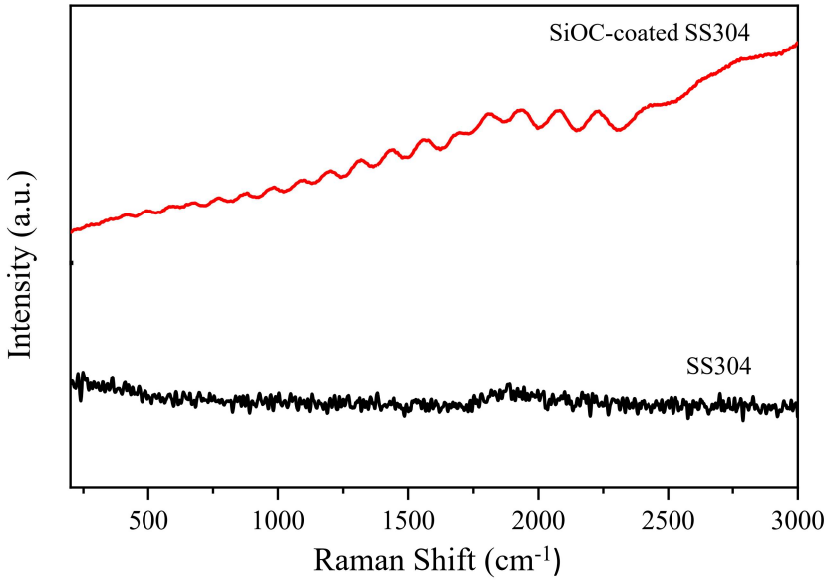

Figure 4.3 Raman spectrum of: (A) SS304, (B) two-fold SiOC coated SS304.

4.2 Electrochemical characterization of uncoated SS304 and SiOC-coated SS304

The corrosion resistance behavior of SS304 and SiOC-coated SS304 were analyzed using OCP, potentiodynamic polarization and EIS measurements in 0.6 M NaCl solution.

4.2.1 Open circuit potential (OCP) and potentiodynamic polarization measurements

OCP measurements of the samples were recorded for 1 h and stable potential was attained after 1 h, as shown in Figure 4.4. It is observed that for SiOC-coated SS304, the OCP value shifted towards the positive potential side indicating that SiOC-coating on SS304 improves corrosion resistance compared to SS304. A similar trend, improvement in OCP values after coating, was observed in the reported literatures [139–141].

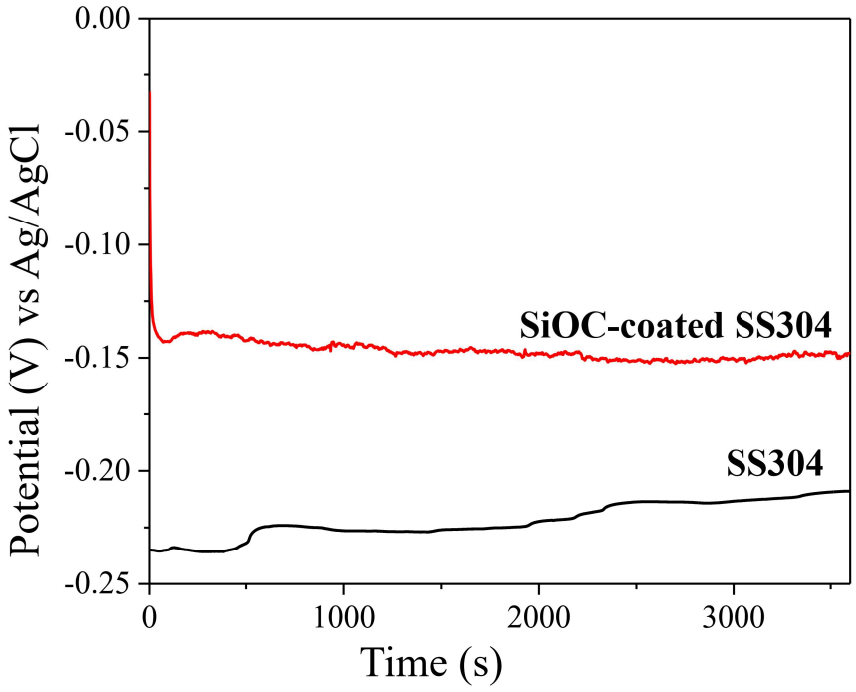

Figure 4.4 Open circuit potential of SS304 and two-fold SiOC-coated SS304 in 0.6 M NaCl solution.

Figure 4.5 shows the potentiodynamic polarization curves of SS304 and two-fold SiOC-coated SS304 samples in 0.6 M NaCl solution. Tafel extrapolation method was used to determine the electrochemical parameters and the obtained parameters are summarized in Table 4.1. Corrosion potential (E_{corr}) of the base SS304 is found to be -0.193 V, whereas for two-fold SiOC-coated is -0.137 V; these data indicates improvement in the corrosion potential of the coated sample. Polarization curve of SS304 (base material) shows that passive film breakdown (pitting potential) occurs at 0.241 V versus Ag/AgCl, whereas in two-fold SiOC-coated SS304 no passivity breakdown is observed. This behaviour implies that coating effectively prevents pitting corrosion by producing an inert layer over SS304 and even when the coating is subjected to hostile ions through a large potential range, it maintains its integrity and performance.

In Figure 4.5, passivity behavior in anodic branches of both curves is observed ─ with an increase in potential in anodic direction a constant current density is observed. Passivation current density (i_p) of SS304 is calculated as 2.55×10^{-7} A/cm^2, whereas for two-fold SiOC-coated SS304, passivation current density is found to be one decade lower (4.18×10^{-8} A/cm^2) than that of SS304. Corrosion current density (i_{corr}) of SiOC-coated SS304 is found to be about 4.14×10^{-9} A/cm^2, and that for uncoated SS304 about 4.56×10^{-7} A/cm^2. Significantly lower

i_{corr} and relatively higher E_{corr} values for SiOC-coated SS304 sample in comparison to that of SS304 confirms the enhanced protection effect of SiOC coating toward SS304.

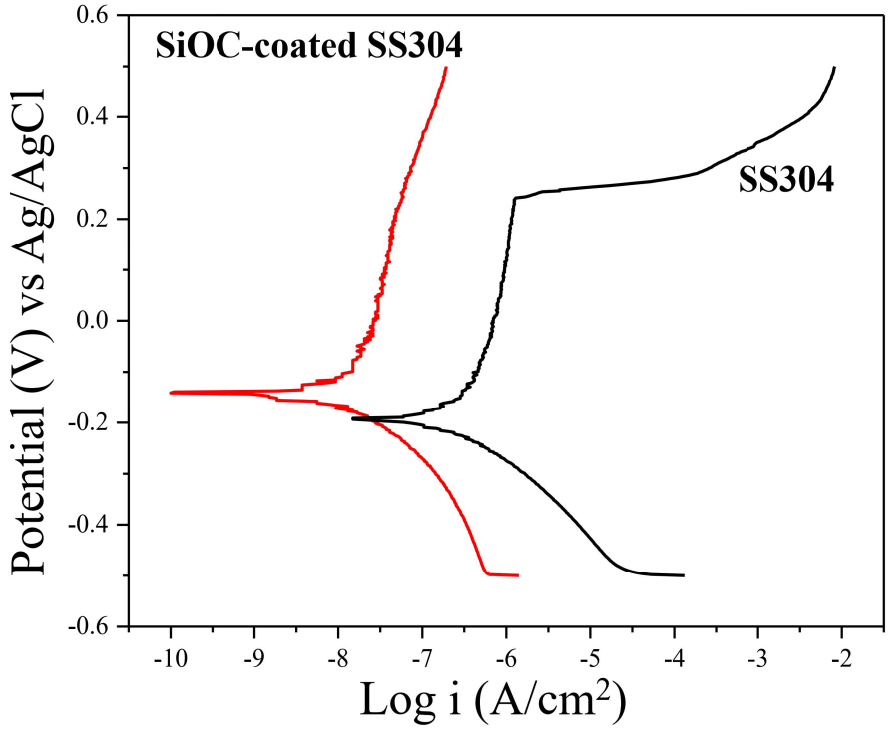

Figure 4.5 Potentiodynamic polarization curves of SS304 and two-fold SiOC-coated SS304.

Protection efficiency of the coated samples is calculated using the following formula [140,142]:

$$\text{Protection efficiency \% } (P.\ E.\ ) = \frac{i^{o}_{corr} - i^{c}_{corr}}{i^{o}_{corr}} \times 100$$

where i^{0}_{corr} is corrosion current density of uncoated SS304 substrate and i^{c}_{corr} is the corrosion current density of the SiOC-coated substrate. Protection efficiency determines how well a deposited layer prevents corrosion. P.E. of the SiOC-coated SS304 is found to be 99.08 % implies that the SiOC coating has significantly enhanced the corrosion protection behavior of SiOC-coated SS304 sample compared to that of uncoated SS304.

Table 4.1 Summary of various data obtained from polarization measurements of SS304 and two-fold SiOC-coated SS304 samples.

Sample	Corrosion potential, E_{corr} (V vs Ag/AgCl)	Passivation current density, i_p (A/cm^2)	Corrosion current density, i_{corr} (A/cm^2)	Polarization resistance, R_p (Ω cm^2)	Protection efficiency (%)
SS304	-0.193	2.55×10^{-7}	4.56×10^{-7}	2.07×10^{5}	-
SiOC-coated SS304	-0.137	4.18×10^{-8}	4.14×10^{-9}	2.01×10^{7}	99.08

4.2.2 Electrochemical impedance spectroscopy studies of SS304 and SiOC-coated SS304

To evaluate the corrosion behaviour/electrochemical reactions of coated sample and base substrate EIS measurements were performed. Obtained EIS experimental data of uncoated SS304 and SiOC-coated SS304 samples are analyzed using Nova 2.1.6 Software to fit equivalent circuit models. Nyquist and Bode plots of SS304 and SiOC-coated SS304 are represented in Figure 4.6 A–D. The real part of impedance (Z) is often represented by Z′ while the imaginary part is represented by Z″ as indicated in Nyquist plots of SS304 and SiOC-coated SS304, Figure 4.6 A and C. Nyquist plot of SS304 (Figure 4.6 A) shows lower arc diameter compared to that of SiOC-coated SS304 (Figure 4.6 C). In general, material with a lower arc diameter in the Nyquist plot represents lower corrosion resistance than that with a higher arc diameter. Also, Nyquist plot of SS304 does not show any straight line at lower frequencies (corresponding to higher Z′ values) indicating incomplete diffusion of chloride[143]. Nyquist plot of SiOC-coated SS304 (Figure 4.6 C) at low and intermediate frequencies shows a non-vertical line; non-vertical straight line at low frequencies is related to the diffusion of reactive species[144,145], which is prepresented by the inclusion of the Warburg element in the equivalent circuit in Figure 4.7 B. This diffusion occurs due the presence of porous nature of the SiOC coating (pore-size < 4-5 Å, as reported by Kumar et al. [108] for SiOC ceramic prepared from same polymer as used in this thesis work).

In general, semi-circles at higher frequencies give better charge transfer resistance properties at the coating/electrolyte interface, as can be seen in Figure 4.5 C, and a larger

impedance modulus at low frequencies gives better corrosion resistance performance [146,147]. At 0.1 Hz low frequency, |Z| of the SiOC-coated sample is found to be ~ 4.3× 10^5 Ω cm^2 whereas that of SS304 is approximately 2.28 × 10^4 Ω cm^2. Increase in |Z| implies improvement in corrosion resistance of SS304 after the deposition of SiOC coating.

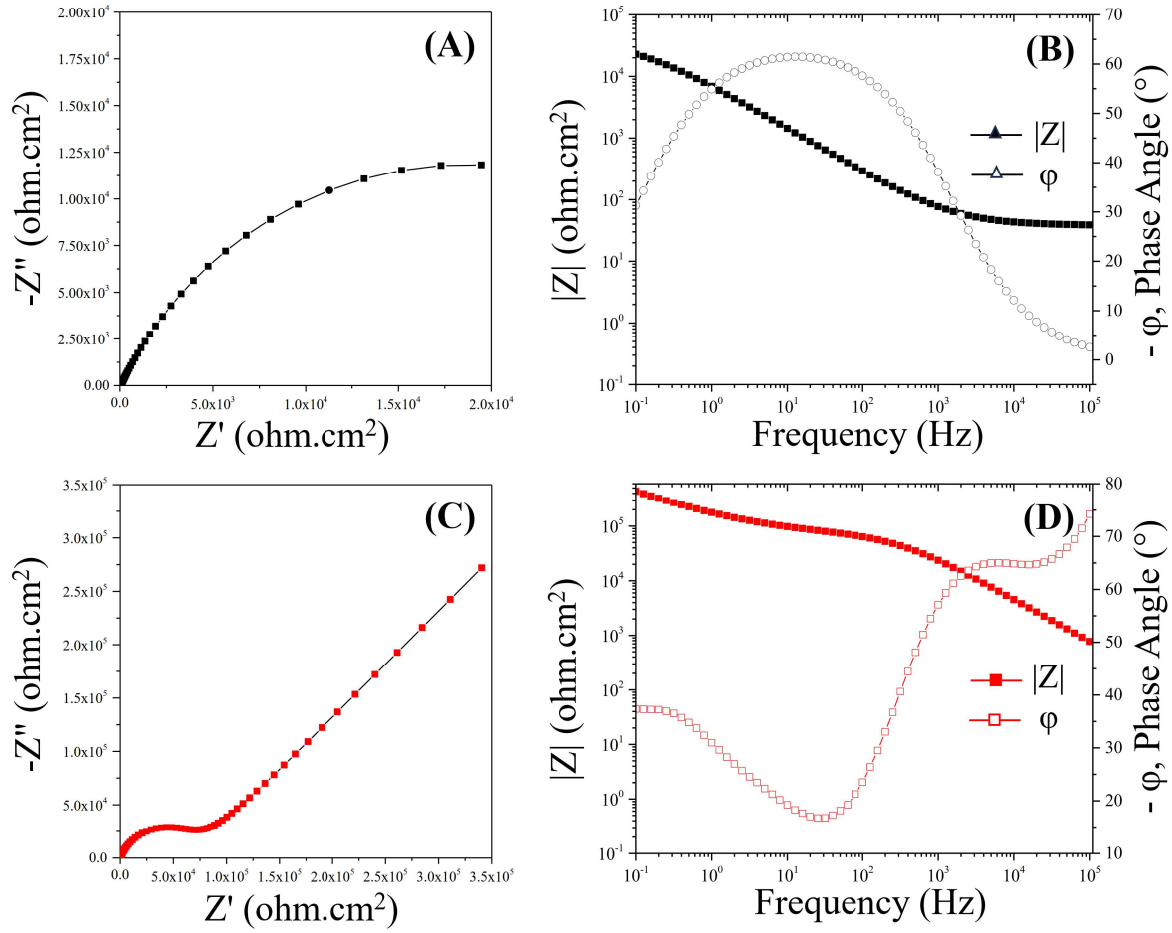

Figure 4.6 Nyquist and Bode plots of SS304 (A, B) and SiOC-coated SS304 (C, D).

The Bode plot of the coated sample (Figure 4.6 D) represents two-time constants (at ~0.20 Hz and ~5030 Hz), whereas the base substrate SS304 shows one-time constant (at ~7 Hz) in Figure 4.6 B. Two-time constants for the coated sample corresponds to electron charge transfer across the double layer at substrate/coating interface and at coated SiOC layer. An increase in phase angle at higher frequency (~5030 Hz) for SiOC-coated SS304 can be attributed to capacitive behavior of the SiOC coating associated with superior corrosion resistance.

Equivalent circuits corresponding to SS304 and SiOC-coated samples are shown in Figure 4.7. The equivalent circuit for SS304 (Figure 4.7 A) consists of solution resistance (R_s),

charge transfer resistance (R_{ct}), and double layer capacitance (CPE_{dl}) which are fitted with the EIS experimental data of SS304. In Figure 4.7 B, CPE_{dl} is replaced by constant phase element (CPE) due to the non-ideal capacitance behavior of the coated sample. Diffusion of the electrolyte in coating can cause the additional resistance, which is termed as Warburg impedance (W) element and therefore, it is inserted in the equivalent circuit. Impedance (Z) of CPE is represented as [148]

$$Z = \frac{1}{Y_0(j\omega)^n}$$

where Y_0 and n are parameters of CPE, j is the imaginary unit, and ω is the angular frequency of the sinusoidal signal; n indicates the deviation between the CPE and ideal capacitor. The value of n lies in the range of 0–1, when n is equal to 1, CPE represents a pure capacitance.

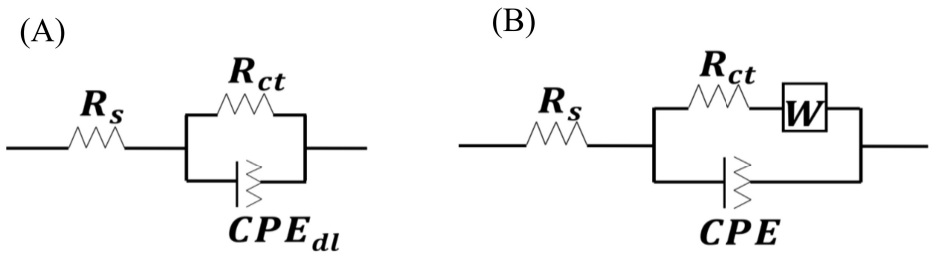

Figure 4.7 Equivalent circuit model of: (A) SS304 and (B) SiOC-coated SS304.

Table 4.2 Fitting parameters for equivalent circuits of SS304 and SiOC-coated SS304 (from Figure 4.7 A and B).

Sample	R_s (Ω cm^2)	R_{ct} (Ω cm^2)	CPE Y_0 (Ω^{-1} cm^{-2}S^n)	n	W Y_0 (Ω^{-1} cm^{-2}S^n)
SS304	38	3.74×10^4	3.53×10^{-6}	0.719	-
SiOC-coated SS304	38.3	7.29×10^4	3.80×10^{-9}	0.783	3.27×10^6

EIS measured data is consistent with potentiodynamic polarization measurement data, and both results confirmed that SiOC-coating protects SS304 in 0.6 M NaCl solution.

After electrochemical testing, EDS elemental mapping of SS304 and SiOC-coated SS304 samples were done to verify the morphology and corrosion products formed on the surface as shown in Figure 4.8. Breakdown of the passive film in SS304 led to the formation of pits and corrosion products (indicated by the presence of O) on the surface, as shown in Figure 4.8 A and in the corresponding enlarged portion of the marked region in Figure 4.8 B. This analysis

confirms formation of pits and corrosion products on the surface of the electrochemically tested SS304 whereas for electrochemically tested SiOC-coated SS304 pits and corrosion products are absent on the SiOC-coated surface.

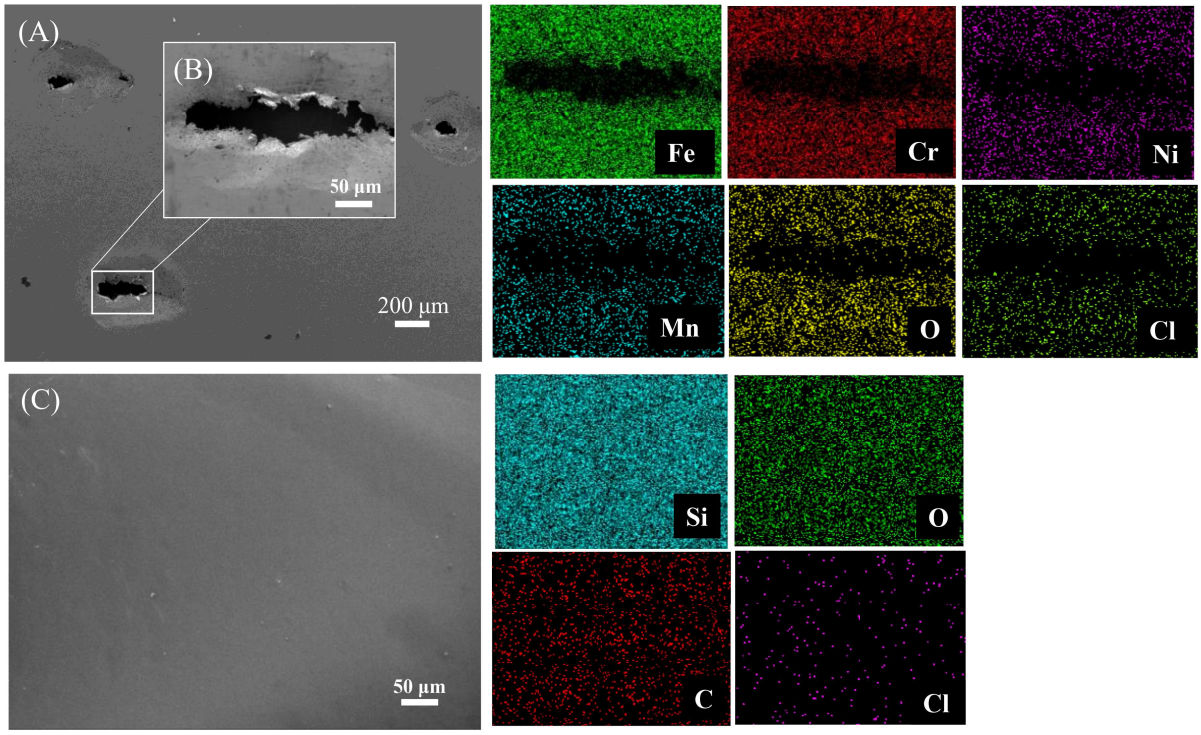

Figure 4.8 EDS elemental mapping of electrochemically tested: (A, B) SS304, and (C) SiOC-coated SS304 in 0.6 M NaCl solution.

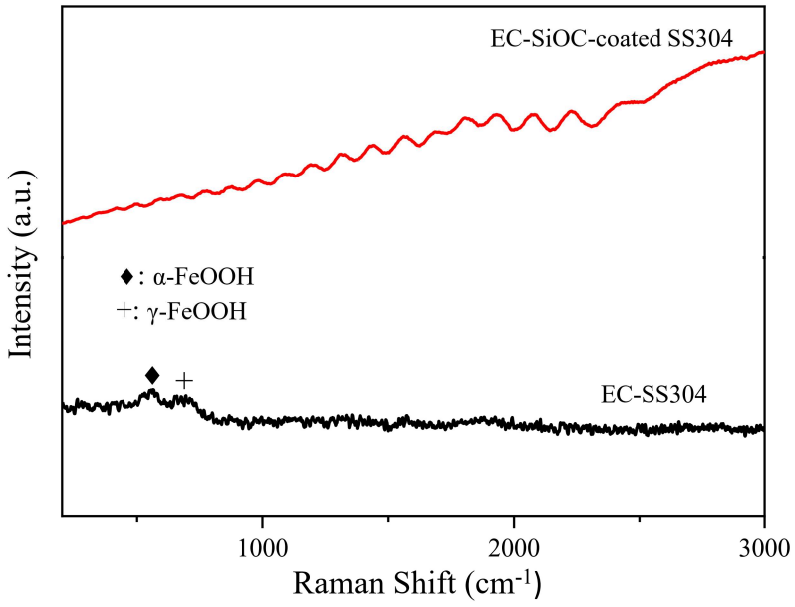

Figure 4.9 Raman spectrum of electrochemically (EC) tested SS304 and SiOC-coated SS304 in 0.6 M NaCl solution.

Qualitative analysis of corrosion products formed on the surfaces was also verified by Raman spectroscopy. Figure 4.9 shows formation of corrosion products such as iron oxyhydroxide hydrates corresponding to Raman shifts at 554 cm^{-1} and 701 cm^{-1}, similar to as in reported literature [149], however, electrochemically tested SiOC-coated SS304 shows absence of any corrosion product.

The characterization results including potentiodynamic polarization tests, EIS measurements, EDS elemental mapping, and Raman spectroscopy, clearly indicate that SiOC-coated SS304 exhibits superior corrosion resistance compared to bare SS304 in a 0.6 M NaCl solution. Compared to the previous coatings on SS304, experimental results of SiOC-coated SS304 showed a considerable improvement in the corrosion resistance of SS304 in a 0.6 M NaCl solution, as listed in Table 4.3.

Compared to the performance of previous coatings on SS304, the present results of SiOC-coated SS304 indicate a considerable improvement in the corrosion resistance of SS304 in a 0.6 M NaCl solution, as listed in Table 4.3.

Table 4.3 Comparison of corrosion rates of various ceramic coatings on SS304 in 0.6 M NaCl environment.

Working electrode	**Corrosion potential, E_{corr} (mV)**	**Corrosion current density, i_{corr} (A/cm^2)**	**Reference**
Muscovite/TiO_2-coated SS304	-503 vs SCE	5.21×10^{-6}	[150]
Ta_3N_5-coated SS304	-196 vs SCE	5.53×10^{-7}	[151]
TiO_2-ZrO_2-coated SS304	-157 vs SCE	5.01×10^{-8}	[152]
SiOC-coated SS304	-133 vs Ag/AgCl	4.14×10^{-9}	Chapter 4, in this thesis work

4.3 Immersion testing of samples

SS304 and two-fold SiOC-coated SS304 samples were immersed in 0.6 M NaCl at room temperature and weight loss was recorded after each immersion interval (24 h, 72 h, 120 h and 168 h) as per ASTM G31-72 (2004) standard. The readability of the weighing balance METLER TOLEDO is 0.0001g. The calculated mean mass loss and mean corrosion rate data

are presented in Tables 4.4 and 4.5 using the equation mentioned in experimental procedure section 2.6. SiOC coated-SS304 shows better corrosion resistance than SS304 for longer immersion time.

Table 4.4 Mean mass loss and mean corrosion rate of SS304 after immersion test at distinct intervals.

Immersion time	24 h	72 h	120 h	168 h
Mean mass loss ($mg/cm^2/day$)	0.5500	0.3933	0.400	0.3500
Mean corrosion rate (mm/y)	0.2545	0.18205	0.1851	0.1644

Table 4.5 Mean mass loss and mean corrosion rate of SiOC-coated SS304 after immersion test at distinct intervals.

Immersion time	24 h	72 h	120 h	168 h
Mean mass loss ($mg/cm^2/day$)	0	0.0666	0.0800	0.0642
Mean corrosion rate (mm/y)	0	0.1261	0.1513	0.1216

4.4 Adhesion test

An adhesive tape test (ASTM D3359) was performed to ensure that SiOC coating is strongly adhered to the base substrate SS304. The surface of the coating was scratched by a sharp knife to have an "X" pattern (Figure 4.10 A) and then adhesive tape was pasted to the "X" pattern (Figure 4.10 B). Afterwards, the tape was peeled off (Figure 4.10 C). After peeling off the tape, it is found that the coating surface had not changed. On the tape, a subtle pattern can be seen in the marked region (Figure 4.10 D), which was caused by the scratch. This test demonstrates good adhesion between SiOC ceramic coating and SS304 substrate.

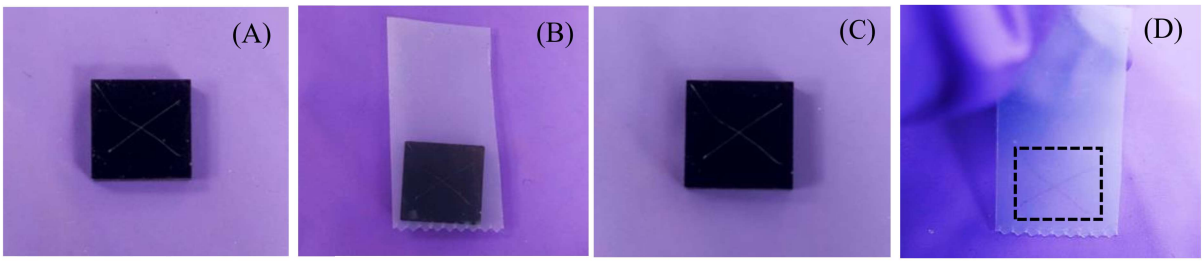

Figure 4.10 Adhesion test: (A) SiOC-coated SS304 with "X" pattern scratch, (B) tape-coated sample, (C) SiOC-coated SS304 after the tape is peeled off, and (D) adhesive tape after peeling.

4.5 Corrosion mechanisms of SS304 and SiOC-coated SS304

Based on the analysis of potentiodynamic polarization tests, EIS data and structural characterization of the tested samples, schematic of corrosion mechanisms of samples are

presented in Figure 4.11. In stainless steel 304, the naturally passive layer (mainly chromium oxide) acts as a protective barrier for further corrosion of steel; however, in an aggressive environment (Cl^-), this protective layer is vulnerable to breakdown and leads to corrosion. In the current work, SS304 undergoes pitting corrosion and the corrosion mechanism is schematically represented in Figure 4.11 A — based on data obtained from potentiodynamic polarization measurements (Figure 4.5) and EDS elemental mapping of SS304 (Figure 4.8 A). In the case of the SiOC-coated SS304 sample, a significant decrease in corrosion current density to ~4.56×10^{-9} A/cm^2 (Table 4.1) indicates that SiOC ceramic coating is geometrically blocking the Cl^- ions and protects against corrosion as depicted in Figure 4.11 B.

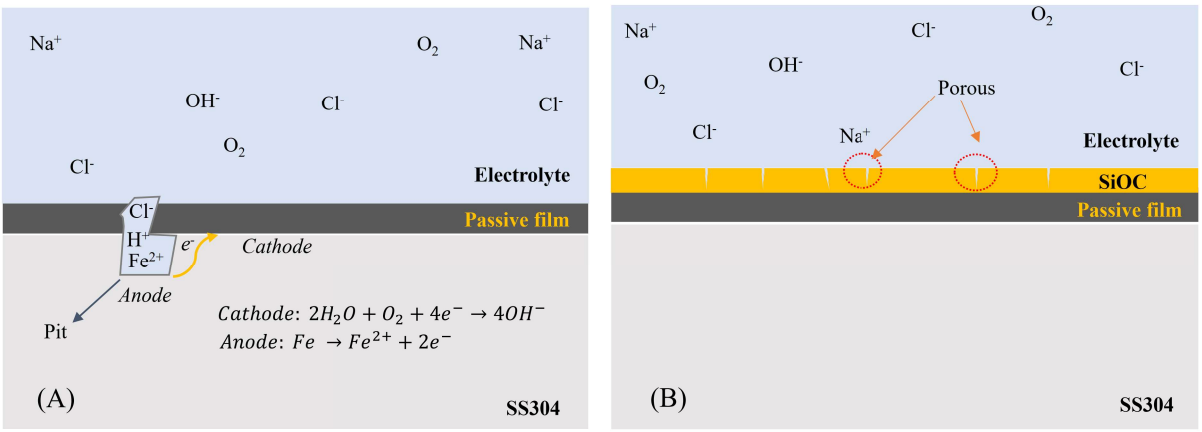

Figure 4.11 Schematic representation of corrosion mechanism of: (A) SS304, and (B) two-fold SiOC-coated SS304 in 0.6 M NaCl solution.

Chapter 5. Corrosion protection performance of polymer-derived SiCN-coated SS304

This chapter discusses enhanced corrosion protection performance of SiCN-coated SS304. SS304 was dip-coated with a polysilazane (Durazane 1800) solution 50 by vol% in anhydrous toluene followed by pyrolysis under argon environment at 800 °C to develop SiCN ceramic layer on SS304. The results of structural characterization and electrochemical characterization of uncoated SS304 and SiCN-coated SS304 performed in 0.6 M NaCl solution are described in the following sections.

5.1 Structural characterization of uncoated SS304 and SiCN-coated SS304

5.1.1 Scanning electron microscopy (SEM)

Base substrate SS304 after polishing was coated with a polymer-derived SiCN ceramic layer by applying the pyrolysis process and coating method as described in experimental procedures (chapter 2, sections 2.1 and 2.3). SiCN coating was found to be crack-free with a thickness of about ~3 µm after three-fold coating and pyrolysis steps as shown in Figure 5.1.

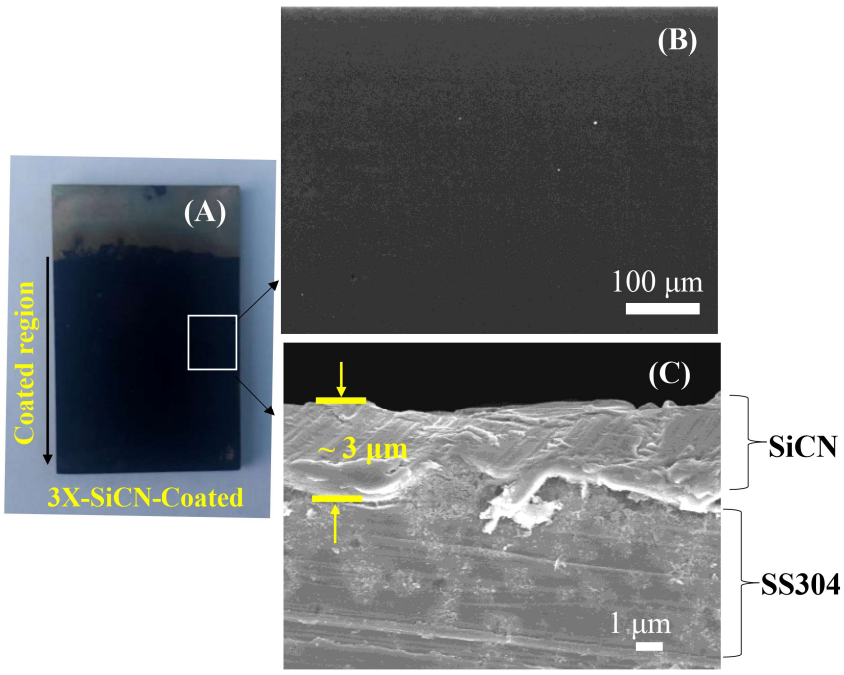

Figure 5.1 (A) Digital image of three-fold SiCN-coated SS304. Field emission scanning electron microscopy (FESEM) images of: (B) crack-free surface of SiCN coated layer, and (C) cross-sectional view of SiCN-coated SS304.

5.1.2 X-ray diffraction (XRD)

X-ray diffraction measurements of SS304, SiCN powder synthesized at 800 °C, and SiCN-coated SS304 were performed. SiCN powder synthesized at 800 °C was found to be amorphous in nature with a featureless broad x-ray diffraction pattern as shown in Figure 5.2 (i). Because of coating of a thin amorphous SiCN layer coated on SS304, it is difficult to identify the difference in XRD patterns of uncoated SS304 and SiCN-coated SS304, Figure 5.2 (ii, iii). Peak positions at 43.38°, 50.52° and 74.24° in diffraction patterns of SS304 and three-fold SiCN-coated SS304 are matched with the standard referenced patterns of gamma-iron (γ-Fe, ICSD PDF code: 01-071-4649) and peak positions at 44.35°, 64.52° and 81.65° are matched with the alpha-iron (α-Fe, ICSD PDF code: 01-089-7194).

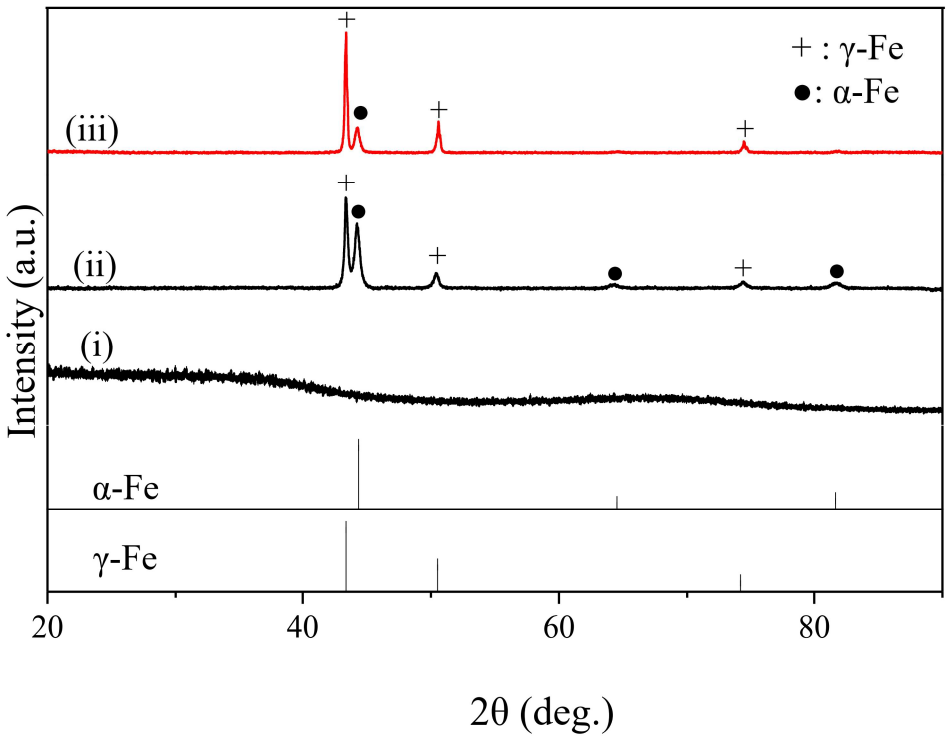

Figure 5.2 X-ray diffraction patterns of: (i) powdered SiCN obtained after pyrolysis of polysilazane at 800°C, (ii) SS304 substrate, (iii) three-fold SiCN-coated SS304. Diffraction patterns of the reference α-Fe (ICSD PDF Code: 01-089-7194) and γ-Fe (ICSD PDF Code: 01-071-4649) are shown at the bottom.

5.1.3 Raman spectroscopy

As the synthesized SiCN ceramic is amorphous in nature, therefore, Raman spectroscopy was performed to verify the presence of SiCN coating on ceramic coated SS304. In Figure 5.3, SS304 does not show any Raman shifts due to the absence of Raman active vibration bonds,

whereas SiCN-coated SS304 sample shows a fluorescence behaviour which is normally observed for polymer-derived ceramics synthesized at lower pyrolysis temperatures (< 1000°C).

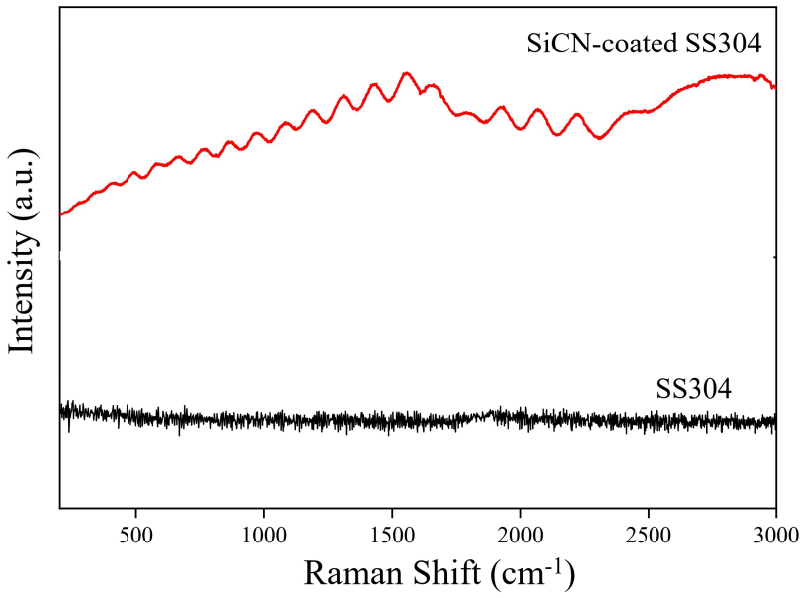

Figure 5.3 Raman spectrum of: (A) SS304, (B) three-fold SiCN-coated SS304.

5.2 Electrochemical characterization of uncoated SS304 and SiCN-coated SS304

Electrochemical characterization to assess corrosion resistance behavior of SS304 and SiCN-coated SS304 were studied using OCP, potentiodynamic polarization and EIS measurements in 0.6 M NaCl solution.

5.2.1 Open circuit potential (OCP) and potentiodynamic polarization measurements

Before performing EIS and polarization measurements, open circuit potential (OCP) measurements were performed to obtain a stable equilibrium potential as shown in Figure 5.4. Samples were immersed in the electrolyte for a particular period as electrochemical tests are performed only after observing the stable OCP values. OCP was stable for both samples after 1 h. Moreover, in case of SiCN-coated SS304, OCP was shifted to the noble side (-0.037 V, relatively positive potential) compared to uncoated SS304 (-0.186 V); this indicates that SiCN-coating on SS304 enhances corrosion resistance.

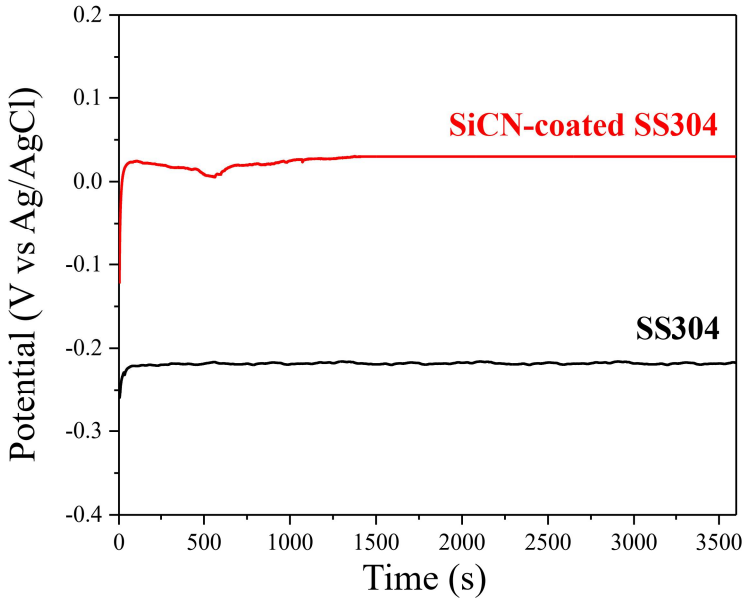

Figure 5.4 Open circuit potential (OCP) measurements of SS304 and three-fold SiCN-coated SS304 in 0.6 M NaCl electrolyte solution.

Further, to verify the effect of coating on the corrosion resistance of SS304 potentiodynamic polarization tests performed. From the polarization curves of SS304 and SiCN-coated SS304 (Figure 5.5), corrosion potential (E_{corr}), corrosion current density (i_{corr}), passivation current density (i_{pass}), and breakdown potential (E_p) were calculated and corresponding values are listed in Table 5.1. E_{corr} and i_{corr} have been obtained from the Tafel extrapolation method. Corrosion potentials (E_{corr}) of SS304 substrate and SiCN-coated SS304 were calculated to be -0.186 and -0.037 V, respectively, Figure 5.5. The black curve corresponding to SS304 in Figure 5.5 shows that in the anodic direction at a potential (0.28 V vs Ag/AgCl) there is a significant increase in the current density attributed to the breakdown of passive film corresponding to breakdown potential (pitting potential). In three-fold SiCN-coated SS304, no passivity breakdown is observed confirming SiCN coating is effectively preventing pitting failure of SS304 by forming a chemically resistant layer (SiCN) over SS304.

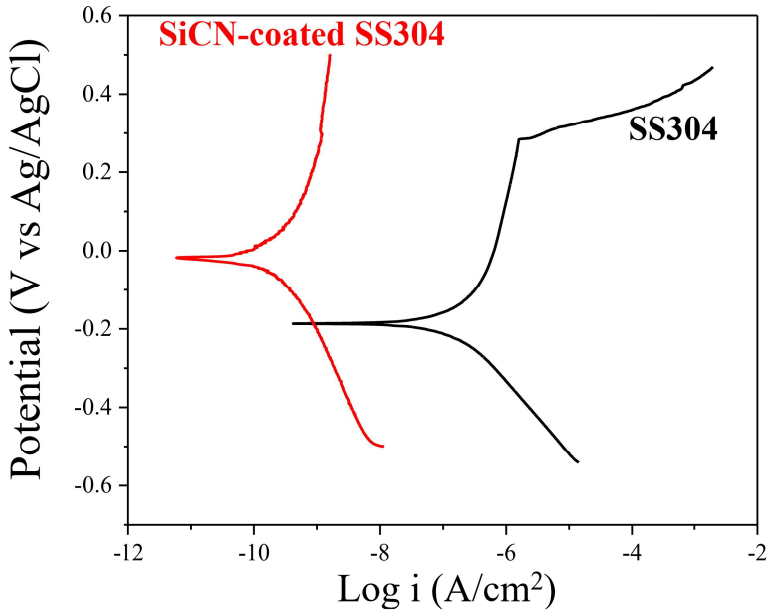

Figure 5.5 Potentiodynamic polarization curves of SS304 and three-fold SiCN-coated SS304.

The passivation current density (i_p) of SS304 is found to be 3.98×10^{-7} A/m^2, whereas for SiCN-coated SS304 passivation current density is measured as 1.94×10^{-9} A/m^2 which is almost two decades lower than that of SS304; material with a lower passivation current density gives better corrosion resistance. Corrosion current density (i_{corr}) of SS304 is calculated to be 1.5196×10^{-7} A/cm^2 whereas for SiCN-coated SS304 it is found to be 4.2004×10^{-10} A/cm^2. As i_{corr} of SiCN-coated SS304 is shifted to much lower current density values compared to base SS304, this behavior implies enhanced corrosion protection after deposition of the SiCN layer on SS304.

The protection efficiency of the coating is estimated using the formula:

$$\text{Protection efficiency \% } (P.\ E.\ ) = \frac{i^o_{corr} - i^c_{corr}}{i^o_{corr}} \times 100$$

where i^0_{corr} is corrosion current density for uncoated substrate and i^c_{corr} is the corrosion current density of the SiCN-coated substrate. P.E. of the SiCN-coated SS304 is found to be 99.72 % indicating significantly enhanced the corrosion protection behavior of SiCN-coated SS304 compared to that of uncoated SS304.

Table 5.1 Corrosion potential (E_{corr}) and corrosion current density (i_{corr}) of SS304 and SiCN-coated SS304 samples.

Sample	Corrosion potential, E_{corr} (V vs Ag/AgCl)	Passivation current density, i_p (A/cm^2)	Corrosion current density, i_{corr} (A/cm^2)	Polarization resistance, R_p (Ω cm^2)	Protection efficiency (%)
SS304	-0.186	3.98×10^{-7}	1.5196×10^{-7}	3.10×10^{5}	-
SiCN-coated SS304	-0.037	1.94×10^{-9}	4.2004×10^{-10}	2.38×10^{8}	99.72

5.2.2 Electrochemical impedance spectroscopy studies of SS304 and SiCN-coated SS304

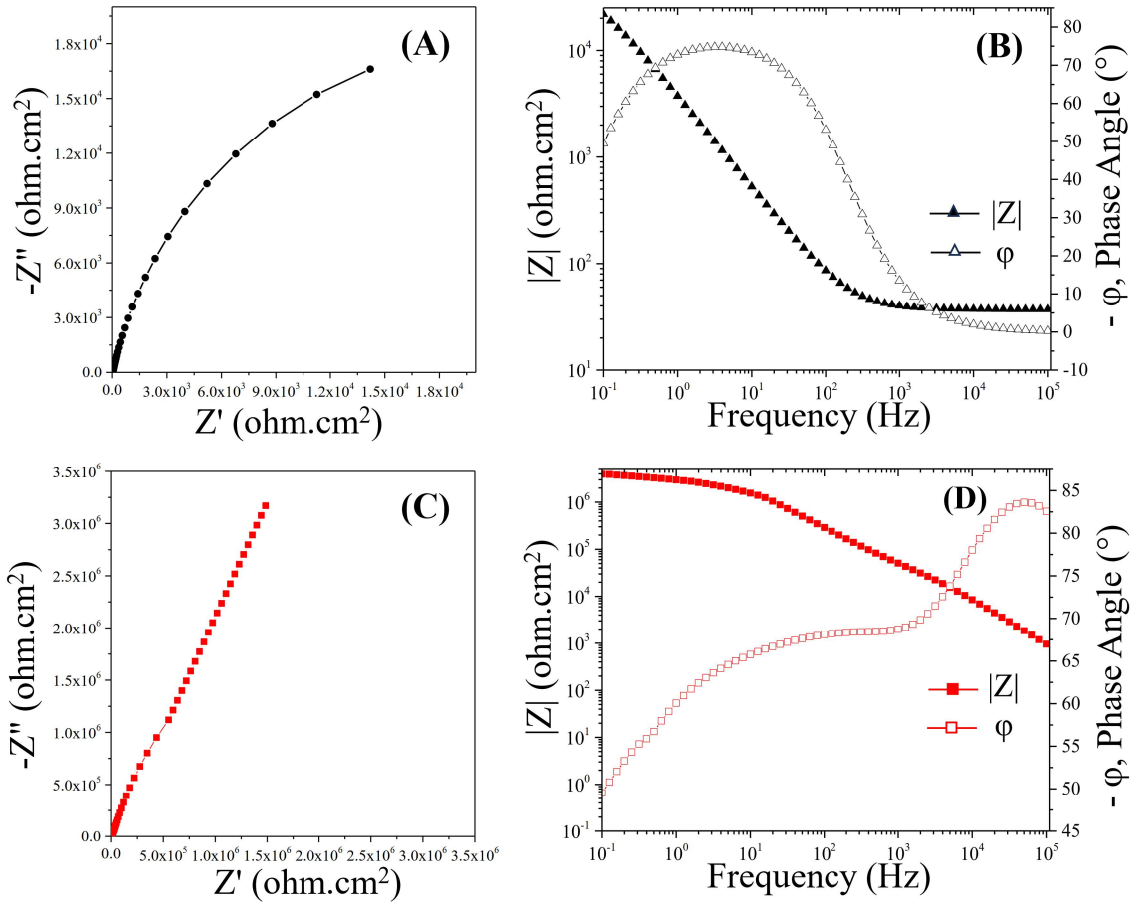

Figure 5.6 Nyquist and Bode plots of SS304 (A, B) and SiCN-coated SS304 (C, D).

EIS measurements were carried out to gain more information about the corrosion resistance properties of the coated sample and base substrate. Nyquist and Bode plots of SS304 are depicted in Figure 5.6 (A, B) and corresponding plots of SiCN-coated SS304 are represented

in Figure 5.6 (C, D). The experimental EIS spectra of SS304 and SiCN-coated SS304 are analyzed with the help of Nova 2.1.6 software, and these equivalent circuits are illustrated in Figure 5.7 (A, B). In equivalent circuit models, R_s represents the solution resistance, R_{ct} is the charge transfer resistance and CPE_{dl} represents the double-layer capacitance due to the formation of a double layer at the interface of the sample/electrolyte. R_c in Figure 5.7 B represents the resistance of SiCN coating, which hinders the electrolyte penetration towards the coating and CPE_{dl} is replaced by a constant phase element (CPE_c) due to the nonideal capacitive behavior of the coating response [147].

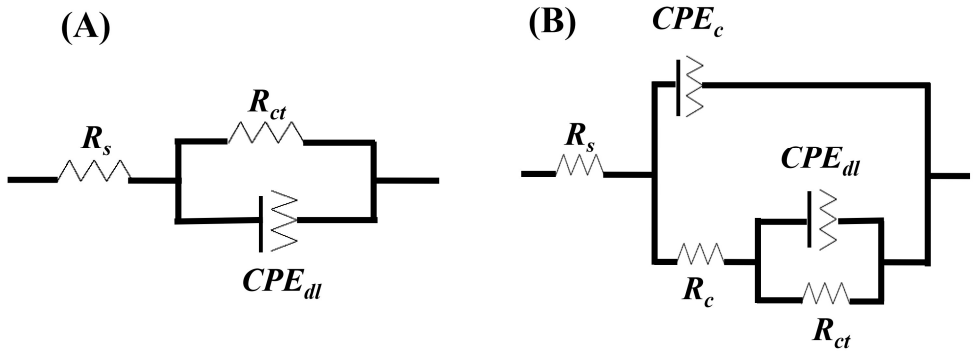

Figure 5.7 Equivalent circuit model of: (A) SS304, and (B) SiCN-coated SS304.

Coating performance is evaluated by elemental values of the equivalent circuits. The obtained values of equivalent circuits are shown in Table 5.2. Nyquist plot in Figure 5.6 A shows a half semicircle for SS304 at a low-frequency range, which does not show any straight line, indicating the incomplete diffusion of the chloride. For SiCN-coated SS304, R_{ct} value is found to be ~8.98×10^7 Ω cm^2 implies high corrosion resistance compared to SS304 (~4.48×10^4 Ω cm^2).

Bode plots of SiCN-coated SS304 (Figure 5.6 D) shows a higher impedance modulus (|Z|) at lower frequencies than uncoated SS304 (Figure 5.6 B). At low frequency of 0.1 Hz, impedance modulus (|Z|) of SiCN-coated SS304 is found to be 3.93×10^6 Ω cm^2 whereas that of uncoated SS304 is found to be 2.17×10^4 Ω cm^2. The increased impedance value of the coated sample implies obstruction of the ion diffusion process, thereby enhancing corrosion resistance. Bode plot of the SiCN-coated SS304 (Figure 5.6 D) represents two-time constants (at ~200 Hz and 50000 Hz), whereas the base substrate SS304 shows one-time constant (at ~3 Hz) in Figure 5.6 B. Two-time constants measured for coated sample corresponds to electron charge transfer across the double layer at the substrate/coating interface and at coated SiCN layer. An increase in phase angle at higher frequency (~50000 Hz) is attributed to capacitive

behavior of the SiCN coating associated with superior corrosion resistance. EIS measured data is consistent with potentiodynamic polarization measurement data, and both results confirm that SiCN-coating protects SS304 in 0.6 M NaCl solution.

Table 5.2 Fitting parameters for equivalent circuits of SS304 and SiCN-coated SS304 (from Figure 5.7 A,B.

Sample	R_s (Ω cm^2)	R_{ct} (Ω cm^2)	CPE_{dl} Y_0 (Ω^{-1} cm^{-2}s^n)	n	R_C (Ω cm^2)	CPE_c Y_0 (Ω^{-1} cm^{-2}s^n)	N
SS304	37.1	4.48×10^4	53.3×10^{-6}	0.77	-	-	
SiCN-coated SS304	55.1	8.98×10^7	28.3×10^{-9}	0.99	3.27×10^4	1.93×10^{-9}	0.69

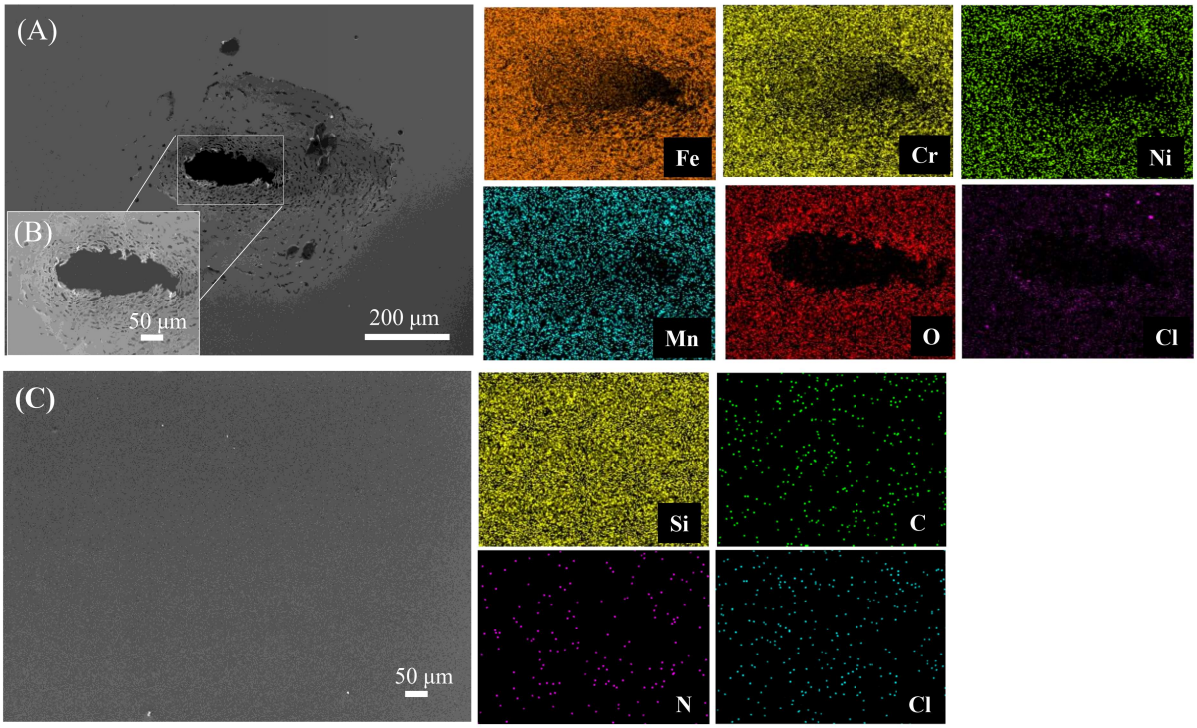

Figure 5.8 EDS elemental mapping of electrochemically tested: (A, B) SS304 and (C) SiCN-coated SS304 in 0.6 M NaCl solution.

To confirm the formation of corrosion products on surface EDS elemental mapping of electrochemically tested SS304 and three-fold SiCN-coated SS304 samples were performed, as illustrated in Figure 5.8. After electrochemical testing of uncoated SS304, breakdown of the passive film led to the formation of pits and corrosion products (presence of O) on the surface, as shown in Figure 5.8 A and in the corresponding enlarged portion of the marked region in

Figure 5.8 B. Conversely, pit formation and corrosion products were absent on the surface of electrochemically tested SiCN-coated SS304 sample, Figure 5.8 C.

Qualitative analysis of the corrosion products formed on the surfaces was examined using Raman spectroscopy. After electrochemical testing in 0.6 M NaCl solution, uncoated SS304 (Figure 5.9) shows Raman shifts at peak positions of 574 cm^{-1} and 708 cm^{-1} which indicates the formation of corrosion products such as iron oxyhydroxide hydrates. Electrochemically tested SiCN-coated SS304 shows absence of a corrosion product.

Based on the abovementioned characterization results (polarization curves, EIS measurements, EDS elemental mapping, and Raman spectroscopy), it can be concluded that SiCN-coated SS304 exhibits superior corrosion resistance compared to bare SS304 in a 0.6 M NaCl solution. Compared to the previous works done by other coatings on SS304, the results obtained for SiCN-coated SS304 shows a significant improvement in the corrosion resistance of SS304 in a 0.6 M NaCl solution, Table 5.3.

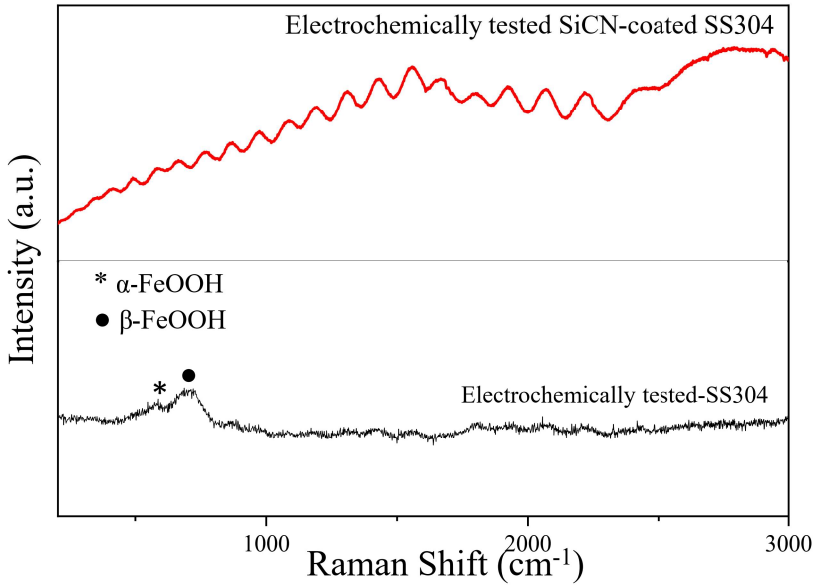

Figure 5.9 Raman spectrum of electrochemically tested SS304 and three-fold SiCN coated SS304.

Table 5.3 Comparison of corrosion rates of various ceramic coatings on SS304 in 0.6 M NaCl environment.

Working electrode	**Corrosion potential, E_{corr} (mV)**	**Corrosion current density, i_{corr} (A/cm^2)**	**Reference**
PHPS-derived SiO_2 coated AISI 304	-90 vs Ag/AgCl	3×10^{-10}	[141]
TiO_2-ZrO_2-coated SS304	-157 vs SCE	5.01×10^{-8}	[152]
Muscovite/TiO_2-coated SS304	-503 vs SCE	5.21×10^{-6}	[150]
Ta_3N_5-coated SS304	-196 vs SCE	5.53×10^{-7}	[151]
SiOC-coated SS304	-133 vs Ag/AgCl	4.14×10^{-9}	Chapter 4, in this thesis work
SiCN-coated SS304	-0.037 vs Ag/AgCl	4.20×10^{-10}	Chapter 5, in this thesis work

5.3 Immersion testing of samples

The long-term corrosion behaviour of the samples were analyzed by performing immersion testing. SS304 and SiCN-coated SS304 samples were immersed in 0.6 M NaCl at room temperature, and weight loss was recorded after each immersion interval (24 h, 72 h, 120 h and 168 h). Calculated mean mass loss and mean corrosion rate data are presented in Table 5.4 and Table 5.5. The data indicates that SiCN-coated SS304 shows better corrosion resistance than SS304 for longer immersion time.

Table 5.4 Mean mass loss and mean corrosion rate of SS304 after immersion at distinct intervals.

Immersion time	24 h	72 h	120 h	168 h
Mean mass loss (mg/cm^2/day)	0.5500	0.3933	0.400	0.3500
Mean corrosion rate (mm/y)	0.2545	0.18205	0.1851	0.1644

Table 5.5 Mean mass loss and mean corrosion rate of SiCN-coated SS304 after immersion at distinct intervals.

Immersion time	24 h	72 h	120 h	168 h
Mean mass loss (mg/cm^2/day)	0.0909	0.0358	0.0527	0.0376
Mean corrosion rate (mm/y)	0.1719	0.0678	0.0997	0.0712

5.4 Adhesion test

An adhesive tape test of SiCN-coated SS304 sample was performed as per ASTM D3359 standard test. The surface of SiCN coated layer was scratched by a sharp knife to have an "X" pattern (Figure 5.10 A) and then adhesive tape was pasted to the "X" pattern on SiCN layer (Figure 5.10 B) and then the tape was peeled off (Figure 5.10 C). After peeling off the tape, SiCN coating surface was not changed and on the tape a subtle pattern was seen in the marked region (Figure 5.10 D) caused by the scratch. This test confirms good adhesion between SiCN ceramic coated layer and SS304 substrate.

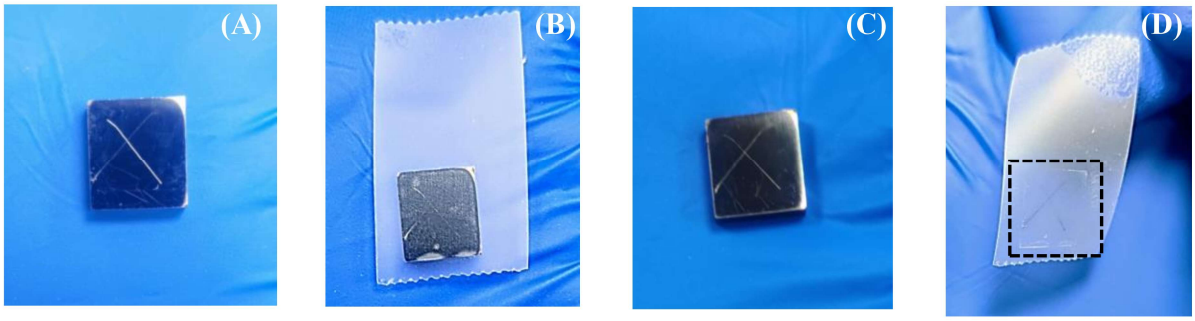

Figure 5.10 Adhesion test: (A) SiCN-coated SS304 with "X" pattern scratch, (B) tape coated sample, (C) SiCN-coated SS304 after the tape is peeled off, and (D) adhesive tape after peeling.

5.5 Corrosion mechanisms of SS304 and SiCN-coated SS304

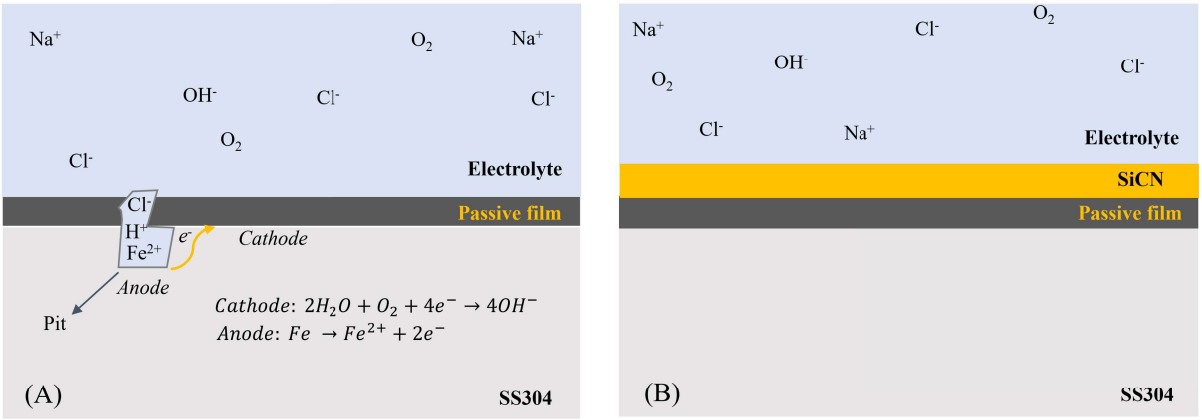

Figure 5.11 Schematic representation of corrosion mechanism of: (A) SS304, and (B) three-fold SiCN-coated SS304 in seawater environment.

Based on the analysis of potentiodynamic polarization, EIS data and structural characterization of the tested samples schematic of corrosion mechanisms of samples are presented in Figure 5.11. In SS304, the passive layer (mainly chromium oxide) serves as a protective barrier against further corrosion of the steel. However, in corrosive solutions which contain chloride ions (Cl^-

), this protective layer becomes prone to corrosion. Based on observations of the current investigation, it is observed that SS304 experiences pitting corrosion as evidenced by the polarization curve presented in Figure 5.5 and this is schematically illustrated in Figure 5.11 A. From polarization data (Figure 5.5), it was observed that the coated sample showed a wide passive region which indicates that corrosion potential is shifted to the positive side compared to the base substrate and corrosion current density was very low (4.2×10^{-10} A/cm^2). This decrease in current density implies that the SiCN coating effectively protects SS304 against corrosion in 0.6 M NaCl by hindering the transport of Cl^- ions, as illustrated in Figure 5.11 B. From the EIS data, Nyquist plots (Figure 5.6 A, C) show a very large semi-circle loop for SiCN-coated SS304 compared to SS304 which indicates passive nature of SiCN coating, and high value of charge transfer resistance of SiCN-coated SS304 (R_{ct} = 8.98×10^7 Ω cm^2, Table 5.2) signifies strong barrier protection with no sign of diffusion related behavior in the coating [153]. EDS mapping (Figure 5.8) and Raman spectroscopy data (Figure 5.9) also confirmed absence of corrosion products was formed on the surface after electrochemical testings.

Chapter 6. Conclusions and outlook

In this thesis work, enhancement of corrosion protection behavior of stainless steel 304 (SS304) coated with amorphous polymer-derived ceramics layers is investigated in 0.6 M NaCl solution. Two different classes of polymer-derived ceramics ─ silicon-oxycarbide (SiOC) and silicon carbonitride (SiCN) ─ were synthesized and characterized. Amorphous ceramic layers were deposited on SS304 by using dip-coating method. Structural characterization of the coated samples were performed using different characterization techniques and corrosion resistance of the samples was evaluated by electrochemical testing of the base substrate (SS304), SiOC-coated SS304, and SiCN-coated SS304.

Two precursors, namely vinyl-functionalized polysiloxane (XP RV200) and polysilazane (Durazane 1800) were used to synthesize SiOC and SiCN ceramics. The structure of these precursors were studied using liquid state NMR and ATR-FTIR spectroscopic methods. Thermal analysis of the precursors at 800 °C under argon environment shows ceramic yields of about 33 % (SiOC) and 71% (SiCN) by mass. XRD analyses of SiOC and SiCN ceramics synthesized at 800 °C showed formation of amorphous ceramics.

In the first phase of this work, polymer-derived ceramic coatings were optimized for deposition of ceramic layers on SS304 using different precursor concentrations. At first, vinyl-functionalized polysiloxane with three different concentrations of 40 vol%, 50 vol%, and 60 vol% diluted with anhydrous toluene were deposited on SS304 substrate using dip-coating process. After polymer deposition, samples were subsequently pyrolyzed to a specified pyrolysis temperature (800 °C) to get a ceramic layer. This deposition and pyrolysis process was repeated to achieve successive layers and a uniform coating. Coated substrates were characterized using optical microscopy. Optical microscopic images of ceramic coated samples with 40 vol% solution showed non-uniform coating, 50 vol% coated samples were found to be uniform crack-free SiOC coating and 60 vol% samples showed defects like bubble formation on the coated surface. After verifying the morphology of the coated samples, 50 vol% precursor with two-fold coatings was chosen as the optimized coating. Whereas for SiCN coating on SS304, three-fold coatings with 50 vol% polysilazane solution was considered as the optimized coating parameters. After optimizing the coating parameters, further characterization was carried out of ceramic-coated samples. Raman spectroscopy measurements of the coated

samples show fluorescence behaviour which confirmed the deposition of SiOC and SiCN coatings on SS304.

In the next step, an amorphous-SiOC ceramic layer with a thickness of about ~1 μm was deposited after two-fold coatings on SS304 by dip-coating in polysiloxane solution followed by pyrolysis at 800 °C under an argon environment. Electrochemical corrosion resistance performance of SiOC-coated SS304 was performed in 0.6 M NaCl solution using open circuit potential (OCP), potentiodynamic polarization, and electrochemical impedance spectroscopy (EIS) methods. OCP measurements of the coated sample was found to be changed towards noble side compared to SS304. After performing potentiodynamic polarization tests, SS304 showed pitting breakdown at 0.241 V vs Ag/AgCl, no pitting characteristics was observed for SiOC-coated SS304. Corrosion potential (E_{corr}) of the coated sample was found to be -0.137 V and for SS304 (-0.193 V). Corrosion current density (i_{corr}) of the coated sample was decreased by two orders of magnitude (4.14×10^{-9} A/cm^2) compared to that of SS304 (4.56×10^{-7} A/cm^2), and the protection efficiency (P.E) of the coating is found to be ~99.08%. EIS measurements of SiOC-coated sample showed a decrease in CPE_C (3.80×10^{-9} Ω^{-1} cm^{-2}S^n) compared to SS304 (3.53×10^{-6} Ω^{-1} cm^{-2}S^n) and an increase in R_{ct} (7.29×10^4 Ω cm^2) than that of SS304 (3.74×10^4 Ω cm^2). At low frequencies 0.1 Hz, impedance of the coated sample was found to be 4.3×10^5 Ω cm^2 and for SS304 of 2.28×10^4 Ω cm^2. Based on these results it was concluded and reported that SiOC-coated SS304 shows better corrosion resistance than uncoated SS304 in 0.6 M NaCl.

In another study, an amorphous SiCN (with a thickness of ~3.2 μm) was coated on SS304 using polysilazane as pre-cermic polymeric solution. Corrosion resistance of SiCN-coated samples was tested in 0.6 M NaCl solution. After 1 h immersion in electrolyte, OCP of the SiCN-coated SS304 was moved to the noble side (-0.037 V) compared to the base SS304 substrate. Corrosion rate was significantly improved for SiCN-coated SS304 as confirmed by decrease in i_{corr} value to three orders of magnitude lower (to 4.20×10^{-10} A/cm^2) than SS304. Impedance value measured at 0.1 Hz of SiCN coating shows a higher value of 3.93×10^6 Ω cm^2 and lower R_{ct} (8.98×10^7 Ω cm^2) values. From the electrochemical studies of SiCN-coated SS304, it was observed that SiCN-coating showed an enhanced corrosion protection performance than SiOC-coated SS304 (chapter 4 in this work).

To deposit the coatings, a simple coating technique is employed in this study, compared to the earlier reported coatings on SS, with PHPS-derived SiO_2-coated AISI 304, TiO_2-ZrO_2-coated

SS304, and Ta_3N_5-coated SS304. The current research shows improved corrosion resistance properties, as described in detail in Table 5.3 (Chapter 5).

The experimental results obtained within the framework of the present thesis work allow for the following recommendations for future research work:

1) Deposition of defect-free thick coatings on the substrates by using different filler materials to enhance the corrosion and high-temperature oxidation resistance applications.
2) Chemically modified precursors can be studied in future for enhancement of corrosion protection of SS304.
3) Corrosion resistance properties of PDC coatings on steels can be studied at higher temperatures (above 50°C in electrolytes).
4) Analyzing corrosion resistance of polymer-derived ceramics in acidic environments and examining the effect of immersion time on the corrosion resistance properties using EIS studies.

References

[1] S.A. Al-Fozan, A.U. Malik, Effect of seawater level on corrosion behavior of different alloys, Desalination 228 (2008) 61–67. https://doi.org/https://doi.org/10.1016/j.desal.2007.08.007.

[2] A.M. El-Sherik, Trends in oil and gas corrosion research and technologies: Production and transmission, Woodhead Publishing, 2017.

[3] D.A. Jones, Principles and prevention, Corrosion 2 (1996) 168.

[4] S. Hiromoto, 4 - Corrosion of metallic biomaterials, in: M. Niinomi (Ed.), Metals for Biomedical Devices, Woodhead Publishing, 2010: pp. 99–121. https://doi.org/https://doi.org/10.1533/9781845699246.2.99.

[5] W.S. Tait, Chapter 27 - Controlling Corrosion of Chemical Processing Equipment, in: M. Kutz (Ed.), Handbook of Environmental Degradation of Materials (Third Edition), William Andrew Publishing, 2018: pp. 583–600. https://doi.org/https://doi.org/10.1016/B978-0-323-52472-8.00028-9.

[6] Z. Ahmad, CHAPTER 2 - BASIC CONCEPTS IN CORROSION, in: Z. Ahmad (Ed.), Principles of Corrosion Engineering and Corrosion Control, Butterworth-Heinemann, Oxford, 2006: pp. 9–56. https://doi.org/https://doi.org/10.1016/B978-075065924-6/50003-9.

[7] S.C. Dexter, Galvanic Corrosion, (1999).

[8] D.A. Jones, Principles and prevention, Corrosion 2 (1996) 168.

[9] Z. Ahmad, Principles of corrosion engineering and corrosion control, Elsevier, 2006.

[10] S. Bandi, J. Banka, A. Kumar, A.K. Rai, Effects of sediment properties on abrasive erosion of a centrifugal pump, Chem Eng Sci 277 (2023) 118873. https://doi.org/https://doi.org/10.1016/j.ces.2023.118873.

[11] A. Dugstad, Formation of protective corrosion films during CO sub 2 corrosion of carbon steel, European Federation of Corrosion Publications (UK) 26 (1999) 70–76.

[12] V. Mitrovic-Scepanovic, R.J. Brigham, The localized corrosion of stainless steel in high purity sulphate solutions, Corros Sci 27 (1987) 545–553. https://doi.org/https://doi.org/10.1016/0010-938X(87)90028-X.

[13] A.J. Sedriks, Corrosion of stainless steels, John Wiley & Sons, 1996.

[14] B. Evgeny, T. Hughes, D. Eskin, Effect of surface roughness on corrosion behaviour of low carbon steel in inhibited 4M hydrochloric acid under laminar and turbulent flow conditions, Corros Sci 103 (2016) 196–205. https://doi.org/https://doi.org/10.1016/j.corsci.2015.11.019.

[15] A. Standard, Standard reference method for making potentiostatic and potentiodynamic anodic polarisation measurements, ASTM, G5-78 (1916).

[16] A.W. Colburn, K.J. Levey, D. O'Hare, J. V Macpherson, Lifting the lid on the potentiostat: a beginner's guide to understanding electrochemical circuitry and practical

operation, Physical Chemistry Chemical Physics 23 (2021) 8100–8117. https://doi.org/10.1039/D1CP00661D.

[17] T. Reyes Hernández, Study of corrosion of 13 Cr stainless steel under alternating current in artificial seawater, 2010-2019-Mines Theses & Dissertations (2011).

[18] F.O. Ajayi, Mitigating corrosion risks in oil and gas equipment by electrochemical protection: Top of the line corrosion, The University of Manchester (United Kingdom), 2015.

[19] N. Perez, Electrochemistry and corrosion science, Springer, 2004.

[20] F. Ríos, J. Calderón, R.P. Nogueira, Electrochemical Behavior of Metals Used in Drinking Water Distribution Systems: A Rotating Cylinder Electrode's Study, Corrosion 69 (2013) 875–885. https://doi.org/10.5006/0848.

[21] N.J. Laycock, R.C. Newman, Temperature dependence of pitting potentials for austenitic stainless steels above their critical pitting temperature, Corros Sci 40 (1998) 887–902. https://doi.org/https://doi.org/10.1016/S0010-938X(98)00020-1.

[22] K. Asami, K. Hashimoto, Importance of initial surface film in the degradation of stainless steels by atmospheric exposure, Corros Sci 45 (2003) 2263–2283. https://doi.org/https://doi.org/10.1016/S0010-938X(03)00047-7.

[23] B. Maier, G.S. Frankel, Pitting Corrosion of Bare Stainless Steel 304 under Chloride Solution Droplets, J Electrochem Soc 157 (2010) C302. https://doi.org/10.1149/1.3467850.

[24] R.P.V. Cruz, A. Nishikata, T. Tsuru, Pitting corrosion mechanism of stainless steels under wet-dry exposure in chloride-containing environments, Corros Sci 40 (1998) 125–139. https://doi.org/https://doi.org/10.1016/S0010-938X(97)00124-8.

[25] A. Nishikata, Y. Yamashita, H. Katayama, T. Tsuru, a. Usami, K. Tanabe, H. Mabuchi, An electrochemical impedance study on atmospheric corrosion of steels in a cyclic wet-dry condition, Corros Sci 37 (1995) 2059–2069. https://doi.org/https://doi.org/10.1016/0010-938X(95)00104-R.

[26] S. Hastuty, Y. Tsutsumi, A. Nishikata, T. Tsuru, Pitting Corrosion of Type 430 Stainless Steel in the Process of Drying of Chloride Solution Layer, ISIJ International 52 (2012) 863–867. https://doi.org/10.2355/isijinternational.52.863.

[27] O.E. Albores-Silva, E.A. Charles, C. Padovani, Effect of chloride deposition on stress corrosion cracking of 316L stainless steel used for intermediate level radioactive waste containers, Corrosion Engineering, Science and Technology 46 (2011) 124–128. https://doi.org/10.1179/1743278210Y.0000000004.

[28] R.C. Newman, 2001 W.R. Whitney Award Lecture: Understanding the Corrosion of Stainless Steel, Corrosion 57 (2001) 1030–1041. https://doi.org/10.5006/1.3281676.

[29] J. Srinivasan, J. Locke, T. Weirich, J.M. Taylor, C. Bryan, E.J. Schindelholz, Long-Term Atmospheric Corrosion of 304 Stainless Steel Used in Spent Dry Nuclear Fuel Storage

Containers, in: Electrochemical Society Meeting Abstracts 236, The Electrochemical Society, Inc., 2019: p. 843.

[30] L. Tjayadi, N. Kumar, K.L. Murty, Stress Corrosion Cracking Behavior of Austenitic Stainless Steel SS304 for Dry Storage Canisters in Simulated Sea-Water, in: TMS 2020 149th Annual Meeting & Exhibition Supplemental Proceedings, Springer International Publishing, Cham, 2020: pp. 1431–1442.

[31] F. Rahimi Kashani, M. Rezaei, Improving the localized corrosion resistance of 304 stainless steel in HCl solution by adsorption of molybdate ions: Interaction mechanisms at the interface using molecular dynamics simulation and electrochemical noise analysis, Colloids Surf A Physicochem Eng Asp 647 (2022) 129085. https://doi.org/https://doi.org/10.1016/j.colsurfa.2022.129085.

[32] P. Lambert, 6 - Sustainability of metals and alloys in construction, in: J.M. Khatib (Ed.), Sustainability of Construction Materials (Second Edition), Woodhead Publishing, 2016: pp. 105–128. https://doi.org/https://doi.org/10.1016/B978-0-08-100370-1.00006-8.

[33] M.C. Tanzi, S. Farè, G. Candiani, Foundations of biomaterials engineering, Academic Press, 2019.

[34] W. Tian, N. Du, S. Li, S. Chen, Q. Wu, Metastable pitting corrosion of 304 stainless steel in 3.5% NaCl solution, Corros Sci 85 (2014) 372–379. https://doi.org/https://doi.org/10.1016/j.corsci.2014.04.033.

[35] M.H. Nazari, X. Shi, Vehicle Risks of Winter Road Operations and Best Management Practices, in: Sustainable Winter Road Operations, 2018: pp. 241–272. https://doi.org/https://doi.org/10.1002/9781119185161.ch12.

[36] B.N. Popov, Chapter 4 - Passivity, in: B.N. Popov (Ed.), Corrosion Engineering, Elsevier, Amsterdam, 2015: pp. 143–179. https://doi.org/https://doi.org/10.1016/B978-0-444-62722-3.00004-5.

[37] B. Anandkumar, N.G. Krishna, R.V. Solomon, T. Nandakumar, J. Philip, Synergistic enhancement of corrosion protection of carbon steels using corrosion inhibitors and biocides: Molecular adsorption studies, DFT calculations and long-term corrosion performance evaluation, J Environ Chem Eng 11 (2023) 109842. https://doi.org/https://doi.org/10.1016/j.jece.2023.109842.

[38] W.-K. Lu, R.L. Elsenbaumer, B. Wessling, Corrosion protection of mild steel by coatings containing polyaniline, Synth Met 71 (1995) 2163–2166. https://doi.org/https://doi.org/10.1016/0379-6779(94)03204-J.

[39] M. Schirmeisen, F. Beck, Electrocoating of iron and other metals with polypyrrole, J Appl Electrochem 19 (1989) 401–409. https://doi.org/10.1007/BF01015243.

[40] N.M. Martyak, Chronoamperometric studies during the polymerization of aniline from an oxalic acid solution, Mater Chem Phys 81 (2003) 143–151. https://doi.org/https://doi.org/10.1016/S0254-0584(03)00167-6.

[41] M.C. Bernard, S. Joiret, A.H.-L. Goff, P.V. Phong, Protection of Iron Against Corrosion Using a Polyaniline Layer: I. Polyaniline Electrodeposit, J Electrochem Soc 148 (2001) B12. https://doi.org/10.1149/1.1344527.

[42] M. Shabani-Nooshabadi, S.M. Ghoreishi, M. Behpour, Electropolymerized polyaniline coatings on aluminum alloy 3004 and their corrosion protection performance, Electrochim Acta 54 (2009) 6989–6995. https://doi.org/https://doi.org/10.1016/j.electacta.2009.07.017.

[43] E. Machnikova, M. Pazderova, M. Bazzaoui, N. Hackerman, Corrosion study of PVD coatings and conductive polymer deposited on mild steel: Part I: Polypyrrole, Surf Coat Technol 202 (2008) 1543–1550. https://doi.org/https://doi.org/10.1016/j.surfcoat.2007.07.006.

[44] J.-L. Camalet, J.-C. Lacroix, T.D. Nguyen, S. Aeiyach, M.C. Pham, J. Petitjean, P.-C. Lacaze, Aniline electropolymerization on platinum and mild steel from neutral aqueous media, Journal of Electroanalytical Chemistry 485 (2000) 13–20. https://doi.org/https://doi.org/10.1016/S0022-0728(00)00080-2.

[45] J. Yahalom, Corrosion Protection Methods, in: K.H.J. Buschow, R.W. Cahn, M.C. Flemings, B. Ilschner, E.J. Kramer, S. Mahajan, P. Veyssière (Eds.), Encyclopedia of Materials: Science and Technology, Elsevier, Oxford, 2001: pp. 1710–1713. https://doi.org/https://doi.org/10.1016/B0-08-043152-6/00306-5.

[46] P.I. Nemes, M. Lekka, L. Fedrizzi, L.M. Muresan, Influence of the electrodeposition current regime on the corrosion resistance of Zn–CeO_2 nanocomposite coatings, Surf Coat Technol 252 (2014) 102–107. https://doi.org/https://doi.org/10.1016/j.surfcoat.2014.04.051.

[47] M. Sajjadnejad, M. Ghorbani, A. Afshar, Microstructure-corrosion resistance relationship of direct and pulse current electrodeposited Zn-TiO_2 nanocomposite coatings, Ceram Int 41 (2015) 217–224. https://doi.org/https://doi.org/10.1016/j.ceramint.2014.08.061.

[48] S. Anwar, F. Khan, Y. Zhang, Corrosion behaviour of Zn-Ni alloy and Zn-Ni-nano-TiO_2 composite coatings electrodeposited from ammonium citrate baths, Process Safety and Environmental Protection 141 (2020) 366–379. https://doi.org/https://doi.org/10.1016/j.psep.2020.05.048.

[49] M.K. Punith Kumar, M.Y. Rekha, J. Agrawal, T.M. Agarwal, C. Srivastava, Microstructure, morphology and electrochemical properties of ZnFe-Graphene composite coatings, J Alloys Compd 783 (2019) 820–827. https://doi.org/https://doi.org/10.1016/j.jallcom.2018.12.354.

[50] S. Arora, B. Sharma, C. Srivastava, ZnCo-carbon nanotube composite coating with enhanced corrosion resistance behavior, Surf Coat Technol 398 (2020) 126083. https://doi.org/https://doi.org/10.1016/j.surfcoat.2020.126083.

[51] P. Colombo, G. Mera, R. Riedel, G.D. Sorarù, Polymer-Derived Ceramics: 40 Years of Research and Innovation in Advanced Ceramics, Journal of the American Ceramic

Society 93 (2010) 1805–1837. https://doi.org/https://doi.org/10.1111/j.1551-2916.2010.03876.x.

[52] M.D. Nguyen, J.W. Bang, A.S. Bin, S.-R. Kim, Y. Kim, K.H. Hwang, V.-H. Pham, W.-T. Kwon, Novel polymer-derived ceramic environmental barrier coating system for carbon steel in oxidizing environments, J Eur Ceram Soc 37 (2017) 2001–2010. https://doi.org/https://doi.org/10.1016/j.jeurceramsoc.2016.12.049.

[53] Z. Lei, Q. Zhang, X. Zhu, D. Ma, F. Ma, Z. Song, Y.Q. Fu, Corrosion performance of ZrN/ZrO_2 multilayer coatings deposited on 304 stainless steel using multi-arc ion plating, Appl Surf Sci 431 (2018) 170–176. https://doi.org/https://doi.org/10.1016/j.apsusc.2017.06.273.

[54] İ. Çakmakcı Ünver, G. Bereket, B. Duran, Corrosion Protection of Stainless Steel by Poly(Carbazole-co-pyrrole) Films Deposited on TiO_2 Sol–Gel Film, Polym Plast Technol Eng 57 (2018) 242–250. https://doi.org/10.1080/03602559.2017.1320723.

[55] J. Hirpara, V. Chawla, R. Chandra, Investigation of tantalum oxynitride for hard and anti-corrosive coating application in diluted hydrochloric acid solutions, Mater Today Commun 23 (2020) 101113. https://doi.org/https://doi.org/10.1016/j.mtcomm.2020.101113.

[56] N.C.A.S. NON-POROUS, 9 THE PREPARATION OF PHOSPHORUS-NITROGEN COMPOUNDS AS NON-POROUS SOLIDS FW AINGER AND JM HERBERT, in: Special Ceramics: Proceedings of a Symposium Held at the British Ceramic Research Association, Heywood, 1960: p. 168.

[57] W. Verbeek, Production of shaped articles of homogeneous mixtures of silicon carbide and nitride, (1974).

[58] P. Colombo, Polymer derived ceramics: from nano-structure to applications, DEStech Publications, Inc, 2010.

[59] N.S. Choong Kwet Yive, R.J.P. Corriu, D. Leclercq, P.H. Mutin, A. Vioux, Silicon carbonitride from polymeric precursors: Thermal cross-linking and pyrolysis of oligosilazane model compounds, Chemistry of Materials 4 (1992) 141–146.

[60] J. He, M. Song, K. Chen, D. Kan, M. Zhu, Polymer-Derived Ceramics Technology: Characteristics, Procedure, Product Structures and Properties, and Development of the High-Entropy Ceramics, Crystals 2022, 12 (9), 1292. https://doi.org/10.3390/cryst12091292

[61] G. Barroso, Q. Li, R.K. Bordia, G. Motz, Polymeric and ceramic silicon-based coatings – a review, J Mater Chem A Mater 7 (2019) 1936–1963. https://doi.org/10.1039/C8TA09054H.

[62] R. Campostrini, A. Zambotti, M. Biesuz, G.D. Sorarù, On the pyrolysis of a methyl-silsesquioxane in reactive CO_2 atmosphere: A TG/MS and FT-IR study, Journal of the American Ceramic Society 105 (2022) 2465–2473. https://doi.org/https://doi.org/10.1111/jace.18270.

[63] C. Vakifahmetoglu, Fabrication and properties of ceramic 1D nanostructures from preceramic polymers: a review, Advances in Applied Ceramics 110 (2011) 188–204. https://doi.org/10.1179/1743676111Y.0000000007.

[64] S. Fu, M. Zhu, Y. Zhu, Organosilicon polymer-derived ceramics: An overview, Journal of Advanced Ceramics 8 (2019) 457–478. https://doi.org/10.1007/s40145-019-0335-3.

[65] Y. Zhang, A. Quaranta, G. Domenico Soraru, Synthesis and luminescent properties of novel Eu^{2+}-doped silicon oxycarbide glasses, Opt Mater (Amst) 24 (2004) 601–605. https://doi.org/https://doi.org/10.1016/S0925-3467(03)00162-9.

[66] Y. Wang, Y. Fan, L. Zhang, W. Zhang, L. An, Polymer-derived SiAlCN ceramics resist oxidation at 1400°C, Scr Mater 55 (2006) 295–297. https://doi.org/https://doi.org/10.1016/j.scriptamat.2006.05.004.

[67] C.D. Doyle, Estimating Thermal Stability of Experimental Polymers by Empirical Thermogravimetric Analysis, Anal Chem 33 (1961) 77–79. https://doi.org/10.1021/ac60169a022.

[68] R. Raj, Fundamental Research in Structural Ceramics for Service Near 2000°C, Journal of the American Ceramic Society 76 (1993) 2147–2174. https://doi.org/https://doi.org/10.1111/j.1151-2916.1993.tb07750.x.

[69] Y. Wang, Polymer-derived Si-al-cn Ceramics: oxidation, Hot-corrosion, And Structural Evolution, (2006).

[70] R. Riedel, H.-J. Kleebe, H. Schönfelder, F. Aldinger, A covalent micro/nano-composite resistant to high-temperature oxidation, Nature 374 (1995) 526–528. https://doi.org/10.1038/374526a0.

[71] L. An, Y. Wang, L. Bharadwaj, L. Zhang, Y. Fan, D. Jiang, Y. Sohn, V.H. Desai, J. Kapat, L.C. Chow, Silicoaluminum Carbonitride with Anomalously High Resistance to Oxidation and Hot Corrosion, Adv Eng Mater 6 (2004) 337–340. https://doi.org/https://doi.org/10.1002/adem.200400010.

[72] Y. Wang, L. An, Y. Fan, L. Zhang, S. Burton, Z. Gan, Oxidation of polymer-derived SiAlCN ceramics, Journal of the American Ceramic Society 88 (2005) 3075–3080.https://doi.org/10.1111/j.1551-2916.2005.00542.x

[73] S. YAJIMA, J. HAYASHI, M. OMORI, K. OKAMURA, Development of a silicon carbide fibre with high tensile strength, Nature 261 (1976) 683–685. https://doi.org/10.1038/261683a0.

[74] Y. Hasegawa, K. Okamura, Synthesis of continuous silicon carbide fibre, J Mater Sci 18 (1983) 3633–3648. https://doi.org/10.1007/BF00540736.

[75] Y. Hasegawa, M. Iimura, S. Yajima, Synthesis of continuous silicon carbide fibre, J Mater Sci 15 (1980) 720–728. https://doi.org/10.1007/BF00551739.

[76] T. Yamamura, T. Ishikawa, M. Shibuya, T. Hisayuki, K. Okamura, Development of a new continuous Si-Ti-C-O fibre using an organometallic polymer precursor, J Mater Sci 23 (1988) 2589–2594. https://doi.org/10.1007/BF01111919.

[77] T. Ishikawa, Y. Kohtoku, K. Kumagawa, T. Yamamura, T. Nagasawa, High-strength alkali-resistant sintered SiC fibre stable to 2,200 °C, Nature 391 (1998) 773–775. https://doi.org/10.1038/35820.

[78] S. Bernard, M. Weinmann, P. Gerstel, P. Miele, F. Aldinger, Boron-modified polysilazane as a novel single-source precursor for SiBCN ceramic fibers: synthesis, melt-spinning, curing and ceramic conversion, J Mater Chem 15 (2005) 289–299. https://doi.org/10.1039/B408295H.

[79] G.D. Sorarù, E. Dallapiccola, G. D'Andrea, Mechanical Characterization of Sol–Gel-Derived Silicon Oxycarbide Glasses, Journal of the American Ceramic Society 79 (1996) 2074–2080. https://doi.org/https://doi.org/10.1111/j.1151-2916.1996.tb08939.x.

[80] N. Janakiraman, F. Aldinger, Fabrication and characterization of fully dense Si–C–N ceramics from a poly(ureamethylvinyl)silazane precursor, J Eur Ceram Soc 29 (2009) 163–173. https://doi.org/https://doi.org/10.1016/j.jeurceramsoc.2008.05.028.

[81] S.R. Shah, R. Raj, Mechanical properties of a fully dense polymer derived ceramic made by a novel pressure casting process, Acta Mater 50 (2002) 4093–4103. https://doi.org/https://doi.org/10.1016/S1359-6454(02)00206-9.

[82] G.M. Renlund, S. Prochazka, R.H. Doremus, Silicon oxycarbide glasses: Part II. Structure and properties, J Mater Res 6 (1991) 2723–2734. https://doi.org/DOI: 10.1557/JMR.1991.2723.

[83] C. Moysan, R. Riedel, R. Harshe, T. Rouxel, F. Augereau, Mechanical characterization of a polysiloxane-derived SiOC glass, J Eur Ceram Soc 27 (2007) 397–403. https://doi.org/https://doi.org/10.1016/j.jeurceramsoc.2006.01.016.

[84] P. Kroll, Modelling polymer-derived ceramics, J Eur Ceram Soc 25 (2005) 163–174. https://doi.org/https://doi.org/10.1016/j.jeurceramsoc.2004.07.012.

[85] P. Kroll, Modelling and simulation of amorphous silicon oxycarbide, J Mater Chem 13 (2003) 1657–1668. https://doi.org/10.1039/B301389H.

[86] T. Rouxel, Elastic Properties and Short-to Medium-Range Order in Glasses, Journal of the American Ceramic Society 90 (2007) 3019–3039. https://doi.org/https://doi.org/10.1111/j.1551-2916.2007.01945.x.

[87] S. Walter, G.D. Soraru, H. Bréquel, S. Enzo, Microstructural and mechanical characterization of sol gel-derived Si–O–C glasses, J Eur Ceram Soc 22 (2002) 2389–2400. https://doi.org/https://doi.org/10.1016/S0955-2219(01)00537-4.

[88] G. Ziegler, H.-J. Kleebe, G. Motz, H. Müller, S. Traßl, W. Weibelzahl, Synthesis, microstructure and properties of SiCN ceramics prepared from tailored polymers, Mater Chem Phys 61 (1999) 55–63. https://doi.org/https://doi.org/10.1016/S0254-0584(99)00114-5.

[89] K. V Moraes, L. V Interrante, Processing, Fracture Toughness, and Vickers Hardness of Allylhydridopolycarbosilane-Derived Silicon Carbide, Journal of the American Ceramic Society 86 (2003) 342–346. https://doi.org/https://doi.org/10.1111/j.1151-2916.2003.tb00020.x.

[90] S.R. Shah, R. Raj, Mechanical properties of a fully dense polymer derived ceramic made by a novel pressure casting process, Acta Mater 50 (2002) 4093–4103. https://doi.org/https://doi.org/10.1016/S1359-6454(02)00206-9.

[91] T. Nishimura, R. Haug, J. Bill, G. Thurn, F. Aldinger, Mechanical and thermal properties of Si–C–N material from polyvinylsilazane, J Mater Sci 33 (1998) 5237–5241. https://doi.org/10.1023/A:1004440122266.

[92] N. Janakiraman, Z. Burghard, F. Aldinger, Fracture toughness evaluation of precursor-derived Si–C–N ceramics using the crack opening displacement approach, J Non Cryst Solids 355 (2009) 2102–2113. https://doi.org/https://doi.org/10.1016/j.jnoncrysol.2009.07.002.

[93] A. Bauer, M. Christ, A. Zimmermann, F. Aldinger, Fracture Toughness of Amorphous Precursor-Derived Ceramics in the Silicon-Carbon-Nitrogen System, Journal of the American Ceramic Society 84 (2001) 2203–2207. https://doi.org/https://doi.org/10.1111/j.1151-2916.2001.tb00988.x.

[94] T. Rouxel, J.-C. Sanglebœuf, J.-P. Guin, V. Keryvin, G.-D. Soraru, Surface Damage Resistance of Gel-Derived Oxycarbide Glasses: Hardness, Toughness, and Scratchability, Journal of the American Ceramic Society 84 (2001) 2220–2224. https://doi.org/https://doi.org/10.1111/j.1151-2916.2001.tb00991.x.

[95] T. Rouxel, G. Massouras, G.-D. Sorarù, High Temperature Behavior of a Gel-Derived SiOC Glass: Elasticity and Viscosity, J Solgel Sci Technol 14 (1999) 87–94. https://doi.org/10.1023/A:1008779915809.

[96] K. Ota, G. Pezzotti, Internal friction analysis of structural relaxation in Si–C–O glass, J Non Cryst Solids 318 (2003) 248–253. https://doi.org/https://doi.org/10.1016/S0022-3093(02)01905-1.

[97] L. An, R. Riedel, C. Konetschny, H.-J. Kleebe, R. Raj, Newtonian Viscosity of Amorphous Silicon Carbonitride at High Temperature, Journal of the American Ceramic Society 81 (1998) 1349–1352. https://doi.org/https://doi.org/10.1111/j.1151-2916.1998.tb02489.x.

[98] A. Zimmermann, A. Bauer, M. Christ, Y. Cai, F. Aldinger, High-temperature deformation of amorphous Si–C–N and Si–B–C–N ceramics derived from polymers, Acta Mater 50 (2002) 1187–1196. https://doi.org/https://doi.org/10.1016/S1359-6454(01)00420-7.

[99] N. V Ravi Kumar, S. Prinz, Y. Cai, A. Zimmermann, F. Aldinger, F. Berger, K. Müller, Crystallization and creep behavior of Si–B–C–N ceramics, Acta Mater 53 (2005) 4567–4578. https://doi.org/https://doi.org/10.1016/j.actamat.2005.06.011.

[100] R. Riedel, G. Passing, H. Schönfelder, R.J. Brook, Synthesis of dense silicon-based ceramics at low temperatures, Nature 355 (1992) 714–717. https://doi.org/10.1038/355714a0.

[101] A. Scarmi, G.D. Sorarù, R. Raj, The role of carbon in unexpected visco(an)elastic behavior of amorphous silicon oxycarbide above 1273K, J Non Cryst Solids 351 (2005) 2238–2243. https://doi.org/https://doi.org/10.1016/j.jnoncrysol.2005.06.008.

[102] B. Clauß, Fibers for ceramic matrix composites, Weinheim, Germany: WILEY-VCH Verlag GmbH & Co. KGaA, 2008.

[103] D. Cornu, S. Bernard, S. Duperrier, B. Toury, P. Miele, Alkylaminoborazine-based precursors for the preparation of boron nitride fibers by the polymer-derived ceramics (PDCs) route, J Eur Ceram Soc 25 (2005) 111–121. https://doi.org/https://doi.org/10.1016/j.jeurceramsoc.2004.07.016.

[104] N. Li, Y. Cao, R. Zhao, Y. Xu, L. An, Polymer-derived SiAlOC ceramic pressure sensor with potential for high-temperature application, Sens Actuators A Phys 263 (2017) 174–178. https://doi.org/https://doi.org/10.1016/j.sna.2017.06.006.

[105] P. Colombo, Polymer derived ceramics: from nano-structure to applications, DEStech Publications, Inc, 2010.

[106] F. Cheng, S.M. Kelly, S. Clark, J.S. Bradley, M. Baumbach, A. Schütze, Preparation and characterization of a supported Si_3N_4 membrane via a non-aqueous sol–gel process, J Memb Sci 280 (2006) 530–535. https://doi.org/https://doi.org/10.1016/j.memsci.2006.02.006.

[107] R.M. Prasad, A. Gurlo, R. Riedel, M. Hübner, N. Barsan, U. Weimar, Microporous ceramic coated SnO_2 sensors for hydrogen and carbon monoxide sensing in harsh reducing conditions, Sens Actuators B Chem 149 (2010) 105–109. https://doi.org/https://doi.org/10.1016/j.snb.2010.06.016.

[108] B. Kumar, R.M. Prasad, Polymer-derived microporous SiOC ceramic coated gallium nitride sensor for selective H_2/CO detection, Sens Actuators B Chem 379 (2023) 133226. https://doi.org/https://doi.org/10.1016/j.snb.2022.133226.

[109] M. Günthner, A. Schütz, U. Glatzel, K. Wang, R.K. Bordia, O. Greißl, W. Krenkel, G. Motz, High performance environmental barrier coatings, Part I: Passive filler loaded SiCN system for steel, J Eur Ceram Soc 31 (2011) 3003–3010. https://doi.org/https://doi.org/10.1016/j.jeurceramsoc.2011.05.027.

[110] T. Kraus, G. M., K. W., G. and Motz, cBN particle filled SiCN precursor coatings, Advances in Applied Ceramics 108 (2009) 476–482. https://doi.org/10.1179/174367609X422153.

[111] M. Günthner, T. Kraus, W. Krenkel, G. Motz, A. Dierdorf, D. Decker, Particle-Filled PHPS Silazane-Based Coatings on Steel, Int J Appl Ceram Technol 6 (2009) 373–380. https://doi.org/https://doi.org/10.1111/j.1744-7402.2008.02346.x.

[112] A. Schütz, M. Günthner, G. Motz, O. Greißl, U. Glatzel, Characterisation of novel precursor-derived ceramic coatings with glass filler particles on steel substrates, Surf Coat Technol 207 (2012) 319–327. https://doi.org/https://doi.org/10.1016/j.surfcoat.2012.07.013.

[113] A. Schütz, M. Günthner, G. Motz, O. Greißl, U. Glatzel, High temperature (salt melt) corrosion tests with ceramic-coated steel, Mater Chem Phys 159 (2015) 10–18. https://doi.org/https://doi.org/10.1016/j.matchemphys.2015.03.023.

[114] M. Lenz Leite, G. Barroso, M. Parchovianský, D. Galusek, E. Ionescu, W. Krenkel, G. Motz, Synthesis and characterization of yttrium and ytterbium silicates from their oxides and an oligosilazane by the PDC route for coating applications to protect Si_3N_4 in hot gas environments, J Eur Ceram Soc 37 (2017) 5177–5191. https://doi.org/https://doi.org/10.1016/j.jeurceramsoc.2017.04.034.

[115] J. Liu, L. Zhang, F. Hu, J. Yang, L. Cheng, Y. Wang, Polymer-derived yttrium silicate coatings on 2D C/SiC composites, J Eur Ceram Soc 33 (2013) 433–439. https://doi.org/https://doi.org/10.1016/j.jeurceramsoc.2012.08.032.

[116] K. Wang, J. Unger, J.D. Torrey, B.D. Flinn, R.K. Bordia, Corrosion resistant polymer derived ceramic composite environmental barrier coatings, J Eur Ceram Soc 34 (2014) 3597–3606. https://doi.org/https://doi.org/10.1016/j.jeurceramsoc.2014.05.036.

[117] F. Li, Y. Wang, W. Dang, Z. Xu, X. Zhang, B. Zhang, K. Zhao, Y. Tang, Effect of curing process and pyrolysis temperature on the microstructure, adhesion and corrosion resistance of PCS-derived coatings, Ceram Int 48 (2022) 28046–28058. https://doi.org/https://doi.org/10.1016/j.ceramint.2022.06.110.

[118] W. Wang, S. Tamakloe, Z. Deng, L. Li, W. Cai, K. Lu, Effects of processing temperature on the corrosion and tribocorrosion resistance of perhydropolysilazane-derived coatings on AISI 304 steel, Surf Coat Technol 439 (2022) 128463. https://doi.org/https://doi.org/10.1016/j.surfcoat.2022.128463.

[119] R. Bertoncello, A. Vezzoli, E. Rebollo, Corrosion behaviour of room temperature cured polysilazane-derived silica coatings on Al 5086, International Journal of Engineering Research & Science 2 (2016) 105–112.

[120] H.J. Choi, K. Lu, Polysilazane-derived SiON coating on stainless steel weld for corrosion resistance, Mater Chem Phys 315 (2024) 128988. https://doi.org/https://doi.org/10.1016/j.matchemphys.2024.128988.

[121] M.R. Gruber, B. Hofko, M. Hoffmann, D. Stinglmayr, H. Grothe, Analysis of metal corrosion methods and identification of cost-efficient and low corrosion deicing agents, Corrosion Engineering, Science and Technology 58 (2023) 452–463.

[122] J. Chruściel, M. Fejdyś, W. Fortuniak, Synthesis and characterization of new, liquid, branched poly(methylvinylborosiloxanes), 13 (2013). https://doi.org/doi:10.1515/epoly-2013-0134.

[123] E. Ionescu, C. Linck, C. Fasel, M. Müller, H. Kleebe, R. Riedel, Polymer-Derived $SiOC/ZrO_2$ Ceramic Nanocomposites with Excellent High-Temperature Stability, Journal of the American Ceramic Society 93 (2010) 241–250. https://doi.org/https://doi.org/10.1111/j.1551-2916.2009.03395.x.

[124] D. Su, Y.-L. Li, H.-J. An, X. Liu, F. Hou, J.-Y. Li, X. Fu, Pyrolytic transformation of liquid precursors to shaped bulk ceramics, J Eur Ceram Soc 30 (2010) 1503–1511. https://doi.org/https://doi.org/10.1016/j.jeurceramsoc.2009.11.015.

[125] X. Zhan, X. Cai, J. Zhang, A novel crosslinking agent of polymethyl(ketoxime)siloxane for room temperature vulcanized silicone rubbers: synthesis, properties and thermal stability, RSC Adv 8 (2018) 12517–12525. https://doi.org/10.1039/C7RA13375H.

[126] Y. Zhan, Rapid Curing and Boron Modification of Polysilazane-Derived Functional Coatings, (2022).

[127] M. Thommes, K. Kaneko, A. V Neimark, J.P. Olivier, F. Rodriguez-Reinoso, J. Rouquerol, K.S.W. Sing, Physisorption of gases, with special reference to the evaluation of surface area and pore size distribution (IUPAC Technical Report), 87 (2015) 1051–1069. https://doi.org/doi:10.1515/pac-2014-1117.

[128] Q.D. Nghiem, J.-K. Jeon, L.-Y. Hong, D.-P. Kim, Polymer derived Si–C–B–N ceramics via hydroboration from borazine derivatives and trivinylcyclotrisilazane, J Organomet Chem 688 (2003) 27–35. https://doi.org/https://doi.org/10.1016/j.jorganchem.2003.08.025.

[129] M. Hörz, A. Zern, F. Berger, J. Haug, K. Müller, F. Aldinger, M. Weinmann, Novel polysilazanes as precursors for silicon nitride/silicon carbide composites without “free” carbon, J Eur Ceram Soc 25 (2005) 99–110. https://doi.org/https://doi.org/10.1016/j.jeurceramsoc.2004.07.020.

[130] M.A. Schiavon, G. Domenico Sorarù, I.V.P. Yoshida, Synthesis of a polycyclic silazane network and its evolution to silicon carbonitride glass, J Non Cryst Solids 304 (2002) 76–83. https://doi.org/https://doi.org/10.1016/S0022-3093(02)01007-4.

[131] N.R. Dando, A.J. Perrotta, C. Strohmann, R.M. Stewart, D. Seyferth, Methylhydridopolysilazane and its pyrolytic conversion to silicon nitride-silicon carbide (Si3N4/SiC) ceramics, Chemistry of Materials 5 (1993) 1624–1630.

[132] H. Ramlow, L.L. Silva, C. Marangoni, M.R. Baldan, R.A.F. Machado, Corrosion and heat-resistant SiCN/C as lightweight fibers for microwave absorption and electromagnetic field shielding in Ku-band, Diam Relat Mater 144 (2024) 110985. https://doi.org/https://doi.org/10.1016/j.diamond.2024.110985.

[133] Y. Feng, S. Dou, Y. Wei, Y. Zhang, X. Song, X. Li, V.S. Battaglia, Preparation and Capacity-Fading Investigation of Polymer-Derived Silicon Carbonitride Anode for Lithium-Ion Battery, ACS Omega 2 (2017) 8075–8085. https://doi.org/10.1021/acsomega.7b01462.

[134] E. Kroke, Y.-L. Li, C. Konetschny, E. Lecomte, C. Fasel, R. Riedel, Silazane derived ceramics and related materials, Materials Science and Engineering: R: Reports 26 (2000) 97–199. https://doi.org/https://doi.org/10.1016/S0927-796X(00)00008-5.

[135] R.M. Prasad, Y. Jüttke, H. Richter, I. Voigt, R. Riedel, A. Gurlo, Mechanism of gas separation through amorphous silicon oxycarbide membranes, Adv Eng Mater 18 (2016) 721–727.

[136] R.M. Prasad, Y. Iwamoto, R. Riedel, A. Gurlo, Multilayer Amorphous-Si-B-C-N/γ-Al_2O_3/α-Al_2O_3 Membranes for Hydrogen Purification, Adv Eng Mater 12 (2010) 522–528. https://doi.org/https://doi.org/10.1002/adem.201000095.

[137] R. Bura, B. Kumar, R.M. Prasad, Polymer-derived SiOC ceramic coating for corrosion protection, Int J Appl Ceram Technol 21 (2024) 900–909. https://doi.org/https://doi.org/10.1111/ijac.14588.

[138] U.M.R. Seelam, C. Suryanarayana, Metallography of Sputter-Deposited SS304+Al Coatings, Metallography, Microstructure, and Analysis 2 (2013) 287–298. https://doi.org/10.1007/s13632-013-0087-3.

[139] S. Akhtar, A. Matin, A. Madhan Kumar, A. Ibrahim, T. Laoui, Enhancement of anticorrosion property of 304 stainless steel using silane coatings, Appl Surf Sci 440 (2018) 1286–1297. https://doi.org/https://doi.org/10.1016/j.apsusc.2018.01.203.

[140] Y. Singhbabu, S. Bose, S. Choudhary, S. Das, R. Sahu, Corrosion-protective reduced graphene oxide coated cold rolled steel prepared using industrial setup: A study of protocol feasibility for commercial production, Surf Coat Technol 349 (2018). https://doi.org/10.1016/j.surfcoat.2018.05.046.

[141] W. Wang, S. Tamakloe, Z. Deng, L. Li, W. Cai, K. Lu, Effects of processing temperature on the corrosion and tribocorrosion resistance of perhydropolysilazane-derived coatings on AISI 304 steel, Surf Coat Technol 439 (2022) 128463. https://doi.org/https://doi.org/10.1016/j.surfcoat.2022.128463.

[142] C.-J. Weng, C.-H. Chang, C.-W. Peng, S.-W. Chen, J.-M. Yeh, C.-L. Hsu, Y. Wei, Advanced Anticorrosive Coatings Prepared from the Mimicked Xanthosoma Sagittifolium-leaf-like Electroactive Epoxy with Synergistic Effects of Superhydrophobicity and Redox Catalytic Capability, Chemistry of Materials 23 (2011) 2075–2083. https://doi.org/10.1021/cm1030377.

[143] X. Chen, H. Liu, X. Sun, B. Zan, M. Liang, Chloride corrosion behavior on heating pipeline made by AISI 304 and 316 in reclaimed water, RSC Adv 11 (2021) 38765–38773. https://doi.org/10.1039/D1RA06695A.

[144] M. Yu, Z. Cui, F. Ge, Y. Lin, L. Lei, X. Wang, Y. Frank Cheng, Facile fabrication of hydrophobic polysiloxane coatings for protection of AZ31 magnesium alloy, J Mater Sci 54 (2019) 9759–9774. https://doi.org/10.1007/s10853-019-03544-2.

[145] R.M. Bandeira, J. van Drunen, A.C. Garcia, G. Tremiliosi-Filho, Influence of the thickness and roughness of polyaniline coatings on corrosion protection of AA7075 aluminum alloy, Electrochim Acta 240 (2017) 215–224. https://doi.org/https://doi.org/10.1016/j.electacta.2017.04.083.

[146] T.S. Lim, H.S. Ryu, S.-H. Hong, Electrochemical corrosion properties of CeO_2-containing coatings on AZ31 magnesium alloys prepared by plasma electrolytic oxidation, Corros Sci 62 (2012) 104–111. https://doi.org/https://doi.org/10.1016/j.corsci.2012.04.043.

[147] E. Potvin, L. Brossard, G. Larochelle, Corrosion protective performances of commercial low-VOC epoxy/urethane coatings on hot-rolled 1010 mild steel, Prog Org Coat 31 (1997) 363–373. https://doi.org/https://doi.org/10.1016/S0300-9440(97)00095-7.

[148] M. Isakhani-Zakaria, S.R. Allahkaram, H.A. Ramezani-Varzaneh, Evaluation of corrosion behaviour of Pb-Co_3O_4 electrodeposited coating using EIS method, Corros Sci 157 (2019) 472–480. https://doi.org/https://doi.org/10.1016/j.corsci.2019.06.023.

[149] M. Criado, S. Martínez-Ramirez, S. Fajardo, P.P. Gómez, J.M. Bastidas, Corrosion rate and corrosion product characterisation using Raman spectroscopy for steel embedded in

chloride polluted fly ash mortar, Materials and Corrosion 64 (2013) 372–380. https://doi.org/https://doi.org/10.1002/maco.201206714.

[150] A. Jiang, Y. Di, S. Chen, D. Zhang, X. Chen, Z. Zhang, X. Zhang, Q. Dong, Photocathodic protection of 304 stainless steel by coating muscovite/TiO_2 heterostructure, Appl Clay Sci 240 (2023) 106974. https://doi.org/https://doi.org/10.1016/j.clay.2023.106974.

[151] J. Hirpara, V. Chawla, R. Chandra, Anticorrosive Behavior Enhancement of Stainless Steel 304 through Tantalum-Based Coatings: Role of Coating Morphology, J Mater Eng Perform 30 (2021). https://doi.org/10.1007/s11665-021-05542-5.

[152] M.Y. Al-Daraghmeh, M.T. Hayajneh, M.A. Almomani, Corrosion Resistance of TiO_2-ZrO_2 Nanocomposite Thin Films Spin Coated on AISI 304 Stainless Steel in 3.5 wt. % NaCl Solution, Materials Research 22 (2019) e20190014. https://doi.org/10.1590/1980-5373-mr-2019-0014.

[153] R. Bura, V.G. C, R.M. Prasad, Enhanced corrosion protection performance using polysilazane-derived amorphous SiCN ceramic coating, Surf Coat Technol 494 (2024) 131402. https://doi.org/https://doi.org/10.1016/j.surfcoat.2024.131402.